THE UNIVERSITY OF CHICAGO

ATOM PROBE TOMOGRAPHY OF LUNAR MATERIALS

A DISSERTATION SUBMITTED TO
THE FACULTY OF THE DIVISION OF THE PHYSICAL SCIENCES
IN CANDIDACY FOR THE DEGREE OF
DOCTOR OF PHILOSOPHY

DEPARTMENT OF THE GEOPHYSICAL SCIENCES

BY
JENNIKA GREER

CHICAGO, ILLINOIS
DECEMBER 2022

TABLE OF CONTENTS

Chapter 3 ········ **36**

Atom Probe Tomography of Space-Weathered Lunar Imenite Grain Surfaces

LIST OF FIGURES

LIST OF TABLES

ACKNOWLEDGEMENTS

If I were to properly thank everyone, this work would easily be another 100 pages. To the many mentors, colleagues, collaborators, friends, and family who helped me along this path, I look forward to thanking you properly and in-person. There are two individuals in particular I wish to mention here: Dieter Isheim, without whose atom probe expertise none of this would have been possible, and Philipp Heck, who is an unparalleled adviser, curator, and scientist.

ABSTRACT

Lunar materials preserve records of the conditions and processes of the time when the Moon was first formed in the giant impact event, but also show evidence of more recent activity that involves the processes of impact cratering and space weathering that are active on the lunar surface today. Alteration due to space weathering can drastically change the reflectance spectra of these bodies as viewed with remote sensing through ground-based telescopes and spacecraft compared to laboratory analysis of the same material that was not space weathered. My work uses atom probe tomography (APT) to investigate the nanoscale characteristics of lunar materials and show how such analyses can be used to better understand the large-scale processes on the Moon. This includes the analysis of space weathered soils brought back by astronauts and the distribution of Pb in the oldest lunar zircon to date.

CHAPTER 1: INTRODUCTION

1.1 MOTIVATION

The overall goal of this work is to characterize select lunar materials at the nanoscale using atom probe tomography (APT). Unlike the Earth, where many different geologic processes have continuously overprinted primary compositions and structures, the Moon has been geologically active in its first billion years but relatively quiescent for much of its later history. There is, therefore, an abundance of lunar materials that preserve records of the conditions and processes of the time when the Moon was geologically more active. However, many, lunar samples show evidence of more recent activity, one that involves the processes of impact cratering and space weathering that active on the lunar surface today.

Early in the Solar System's history, perhaps during the first 60 to 110 Myr (Touboul et al., 2007; Halliday, 2008; Kleine et al., 2009; Jacobson et al., 2014), the Earth-Moon system formed through a giant impact between the proto-Earth and Theia, a Mars-sized protoplanet, the result being a nearly completely molten Moon known as the lunar magma ocean (LMO). The timing of this event is still debated. Reported ages for the Moon-forming event based on lunar mare basalts using short-lived isotopic chronometers (such as ^{146}Sm-^{142}Nd and Hf-W) range from 4.455 to 4.314 Ga (e.g. Nyquist et al., 1995; Lee et al., 1997; Rankenburg et al., 2006; Boyet and Carlson, 2007; Brandon et al., 2009; Gaffney and Borg, 2014), whereas modeled U-Pb systematics derive a Moon-forming event age of 4.426 to 4.417 billion years (Connelly and Bizzarro, 2016). Disagreement on the ages (4.536 – 4.290 billion years) of the oldest preserved lunar material, ferroan anorthosites, has implications for the timing, duration, and nature of LMO crystallization and the overall differentiation history of the moon (Alibert et al., 1994; Borg et al., 1999; Nyquist et al., 2006; Shearer et al., 2006; Meyer et al., 2010, Elkins-Tanton et al., 2011). In chapter 5 I provide new chronological constraints on the timing of the Moon-forming event and LMO through APT analysis of an old lunar zircon.

Space weathering, the physical and chemical alteration of materials on airless bodies like the moon, is an active process on the lunar surface today. Despite the fact that space weathering only affects the outermost ~100 nm of a grain's surface, this alteration can drastically change the overall color and the reflectance spectra of these bodies as viewed with remote sensing through ground-based telescopes and spacecraft, compared to laboratory analysis of the same material that was not space weathered (e.g., Chapman, 1996). Spectral studies of the Moon are extremely useful for generating compositional data that can be used to understand its present global composition and its history; thus, it is critical to understand how lunar materials change when exposed to space weathering. Prolonged exposure to space weathering increases the degree of alteration of the surface of the materials and thus its *maturity.* A frequent definition of the maturity is the abundance of nanoscale metallic iron particles (Morris, 1978). This classification uses the expressions *immature* to describe the least space-weathered samples and *submature* for the intermediately weathered materials.

The effects of space weathering on lunar materials generally manifest at the nanoscale. In chapters 3 and 4, I use APT to investigate the nanoscale characteristics of lunar materials, where atoms on a sample nanotip are field-evaporated using a pulsed laser, accelerated through a local electrode, and measured by a position sensitive detector. In this way, both the compositions and distributions of the atoms in the sample can be measured in three dimensions. This work also demonstrates the power of APT analysis when correlated with other techniques, such as transmission electron microscopy (TEM; chapter 4) and nanoscale secondary ion mass spectrometry (NanoSIMS; chapter 5). In this work I provide examples on how nanoscale analyses of lunar samples are instrumental in better understanding the large-scale processes in our Solar System.

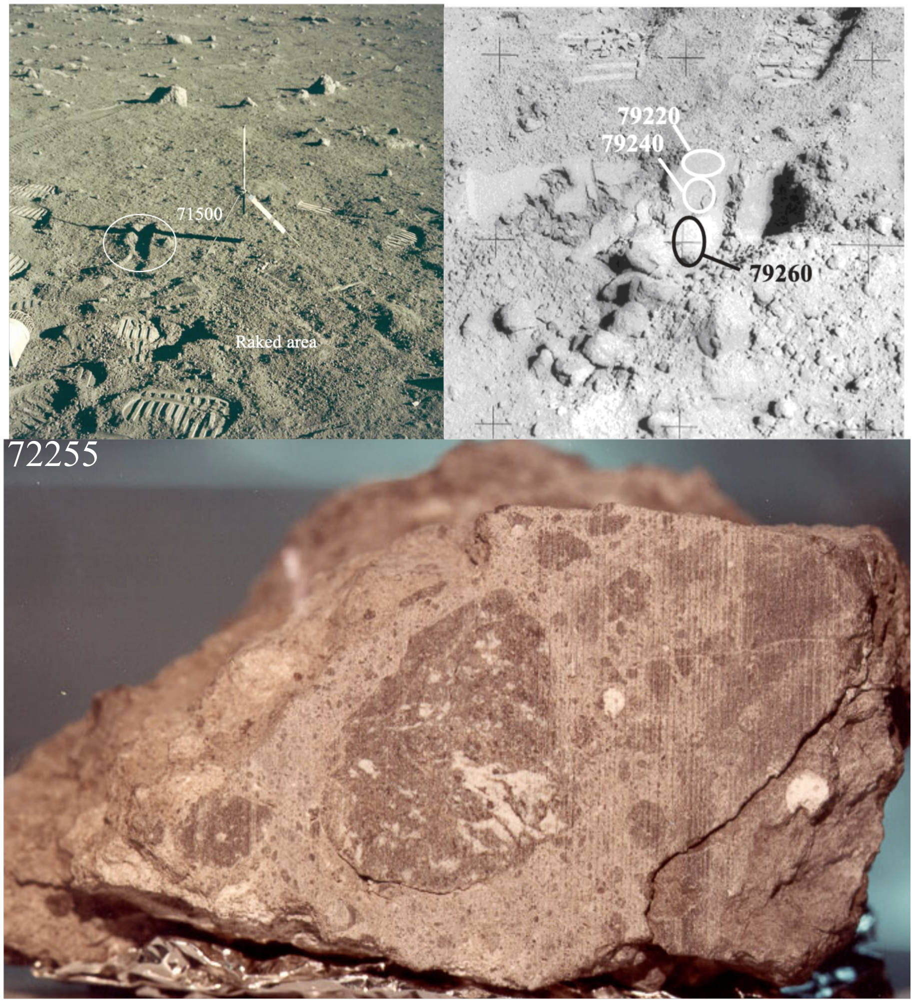

Figure 1-1: Images of the sampling sites or samples from the Lunar Sample Compendium (Meyer, 2010). 71501 is a sub-sample of 71500, 79221 is a sub-sample of 79220, and the largest dark region in the cross section of sample 72255 is the Civet Cat norite.

1.2 SAMPLES

The materials that were analyzed in this work were collected by the astronauts of the Apollo 17 lunar mission, which landed in the Serenitatis basin in the Taurus-Littrow region. One of the main goals for sampling this region was to constrain the timing of lunar volcanism, and therefore the Moon’s thermal history. The site provided five different geologic units of interest (Apollo 17

Preliminary Examination Team, 1973). In addition to the rock and core samples collected, a total of 73 soil samples were also brought back (Heiken and McKay, 1974). Unlike terrestrial soils, these soils have no biomatter, and this term is used when discussing the fine-grained (< 1 cm) regolith of the Moon's surface. The lunar regolith is the material from the bedrock that has been broken-up, altered, and is subject to mixing by impact processes (McKay et al., 1991).

1.2.1 Ilmenite, Apollo 17 sample 71501, aliquot 284

Ilmenite ($FeTiO_3$) is a black, opaque oxide mineral that is a common accessory phase in igneous and metamorphic rocks (Deer et al., 1992) and can comprise up to about 20% of lunar soils (McKay and Williams, 1979; Papike et al., 1991). The Apollo 17 sample 71501 (Figure 1-1) is a particularly well-studied sample for its implanted solar wind (e.g. Benkert et al., 1993). Ilmenite is particularly retentive to noble gases and is therefore an ideal target for the study of implanted solar wind. Sample 71501 has been classified as a submature sample (Heiken and McKay, 1974). The sample is mostly comprised of basalt fragments, basaltic minerals, and composites derived from them, and has an 8% modal abundance of ilmenite in 90-150 µm range (Meyer, 2010).

1.2.2 Various materials, Apollo 17 sample 79221

Sample 79221 (Figure 1-1) is classified as a mature to very mature soil sample (Meyer 2010). A sprinkle mount (unsorted grains deposited on C-tape for identification) was prepared at Purdue University by Alexander Kling, who then selected individual grains for further analysis. These grains include ilmenite, olivine ($(Mg,Fe)_2SiO_4$), an agglutinate with a clinopyroxene-like composition (a silicate mineral with Al and a variety of other elements like Mg, Fe, and Ca), and a plagioclase ($(Na,Ca)(Si,Al)_3O_8$) grain that may be an agglutinate. Agglutinates are glass grains with fused soil components and were formed from impact melting (McKay et al., 1991). These materials, with their different compositions, exhibit different features, densities, and products of space weathering.

1.2.3 Zircon, Apollo 17 sample 72255, Civet Cat norite clast

The zircons in this study are sourced from the Apollo 72255 Civet Cat meta-norite (Figure 1-1), which was sourced in the landslide material at the bottom slope of the South Massif. The Civet Cat clast, which itself was in an impact breccia originally sourced from the Serenitatis impact event (Morgan et al., 1975; Wolfe et al., 1981), has signatures of being sourced from the deep crust of the Moon (James, 1983). Norite is a type of orthopyroxene-rich gabbro, and a rock type commonly found in the materials returned by the Apollo missions. This sample is of particular interest because of the ancient ages that come from different components (Meyer, 2010 and references therein), and do not represent the sampling of periods of bombardment like most lunar samples (Nemchin et al., 2008). These zircons were analyzed by Zhang et al. (2021) for their U-Pb isotopic composition using NanoSIMS. The zircons in this sample are small (10 to 20 μm), and therefore conventional SIMS does not have the required spatial resolution to obtain ages from individual age domains in the crystals, provide mixed signals, and thus cannot provide undiluted ages. The five oldest NanoSIMS zircon ages have a weighted mean Pb-Pb age of 4452±35 Myr ago, and define a concordant U-Pb average age of 4461±35 Myr ago, which is older than the previously reported age of this sample of 4417±6 Myr ago by Nemchin et al. (2009).

1.3 SPACE WEATHERING

Space weathering is the alteration of the upper surface of materials on airless bodies (such as the Moon and asteroids) due to the simultaneous effects of irradiation by galactic and solar cosmic ray particles and solar wind, electromagnetic radiation from the Sun, and impacts from micrometeorites. These interactions cause physical and chemical alteration of the surface, impact vaporization, and ion sputtering and implantation, which leads to gardening and change in optical properties of the surface materials (Hapke, 2001; Chapman, 2004; Pieters and Noble, 2016). Products of space weathering include agglutinates, redeposition rims, microphase metallic iron (>40 nm, $mpFe^0$, also known as Britt-Pieters particles; Lucey and Noble, 2008), nanophase metallic iron (<40 nm, $npFe^0$; Lucey and Noble, 2008; Hapke et al., 2001), and vesicles filled with implanted solar wind. The abundance of these space weathering products depends on the composition of the soil grain (Zhang and Keller, 2011; Burgess and Stroud, 2018) as well as the distance from the Sun and the length of time it has been exposed to the space weathering environment (Zhang and Keller, 2011; Pieters and Noble, 2016).

In the space-weather affected area, Fe is reduced, and there is an Fe enrichment in rims due to the selective removal of lower mass atoms by sputtering processes (Bennett et al., 2013). Due to these $npFe^0$ and $mpFe^0$ particles, space weathered materials have reddened and darkened spectra relative to pristine samples in visible and near-IR (VNIR; Noble et al., 2001; Hendrix and Vilas, 2006; Starukhina and Shkuratov, 2011; Pieters and Noble, 2016; Raut et al., 2018).

Redeposition rims are thin zones on the outer surface of the grain that are compositionally distinct from the host grain and can have inclusions like $npFe^0$ (Pieters and Noble, 2016). Study of space mission-returned material from the surface of the Moon and asteroid Itokawa shows the presence of a single amorphous layer or complex rims, sometimes with gas-filled vesicles, on the surface of the studied grains (Keller and McKay, 1997; Noguchi et al., 2014). The $npFe^0$ particles present in these rims on lunar and Itokawa soil grains (e.g. inclusion-rich and complex rims on the lunar particles and redeposition and partially-amorphous rims on Itokawa particles) formed through a combination of deposition of the vapor produced during micrometeorite impacts, deposition of elements sputtered by solar wind, and thermally induced reduction during micrometeorite impact melting (Moroz et al., 1996; Keller and McKay, 1997; Noguchi et al., 2014; Pieters and Noble 2016). The total depth of these rims can be up to 200 nm (Keller and McKay, 1997) and it is difficult to differentiate the contributions from micrometeorite impacts from those of the solar wind ions in the formation of the rims. However, work by Zhang and Keller (2011) shows that micrometeorite impact is a dominant contributor to the deposition rims on lunar soil grains during the initial stages of space weathering.

Solar wind noble gases are implanted up to 150 nm deep, and solar wind-implanted H (present even deeper) could play a role in the development of $npFe^0$ within agglutinate glasses and formation of vesiculated rims on lunar and Itokawa soil grains (McKay et al., 1991, Keller and McKay, 1997; Pieters and Noble, 2016). This implanted H could also lead to the formation of water, which has implications for the availability of such a resource in future space missions.

1.4 ZIRCON GEOCHRONOLOGY

Among the many geochronometers, U-Pb in zircon ($ZrSiO_4$) is one of the most reliable for absolute age dating of early solar system events. During crystallization U is incorporated into the crystal lattice of zircon while Pb is excluded, therefore, the Pb present in the zircon should all be radiogenic. The two decay series used are ^{238}U ($t_{1/2} \approx 4.47$ Gyr) and ^{235}U ($t_{1/2} \approx 704$ Myr) which decay to ^{206}Pb and ^{207}Pb, respectively. By comparing these two systems, which should agree, a concordia age can be given. Despite its robustness, there are many mechanisms that could disrupt the system, such as metamictization, metamorphism, deformation, and melting (e.g., Hopkins and Mojzsis, 2015). The U-Pb ages of zircons can represent the true age of crystallization of the mineral and rock, an age associated with a metamorphic event, or have undergone a partial resetting of the system so that the age has no relevance. Therefore, the ages produced by this system must be carefully evaluated and contextualized.

Valley et al. (2014) presented the first results of APT of zircon. This work was particularly influential because it was able to leverage the technique's spatial resolution and compositional sensitivity to determine the distribution of individual atoms of Pb in Hadean zircon. These Jack Hills zircons, originally dated to 4.4 Ga using SIMS, are the oldest terrestrial mineral found to date, and had the potential to be exposed to a variety of processes that would have altered the U/Pb system. APT analysis of these zircons showed the presence of Pb nanoclusters, which, while radiogenic, formed later and in a closed system. In addition, these clusters occurred at a length scale that is smaller than the scale of the SIMS analysis spot, which makes the crystal appear homogeneous to SIMS, and thus they concluded that the 4.4 Gyr age of the zircon was real. The formation of zircons at 4.4 Gyr ago means solidification of the Earth's primordial magma ocean must have occurred before this date. In chapter 5, I apply this technique to ancient lunar zircons where I provide improved constraints on the timing of the Moon-forming Giant Impact Event and subsequent Lunar Magma Ocean.

1.5 SYNOPSIS OF CHAPTERS

Chapter 2 is a discussion of the methods used, with a focus on sample preparation for APT. Because this is a relatively new technique as applied to cosmochemical materials, a significant amount of technique development was required, and this is detailed therein.

Chapter 3, "Atom Probe Tomography of Space-Weathered Lunar Ilmenite Grain Surfaces," is a version of a manuscript I published under the same title in Meteoritics and Planetary Sciences with co-authors Surya S. Rout, Dieter Isheim, David N. Seidman, Rainer Wieler, and Philipp R. Heck (Greer et al., 2020). This work characterizes the first analysis of natural space weathering products by APT. The sample was obtained from a sub mature lunar soil collected by Apollo 17.

Chapter 4, "Nanoscale Space Weathering Feature of Mature Lunar Soils Using Correlated APT and TEM Analyses," is a version of a manuscript I am currently preparing for publication with co-authors Alexander Kling, Dieter Isheim, David N. Seidman, Michelle Thompson, and Philipp R. Heck. This work examines the products of space weathering with both TEM and APT in several different lunar materials from mature lunar soils collected in the Apollo program.

Chapter 5, "Atom Probe Tomography of 4.45 Ga Lunar Zircon from the Apollo 17 Civet Cat Norite Clast," is an expanded version of the manuscript "4.45 Ga Old Lunar Zircon Anchors Chronology of Lunar Magma Ocean," which I am preparing for publication with co-authors Bidong Zhang, Dieter Isheim, David N. Seidman, Audrey Bouvier, and Philipp R. Heck. This work confirms the oldest lunar zircon age to date by examining the nanoscale distribution of Pb and Y and presents its implications for lunar chronology.

1.6 REFERENCES

Alibert, C., M. D. Norman, and M. T. McCulloch. "An ancient Sm-Nd age for a ferroan noritic anorthosite clast from lunar breccia 67016." *Geochimica et Cosmochimica Acta* 58, no. 13 (1994): 2921-2926.

Apollo 17 Preliminary Examination Team. "Apollo 17 lunar samples: Chemical and petrographic description." *Science* 182, no. 4113 (1973): 659-672.

Benkert J., Baur H., Signer P., and Wieler R. “He, Ne, and Ar from the solar wind and solar energetic particles in lunar ilmenites and pyroxenes”. *Journal of Geophysical Research* 98 (1993): 13147.

Bennett, C. J., C. Pirim, and T. M. Orlando. "Space-weathering of solar system bodies: A laboratory perspective." *Chemical Reviews* 113, no. 12 (2013): 9086-9150.

Borg, L., M. Norman, L. Nyquist, D. Bogard, G. Snyder, L. Taylor, and M. Lindstrom. "Isotopic studies of ferroan anorthosite 62236: a young lunar crustal rock from a light rare-earth-element-depleted source." *Geochimica et Cosmochimica Acta* 63, no. 17 (1999): 2679-2691.

Boyet, M., and R. W. Carlson. "A highly depleted moon or a non-magma ocean origin for the lunar crust?." *Earth and Planetary Science Letters* 262, no. 3-4 (2007): 505-516.

Brandon, A. D., T. J. Lapen, V. Debaille, B. L. Beard, K. Rankenburg, and C. Neal. "Re-evaluating ^{142}Nd/^{144}Nd in lunar mare basalts with implications for the early evolution and bulk Sm/Nd of the Moon." *Geochimica et Cosmochimica Acta* 73, no. 20 (2009): 6421-6445.

Burgess, K. D., and R. M. Stroud. "Phase-dependent space weathering effects and spectroscopic identification of retained helium in a lunar soil grain." *Geochimica et Cosmochimica Acta* 224 (2018): 64-79.

Chapman, C. R. "S-type asteroids, ordinary chondrites, and space weathering: The evidence from Galileo's fly-bys of Gaspra and Ida." *Meteoritics & Planetary Science* 31, no. 6 (1996): 699-725.

Chapman, C. R. "Space weathering of asteroid surfaces." *Annu. Rev. Earth Planet. Sci.* 32 (2004): 539-567.

Deer, W. A., R. A. Howie, and J. Zussman. “An introduction to the rock forming minerals.” Harlow, UK. Longman Scientific & Technical. 1992.

Elkins-Tanton, L. T., S. Burgess, and Q.-Z. Yin. "The lunar magma ocean: Reconciling the solidification process with lunar petrology and geochronology." *Earth and Planetary Science Letters* 304, no. 3-4 (2011): 326-336.

Gaffney, A. M., and L. E. Borg. "Evidence for Magma Ocean Solidification at 4.36 Ga from ^{142}Nd-^{143}Nd Variation in Mare Basalts." In *Lunar and Planetary Science 45*, #1449. 2014.

Greer, J., S. S. Rout, D. Isheim, D. N. Seidman, R. Wieler, and P. R. Heck. "Atom probe tomography of space-weathered lunar ilmenite grain surfaces." *Meteoritics & Planetary Science* 55, no. 2 (2020): 426-440.

Halliday, A. N. "A young Moon-forming giant impact at 70–110 million years accompanied by late-stage mixing, core formation and degassing of the Earth." *Philosophical Transactions of the Royal Society A: Mathematical, Physical and Engineering Sciences* 366, no. 1883 (2008): 4163-4181.

Hapke, B. "Space weathering from Mercury to the asteroid belt." *Journal of Geophysical Research* 106, no. 5 (2001): 10-039.

Heiken, G., and D. S. McKay. "Petrography of Apollo 17 soils." In *Proceedings of the Lunar Science Conference*, vol. 5, pp. 843-860. 1974.

Hendrix, A. R., and F, Vilas. "The effects of space weathering at UV wavelengths: S-class asteroids." *The Astronomical Journal* 132, no. 3 (2006): 1396.

Hopkins, M. D., and S. J. Mojzsis. "A protracted timeline for lunar bombardment from mineral chemistry, Ti thermometry and U–Pb geochronology of Apollo 14 melt breccia zircons." *Contributions to Mineralogy and Petrology* 169, no. 3 (2015): 1-18.

Jacobson, S. A., A. Morbidelli, S. N. Raymond, D. P. O'Brien, K. J. Walsh, and D. C. Rubie. "Highly siderophile elements in Earth’s mantle as a clock for the Moon-forming impact." *Nature* 508, no. 7494 (2014): 84-87.

James, O. B. "Mineralogy and petrology of the pristine rocks." In *Pristine Highlands Rocks and the Early History of the Moon*, LPI Technical Report 83-02. 1983.

Keller, L. P., and D. S. McKay. "The nature and origin of rims on lunar soil grains." *Geochimica et Cosmochimica Acta* 61, no. 11 (1997): 2331-2341.

Kleine, T., H. Palme, K. Mezger, and A. N. Halliday. "Hf-W chronometry of lunar metals and the age and early differentiation of the Moon." *Science* 310, no. 5754 (2005): 1671-1674.

Lucey, P. G., and S. K. Noble. "Experimental test of a radiative transfer model of the optical effects of space weathering." *Icarus* 197, no. 1 (2008): 348-353.

McKay, D. S., and R. J. Williams. "A geologic assessment of potential lunar ores, Space resources and space settlements." *NASA Spec. Publ* 428 (1977): 243.

McKay, D. S., G. Heiken, A. Basu, G. Blanford, S. Simon, R. Reedy, B. M. French, and J. Papike. "The lunar regolith." *Lunar sourcebook* 567 (1991): 285-356.

Meyer, C. “Lunar Sample Compendium.” http://curator.jsc.nasa.gov/lunar/compendium.cfm (2005-2012)

Meyer, J., L. Elkins-Tanton, and J. Wisdom. "Coupled thermal–orbital evolution of the early Moon." *Icarus* 208, no. 1 (2010): 1-10.

Morgan, J. W., H. Higuchi, and E. Anders. "Meteoritic material in a boulder from the Apollo 17 site: implications for its origin." *The Moon* 14, no. 3 (1975): 373-383.

Moroz, L. V., A. V. Fisenko, L. F. Semjonova, C. M. Pieters, and N. N. Korotaeva. "Optical effects of regolith processes on S-asteroids as simulated by laser shots on ordinary chondrite and other mafic materials." *Icarus* 122, no. 2 (1996): 366-382.

Morris R. V. “The surface exposure (maturity) of lunar soils; some concepts and Is/FeO compilation.” *Proceedings, 9th Lunar and Planetary Science Conference*, (1978) pp. 2287-2297.

Nemchin, A. A., R. T. Pidgeon, M. J. Whitehouse, Jeffrey Patrick Vaughan, and C. Meyer. "SIMS U–Pb study of zircon from Apollo 14 and 17 breccias: implications for the evolution of lunar KREEP." *Geochimica et Cosmochimica Acta* 72, no. 2 (2008): 668-689.

Nemchin, A., N. Timms, R. Pidgeon, T. Geisler, S. Reddy, and C. Meyer. "Timing of crystallization of the lunar magma ocean constrained by the oldest zircon." *Nature Geoscience* 2, no. 2 (2009): 133-136.

Noble, S. K., C. M. Pieters, L. A. Taylor, R. V. Morris, C. C. Allen, D. S. McKay, and L. P. Keller. "The optical properties of the finest fraction of lunar soil: Implications for space weathering." *Meteoritics & Planetary Science* 36, no. 1 (2001): 31-42.

Noguchi, T., T. Nakamura, M. Kimura, M. E. Zolensky, M. Tanaka, T. Hashimoto, M. Konno et al. "Incipient space weathering observed on the surface of Itokawa dust particles." *Science* 333, no. 6046 (2011): 1121-1125.

Nyquist, L. E., H. Wiesmann, B. Bansal, C-Y. Shih, J. E. Keith, and C. L. Harper. "146Sm-142Nd formation interval for the lunar mantle." *Geochimica et Cosmochimica Acta* 59, no. 13 (1995): 2817-2837.

Nyquist, L., D. Bogard, A. Yamaguchi, C-Y. Shih, Y. Karouji, M. Ebihara, Y. Reese, D. Garrison, G. McKay, and H. Takeda. "Feldspathic clasts in Yamato-86032: Remnants of the lunar crust with implications for its formation and impact history." *Geochimica et Cosmochimica Acta* 70, no. 24 (2006): 5990-6015.

Papike, J. J., L. Taylor, and S. Simon. "Lunar Minerals" *Lunar Sourcebook: A User’s Guide to the Moon* (1991): 121-181.

Pieters, C. M., and S. K. Noble. "Space weathering on airless bodies." *Journal of Geophysical Research: Planets* 121, no. 10 (2016): 1865-1884.

Rankenburg, K., A. D. Brandon, and C. R. Neal. "Neodymium isotope evidence for a chondritic composition of the Moon." *Science* 312, no. 5778 (2006): 1369-1372.

Raut, U., P. L. Karnes, K. D. Retherford, M. W. Davis, Y. Liu, G. R. Gladstone, E. L. Patrick, Thomas K. Greathouse, A. R. Hendrix, and P. Mokashi. "Far-ultraviolet photometric response of apollo soil 10084." *Journal of Geophysical Research: Planets* 123, no. 5 (2018): 1221-1229.

Shearer, C. K., P. C. Hess, M. A. Wieczorek, M. E. Pritchard, E. M. Parmentier, L. E. Borg, J. Longhi et al. "Thermal and magmatic evolution of the Moon." *Reviews in Mineralogy and Geochemistry* 60, no. 1 (2006): 365-518.

Starukhina, L. V., and Yu G. Shkuratov. "Reduced iron grains from nano-to micron sizes in lunar and mercurian regoliths: Calculation of spectral effects." In *Lunar and Planetary Science 42*, (2011) no. 1608, p. 1144.

Touboul, M., T. Kleine, B. Bourdon, H. Palme, and R. Wieler. "Late formation and prolonged differentiation of the Moon inferred from W isotopes in lunar metals." *Nature* 450, no. 7173 (2007): 1206-1209.

Wolfe, E. W., N. G. Bailey, B. K. Lucchitta, W. R. Muehlberger, D. H. Scott, R. L. Sutton, and H. G. Wilshire. "The geologic investigation of the Taurus-Littrow Valley." *Apollo 17 landing site, with a section on Apollo 17 lunar surface photography* (1981).
Geol. Surv. Prof. Pap. (1981): 1080, pp. 280.

Zhang, S., and L. P. Keller. "Space weathering effects in soils lunar: Roles the of surface exposure time, and bulk chemical composition (abstract# 1947)." In *Lunar and Planetary Science 42*. 2011.

Zhang, B., Y. Lin, D. E. Moser, J. Hao, Y. Liu, J. Zhang, I. R. Barker, Q. Li, S. R. Shieh, and A. Bouvier. "Radiogenic Pb mobilization induced by shock metamorphism of zircons in the Apollo 72255 Civet Cat norite clast." *Geochimica et Cosmochimica Acta* 302 (2021): 175-192.

CHAPTER TWO: METHODS

2.1 INTRODUCTION

Sample analysis at the nanoscale requires sample preparation at the microscale. Extensive sample preparation is needed in APT predominantly with focused-ion beam methods. The sample preparation methods used for the work presented in here are based on established methods developed for site-specific atom probe tomography (Larson et al., 1999) but were further adapted for this project and influenced by the techniques described in Rout et al. (2017). It is important to note that flexibility and creativity are necessary when preparing atom probe samples of cosmochemical materials as they are often unique and each sample presents new and distinct challenges based on material properties, geometry and the goal of the analysis. Details specific to this project are outlined below.

2.2 SAMPLE CHARACTERIZATION

In a scanning electron microscope (SEM), primary electrons interact with the specimen and can excite electrons within the specimen, with weakly-bound electrons are emitted as secondary electrons that help image the topography of a sample and backscattered electrons that provide compositional contrast images of the sample (Goldstein et al., 2018). A field-emission SEM has a typical spatial resolution of ~1 nm (e.g., Nagatani et al., 1987), which is necessary for preparing the sample at the nm-scale. Carbon contamination by mobilization and redeposition of pre-existing hydrocarbons on the sample surface through electron beam exposure, a common issue in SEM (Stroud et al., 2014), must be minimized for APT applications as even a monolayer of C detected by the atom probe can make sample analysis more difficult. During APT analysis the C film does not have a uniform field-evaporation pattern. Since C requires a higher electric field to be field-evaporated than any other element, during analysis, this can result in an extreme field-evaporation contrast between C and other elements and can lead to catastrophic tip failure. Carbon deposition can be minimized by avoiding unnecessary imaging, imaging with a wide field of view, using faster scan speeds, and using a higher accelerating voltage. Systematic studies with different SEMs determined that a dwell time of < 0.1 s/μm^2 results in an average build-up of less than a monolayer of C (Stroud et al., 2014). These conditions help minimize the carbon deposition. Sources of carbon include the addition of carbon-rich gases with the gas injection system and dirty samples, and sample holders. Thus, it is important to use gloves, clean sample holders and samples to keep the SEM system as clean as circumstances allow.

Characterizing the sample is necessary prior to sample preparation, and I used two techniques in conjunction with SEM imaging, to aid in APT sample tip preparation. Energy-dispersive X-ray spectroscopy (EDS) was used to determine the sample's general elemental composition. In the work presented here, EDS was used to confirm the presence of major elements in the region of interest (ROI), so only qualitative measurements were necessary. Backscattered electrons (BSE) imaging was useful when the compositional contrast between two phases was high. Heavier elements appear brighter than lighter elements and BSE is therefore useful in differentiating between different minerals during sample liftout as well as identifying the Pt capping material and ROI during the final stages of tip sharpening. For a sample to be analyzed by APT, it must be shaped into a sharp and elongated nanotip to allow a later applied electric field to be strong enough to result in activation and field-evaporation of surface atoms (more details will be presented in section 2.4.). The apex of the needle needs to be more than 5 μm above any other sharp point that may also field evaporated in addition to the ROI (Larson et al., 2013). Thus, once an ROI is identified it must be either shaped into the required needle-shape *in situ* or lifted out from its original host sample onto on a suitable prefabricated tip and then shaped into the required geometry.

2.3 APT NANOTIP SAMPLE PREPARATION

To prepare samples for APT, we used the TESCAN LYRA3 FIB-SEM at the University of Chicago equipped with a Ga liquid-metal ion source, an Oxford Instruments Omniprobe-400 micromanipulator, and an Oxford Instruments OmniGIS gas injection system (GIS). For a successful APT analysis, a sample must be sharpened to a tip with a radius of no greater than 100 nm, although tips with smaller radii are recommended as field-evaporation will begin at lower voltages. There are two methods for creating such tip: electropolishing and focused ion beam (FIB) milling. Electropolishing, which forms a tip by moving a positively charged thin wire through an electrolyte solution, was the method by which the first tips for atom probe were made, but it is not suitable for many geo- and cosmochemical applications as the materials of interest are usually insulators, unlike the metal alloys analyzed by the first users of APT. Electropolishing also does not allow for site specificity. Instead, the tips presented in this work were produced by FIB milling. FIB works similar to SEM, but instead uses ions (the FIB used in this work uses a $^{69}Ga^{+}$ primary beam). FIB is used for both imaging and milling. Since in the instrument I used the FIB is mounted at a 55° angle to the electron beam, coordinated imaging using both of these beams is necessary for manipulating samples in 3D space. Both beams can be used for depositing Pt, which acts as both a glue and/or a protective layer during sample preparation. The gas injection system (GIS) pumps a Pt- and C-rich gas that deposits on surfaces that are exposed to either beam.

With the sample tilted so that it is normal to the FIB beam, an area is targeted for liftout and marked, usually by a protective GIS Pt layer (see below for details). The dimensions of this liftout depend on the ROI. There are two approaches to lifting out material from a sample that are used in this work: the lamella method and the spoke method, which describe the shape of the material that is lifted out. The initial stages of the lamella method are similar to that of TEM sample preparation, and this method is more conventionally used in APT sample preparations. The advantages to this include minimizing sample handling (where every step represents a point where the sample could be lost) while maximizing the number of tips that are produced.

This method is used when the ROI (Figure 2-1, red) is at the surface or is not site-specific. A rectangular area is coated with protective capping material (Figure 2-1, black). The dimensions of this rectangle can vary, but 1 µm in width is preferred for mounting on Si flat top posts so that it matches the dimensions of the mounting post. The lamellae lifted-out in this study are 10–15 µm in length. The liftout can be longer, with as many as ~1 tip per µm produced.

The material around the area that has been marked for analysis must be removed to lift out the ROI. For many FIB/SEM setups, there are formulaic recipes for milling away this area that are

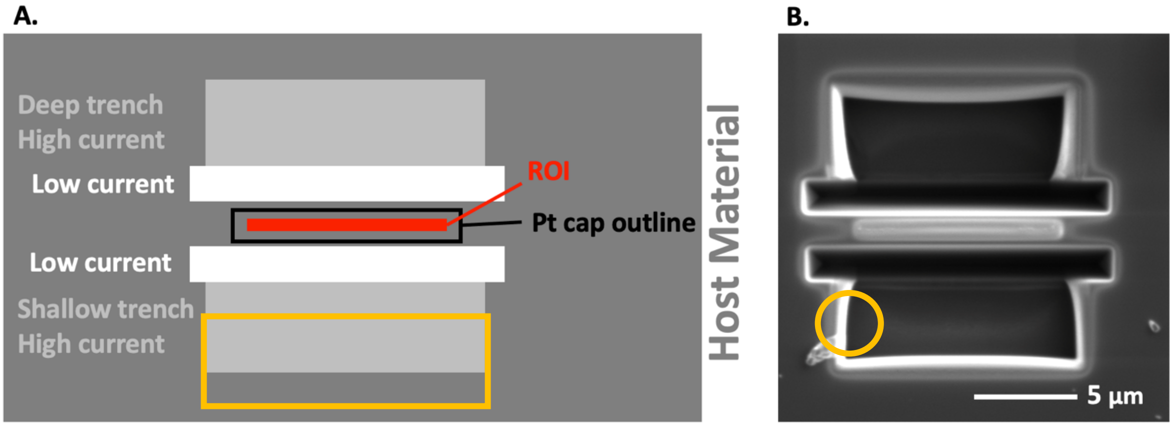

Figure 2-1: Schematic (A) and SEM image (B) showing the protective Pt cap and initial milling of trenches for a lamella liftout. The light gray rectangles represent the areas that are milled with a higher current beam (the depth of the trenches is addressed in Figure 2-2). The white rectangles represent areas closer to the ROI that should be milled using lower currents. The images show areas (B; circled, yellow) where material was re-deposited in the high current trenches (A; yellow outline) during the milling of the low current trenches, rounding the initial rectangle shape.

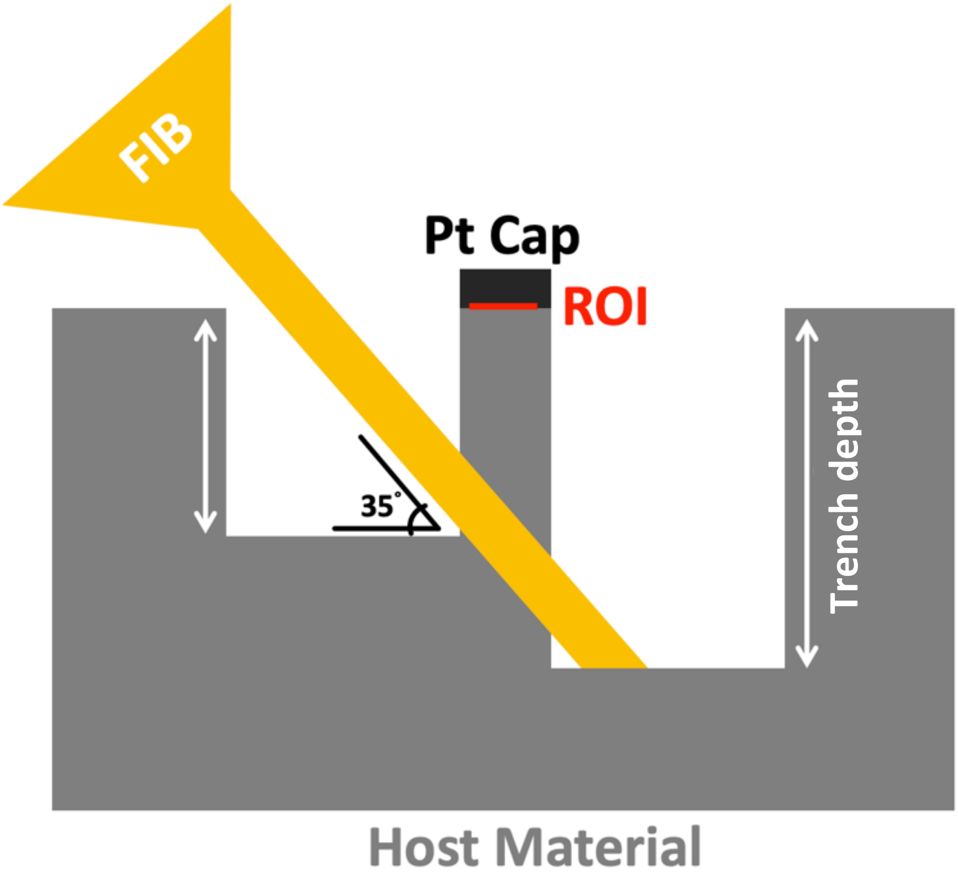

Figure 2-2: A simplified schematic showing a cross-section (z-direction relative to Figure 2-1) of the undercut made during lamella liftout.

included in the software, but if there is interest in consuming as little sample as possible, these pre-made conditions usually mill away more material than is necessary. Because of this, each individual lift-out in this work had different conditions and different dimensions. Rough milling, which involves removing the bulk of the sample from around the ROI, was done with FIB currents from 0.5 – 10.0 nA. For the higher end of this range, given a lamella with dimensions of 1 × 10 µm, this should be done at least 1 µm away (y-direction in Figure 2-1) from the ROI and be longer than the ROI by about 1 µm on either side. This has also been successful with the lowest end of the current range, milling away material right up to the edge of the ROI. Lower currents, 100 – 500 pA, are used to mill away material surrounding the ROI up to the edge of the Pt deposit. The depth of these trenches can vary from several to ten μm, but the trench depths on each side of the ROI do not have to be the same, as the undercut to lift out the ROI will be at an angle and accounting for this can save time during this step (Figure 2-2).

The spoke method is the best way to lift out material in cases where the ROI is site specific in all dimensions or consuming as little material as possible is desired. In the spoke method, the material to be lifted out is capped with GIS Pt, and then annularly milled around the ROI (Figure 2-3). With a ROI 1 μm in diameter, a milling annulus as small as 3 μm in diameter can be enough to extract the grain, minimizing sample consumption. This technique is also useful when there is significant topography (such as in Figure 2-3) on the grain's surface.

After these preparations, the sample is tilted back so that it is perpendicular to the electron beam. This exposes the side of the lamella/spoke so that it can be cut out. In the case of the lamella method, the edge of the lamella closest to the micromanipulator is milled away so that it is no

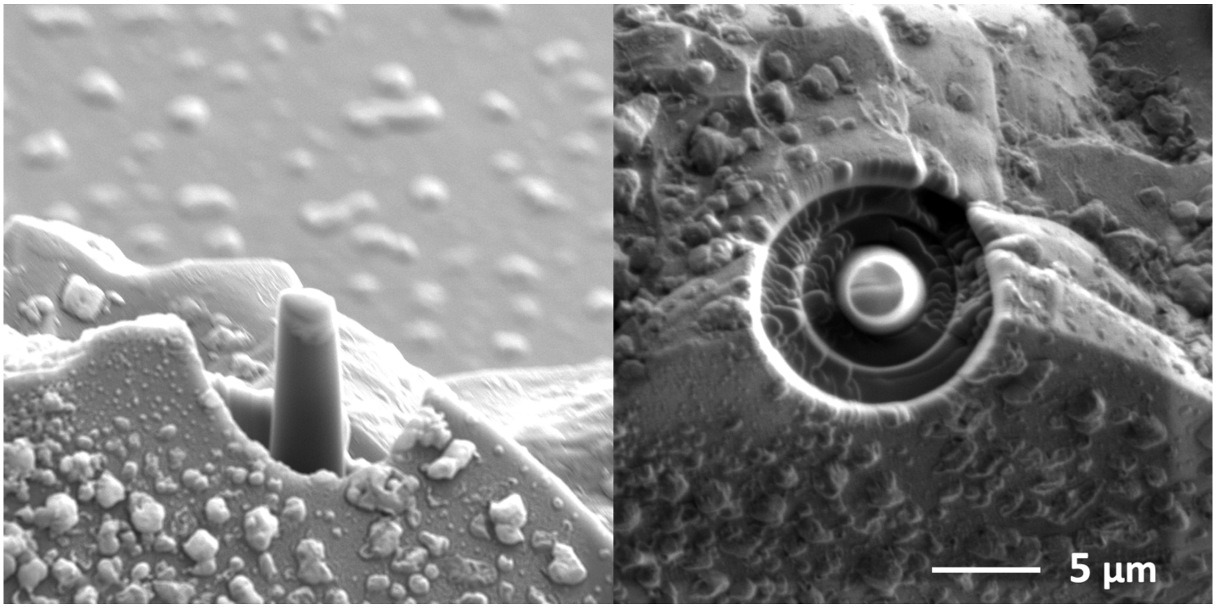

Figure 2-3: SEM images (left, sample tilted 55° and right, sample not tilted) of a spoke that has been milled into the host material. In this instance, the ROI is located on the ridge of a grain, so this method was chosen in order to preserve as much of the grain as possible while adapting to the geometry of the sample. In the left image, the Pt cap is differentiated from the host material by its slightly lighter color.

longer attached to the substrate and is then undercut the entire length of the lamella (Figure 2-2). Care must be taken in order to make sure that this cut goes all the way through. The success of this undercut can be assured by making the undercut tall enough, as a thin cut could lead to redeposition of material at the edges. A micromanipulator is inserted and then welded with GIS Pt to the sample. In the spoke method, the bottom part of the spoke is undercut. Micromanipulator drift may lead to the Pt weld being broken, which could also lead to sample loss, so the choice in beam current must balance the need to detach the sample gently with a lower current and the need to detach the sample quickly with a higher current, thus a current of ~100 pA is recommended. Once the ROI has been lifted out, it must be re-attached to an appropriate mount for the tip making process and subsequent APT analysis.

The mount type that was most used for my APT work was a grid of flat-topped Si microtips. These flat-tops have a circular top surface of ~ 1–2 μm across, and their profile allows for easy navigation while in the atom probe's analysis chamber. For spoke liftouts, the base of the sample

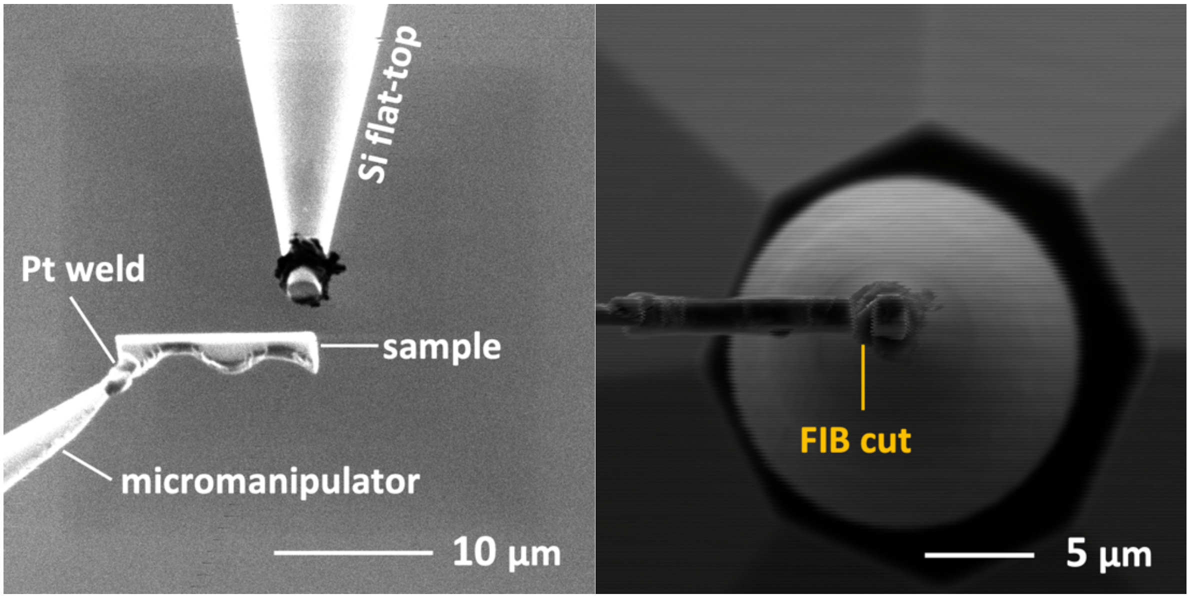

Figure 2-4: Labeled SEM images of the mounting process. To the left is a FIB image showing the sample being lowered physically (but raised in the image) to the Si flat-top. The edge of this lamella is mounted with Pt, and the rest is cut away as seen to the right.

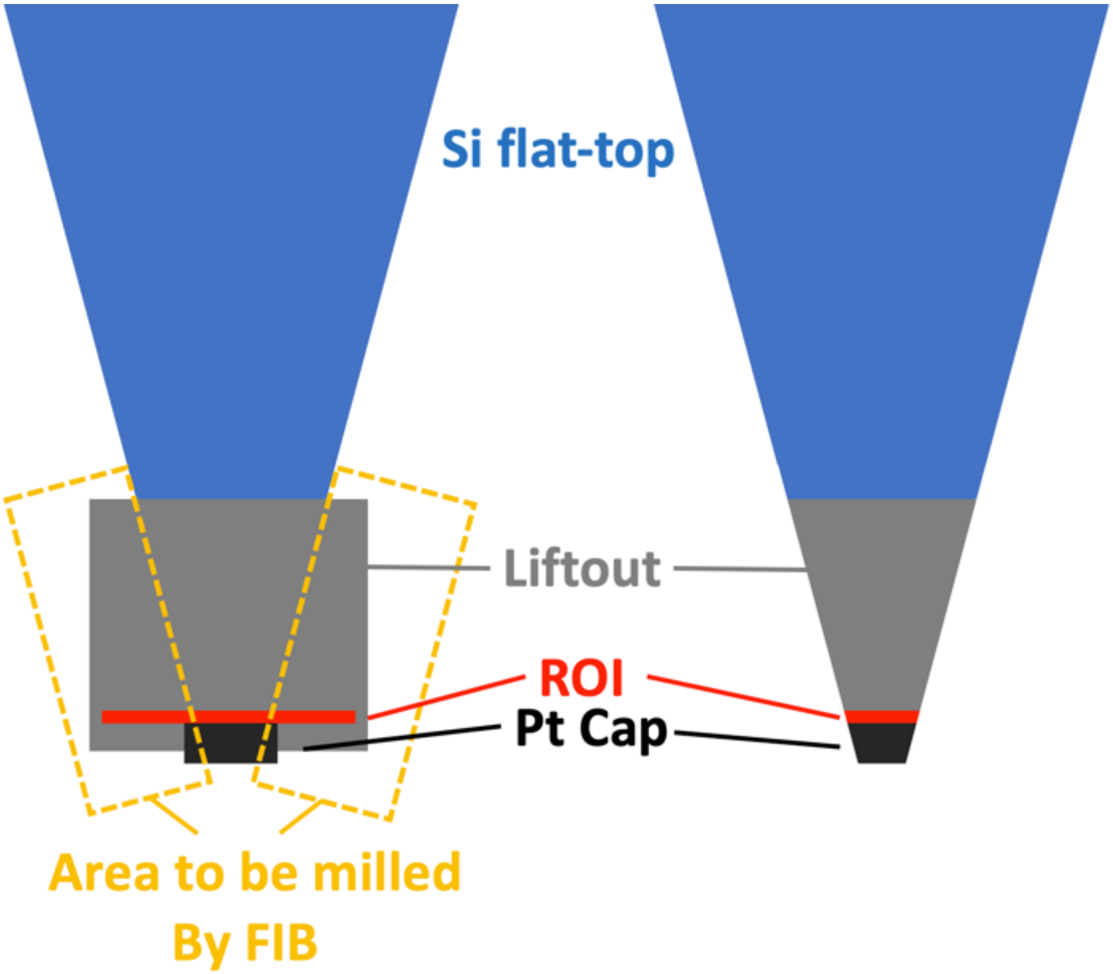

Figure 2-5: A schematic as seen with the FIB of the initial tip shaping process after a subsection of the lamella (gray) has been mounted onto the Si flat-top post (blue). The FIB is repeatedly scanned across the area outline in yellow (with this setup, using the program DrawBeam) to mill this material away. This is done again after the sample is rotated 90° to form a square pyramid. The apex of the pyramid should still contain some of the protective capping material, as seen to the right in a schematic of the tip after milling.

can be welded to the flat-top and then cut away from the micromanipulator. For lamella liftouts, only the edge of the lamella that is furthest away from the micromanipulator is welded to the flat-top (Figure 2-4, left), and then the lamella itself is cut so that only a section remains on the flat-top (Figure 2-4, right), with the rest of the lamella still attached to the micromanipulator. This is repeated until the lamella has been fully distributed in chunks on multiple flat-tops. As before, these cuts should be done with beam conditions that cut the material quickly while minimizing excessive damage (e.g. 30 keV, 100–500 pA). Once the micromanipulator has been retracted, it is usually necessary to reinforce the welds with more Pt. At minimum, the sample should be rotated 180°, and the back side reinforced with Pt. For some samples it may be necessary to rotate the sample 90° and deposit on all 4 sides. This is the case when the base of the sample has an irregular shape; if it has been cut out by the FIB so that there is a large wedge, it is only necessary to fill this wedge.

Once the sample is sufficiently well attached to the flat-top, it can be shaped to a point that is sharp enough for field-evaporation. Depending on the size and composition of the material, the ion beam should be 15–30 keV, 35–100 pA. The chunk should be milled on all four sides to a square pyramid shape with a top length of 0.2–0.5 μm and a base length equivalent to the diameter of the Si post (Figure 2-5). In order to get a sufficiently long and sharp tip, it may be necessary to thin the Si post as well. Tips can be successful if the Si post is thinned, but it is better to have the sample/flat-top contact as large as possible for stability during atom probe analysis. The ROI should be below the apex of the pyramid just below a protective Pt cap. Once the sample is in the shape of a square pyramid, the sample is then rotated so that the FIB has a top-down view of the tip. Similar to the process of creating a spoke as described above, an annular milling pattern is used to sharpen the tip with the FIB. This should be done with a low-current (10–100 pA, depending on the material) and ideally a low-voltage beam (≤ 10 keV) with the annulus centered on the top of the pyramid. The inner diameter of the annulus should be 0.05–0.2 μm, and the outer diameter of the annulus should be large enough so that secondary tips are not produced within 5 μm of the apex (and therefore susceptible to being evaporated during atom probe analysis). The final polishing step requires a circular milling pattern using a low-current, low-voltage beam (5 keV, 30 pA) that is centered on the tip and used to sharpen the tip to its final diameter with the

ROI in the apex as well as remove Ga implantation damage. At this point, the milling should be constantly monitored to prevent milling of the ROI. An in-beam BSE detector can be useful to observe the position of the protective Pt cap. After this final polishing step, the tip should have an apex radius as small as possible, and no larger than 100 nm (for some materials, this radius is too large and the sample will not field-evaporate).

Lastly, secondary electron images of the finished tips need to be acquired in the SEM using the electron beam. These images are later used during geometric data reconstruction of the atom probe data. At this point, imaging with the electron beam should be kept to a minimum to prevent the deposition of C, and imaging with the FIB must be avoided completely. A sufficiently sharp tip may be charging in the electron-beam image. Two images should be taken: the first image should be at high enough magnification so that the dimensions of the tip (radius, shank angle) can be accurately measured. The second image should be at lower magnification to capture both the material-Si boundary and at least 5 μm of the tip below the apex to verify the absence of any secondary tips. Both images will be essential for comparisons to tip images at the same magnifications after APT analysis to measure the depth analyzed and, in case of tip failure, to aid in determining the cause of failure.

During the sample preparation process, the Ga from the FIB can implant into the sample. This implantation must be minimized as much as possible, as this implantation can mix, damage, or even amorphize the sample. This is minimized by using progressively lower voltages of the FIB beam during milling and sharpening. At the 30 keV shaping level, Ga can be implanted up to ~50 nm into the surface of the sample (Thompson et al., 2007) but this can be reduced to only several nm with an accelerating voltage of 5 keV, which is used in the final stage of polishing. GIS Pt is also used to cap the sample and protect it. An initial, thin layer of electron beam-deposited Pt protects the sample during ion beam deposition, as Pt is deposited much faster with the ion beam and is therefore used during lift out and welding stages.

GIS Pt is commonly used to protect the surface of a sample from damage by the FIB beam during the sample preparation process. However, this is not an ideal capping material, as the deposited Pt is deposited along with C (from the precursor gas) which is known to have an irregular, "bursty" field-evaporation (Andrén et al., 1980) behavior during APT analysis. One important consideration in selecting capping material is to select one that avoids or minimizes isotopic peak overlaps in the mass spectrum with peaks of interest in the sample. Monoisotopic elements can be ideal for this, but the coating material must be able to adhere well to the sample and behave well during field-evaporation in the APT. For this reason, Au, which has a very low field-evaporation threshold compared to other elements, but is commonly used to coat samples for SEM or SIMS analysis, is not an ideal material for use in APT. For the submature lunar ilmenite with a ROI at the surface (i.e. the space-weathered surface), a sputter-deposited coating layer of Ni was deposited onto the sample (~50 nm thick), which is then capped by GIS Pt (1–2 μm thick). For most samples analyzed in this work, the tip can be successfully measured in the atom probe with a small amount Pt cap remaining, but in the case of some minerals such as feldspar, the Pt cap must be entirely removed as the voltage required to field-evaporate the Pt is higher than that of the feldspar, and the electric field will be too high for stable feldspar field-evaporation at the transition between cap and ROI.

Finished tips should be moved into ultra-high vacuum as soon as possible. Prolonged exposure to the atmosphere can result in the oxidation of the outermost surface, which will usually make the tip more difficult to evaporate and can result in premature tip failure. For samples where H species are of interest, exposure to air with high relative humidity should be minimized. This can be most easily controlled by transporting the tips in a portable vacuum or nitrogen chamber. Though some minerals (in this work, zircons) only need to be transported with desiccant if they are already oxides or otherwise not particularly susceptible to oxidation, or if there is no potential peak overlap in the mass spectrum between possible adsorbed species and species of interest. We used a portable vacuum chamber to transport the samples most susceptible to oxidation.

2.4 ATOM PROBE TOMOGRAPHY ANALYSIS

2.4.1. A brief introduction to APT

The ultimate goal of analytical instrumentation is to fully characterize every single atom in a sample. Currently, atom probe tomography (APT) is the closest we have gotten to this goal of characterizing the elemental and isotopic compositions of individual atoms within a sample in 3D. APT is a type of time-of-flight mass spectrometry that analyzes a sample atom by atom with a high detection efficiency (up to 80% of all atoms in a sample), sensitivity and spatial resolution. Both the position in the sample and mass-to-charge state of a single atom can be measured, allowing for a 3D reconstruction of a sample, complete with the compositional and/or isotopic information of every ion that has been detected. APT reaches a range of compositional spatial resolution and sensitivity that other instruments (such as TEM and NanoSIMS) cannot reach (e.g. Reddy et al., 2020) and is thus a uniquely powerful technique. However, any analytical technique is made more useful by correlative and coordinated analysis. For example, NanoSIMS has a higher mass resolving power, TEM can provide structural information, and both of these techniques are able to analyze larger volumes of a sample where APT is limited to a smaller volume analyzed. The work contained herein demonstrates how these techniques complement each other while focusing on the details of the APT analysis of these samples.

The atom probe was invented in 1967 (Larson et al., 2013), but its use in geo- and cosmochemistry begins in the 21st century. The work of Valley et al. (2014) was instrumental in validating the U-Pb age of the Earth's oldest zircon by using APT to map the Pb distribution inside the grain. Since then, APT has been used on ancient zircons and baddeleyites in order to develop a context for these ages (e.g. Reddy et al., 2016, White et al., 2019), and this application is likely to become even more widespread in the future. Cosmochemical studies with APT include meteoritic nanodiamonds (Heck et al., 2014[1], Lewis et al., 2015), the interface between kamacite and taenite in iron meteorites (Rout et al., 2017), and refractory metal nuggets from meteorites (Daly et al., 2017). A more comprehensive list of studies using APT for geo- and cosmochemical samples can be found in Reddy et al. (2020).

In APT, a high electric field (2–10 kV) is applied to a very sharp sample tip, and a pulsed laser or high voltage pulse field-evaporates and field-ionizes individual atoms. The outermost atoms are removed from the top of the sample, so the tip can be reconstructed in three dimensions (Larson, 2013). These ions are then accelerated through the local electrode and detected by a position-sensitive time-of-flight mass spectrometer. A local electrode is a negatively-charged funnel that accelerates the evaporated ions to a microchannel plate which detects the desorbed ion records its position and detects the electron cascade triggered by the incoming ion. While the time for the ion to reach the detector corresponds to the ion's mass to charge state ratio (Kelly and Miller, 2007). Chemical information is discerned from mass-to-charge ratios (Seidman and Stiller, 2009). Therefore, APT provides both the composition and distribution of the atoms in this sample, allowing for 3D reconstruction of elemental and isotopic information.

---

[1] This is the paper that sparked my interest in this field, and without it, this work would not exist.

2.4.2 Using the atom probe tomograph

The atom probe used for this work was the LEAP 4000X Si, which was later upgraded to the LEAP 5000XS tomograph at the NUCAPT facility of Northwestern University. This upgrade increased the detection efficiency from ~50% to ~80%. There are two ways to achieve field evaporation in APT: laser-pulsed mode and voltage-pulsed mode. Field-evaporating atoms by using voltage pulses limits the materials that can be analyzed to electrical conductors and heavily doped semiconductors (Shariq et al., 2009). The use of laser pulsing allows for the analysis of insulator samples that cannot transmit a voltage pulse (Kellogg and Tsong, 1980). In materials science, minerals such as silicates and oxides are considered resistive or insulative relative to materials such as metals. It should be noted, however, that the surface of resistive materials become conductive in a high electric field, as is the case in the atom probe where a high electric field allows for desorption of the material (Miller and Forbes, 2014). The laser is focused to a spot size of less than 3 µm to minimize sample heating as much as possible. This small size means that only a small volume of the sample is heated and therefore will cool quickly— this is important in reducing thermal tails in the mass spectrum. Thermal tails can form when the heated volume is so large that the arrival times at the detector of field-evaporated ions from proximal to distal positions in the heated volume are noticeably different and cause asymmetric peak broadening in the mass spectrum. In general, the mass resolving power of APT is limited by thermal effects on the mass spectrum (Larson et al., 2013), and given the low thermal conductivity of the minerals in this study, some thermal tails are unavoidable and result in peak overlaps that cannot be resolved.

Larson et al. (2013) recommends that when starting analysis with a new material, best practice is to “assume that the new material type is difficult to field evaporate.” Apart from zircon, which has been extensively analyzed by others (Reddy et al., 2020) each individual tip was treated as a challenging “new” material. The run conditions chosen generally prioritized sample stability. A low base temperature of 30–50K was used in order to maximize heat flow, thereby reducing thermal tails in the mass spectra. The pulse energy was also chosen as to reduce heating and was set to between 40–50 pJ. In general, a low base temperature and pulse energy leads to better spatial and spectral resolution, where a high base temperature and pulse energy leads to a better yield. The pulse rate for all samples was set to 250 kHz. In general, a low pulse rate is better for materials with low thermal diffusivity. The initial detection rate (the percentage of laser pulses that lead to a detection on the multichannel plate) ranged from 0.01–0.1% and was slowly increased until the tip reached steady state field-evaporation. From then, the detection rate was increased in intervals of 0.1%, and never exceeded 1%. This is done primarily to collect as much data as possible within a reasonable timeframe without leading to tip failure (increasing the detection rate above 1% was likely to result in tip failure).

During tip analysis, the DC voltage slowly increases in order to reach the targeted detection rate. During data acquisition, tips were constantly monitored to watch for any sudden changes in field-evaporation pattern. Data acquisition ended if the target number of ions was reached or if the tip fractured. The target number of atoms can be specified in the acquisition software, but for these samples, this feature was not used. Instead, runs were stopped manually after the region of interest had been analyzed; in the case of space weathered samples, this happened when field-evaporation reached the unaltered part of the grain. If the voltage increased to the point where the local electrode became noisy (resulting from emission from surface defects on the electrode that cause hotspots on the detector image, unrelated to the sample), the run was ended and the electrode was exchanged with a freshly polished one, but in general the tips fractured before this point. For the space weathered samples, tip fracture was usually due to a compositional interface that drastically/overly changed the electric field needed for field evaporation or if the tip contained a large vesicle that changed the geometry of the tip. A large electrical discharge at the tip results in significant melting so that the entire sample and most of the Si flat top are lost, as determined with post-analysis, "post-mortem" SEM imaging. If the data acquisition run was stopped prior to tip fracture, the remainder of the tip can then be reimaged in the SEM for more information on the volume that was analyzed, and to provide further constraints on the reconstruction (Figure 2-6).

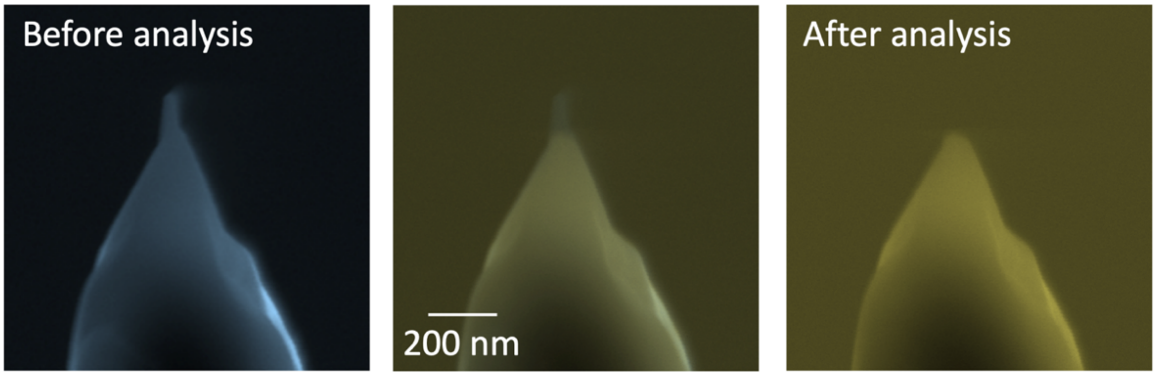

Figure 2-6: A false-color SEM image of a zircon tip before (left) and after (right) APT analysis (middle- composite). The length of the tip that was evaporated can be measured using these images, and therefore leads to a more accurate reconstruction. The wide base of the tip allows for more efficient heat flow and will therefore lead to a more stable tip. However, once the sharp part has been analyzed, the rest of the tip will need to be reshaped in the FIB for further analysis.

2.4.3 Data analysis

APT data sets are reconstructed using the Integrated Visualization and Analysis Software (IVAS) developed by CAMECA. The software is used prepare tomographic reconstructions from the raw dataset and to calibrate the mass spectra. During data reconstruction, tip radius and half-shank angle (Figure 2-7) are used to model the geometry of the tip. These parameters are determined from the pre-APT SEM images (Figure 2-6) analyzed using the image processing package Fiji (Schindelin et al., 2012). The IVAS software visualizes the reconstructed tips as color-coded 3D point clouds of nuclides and molecular species. Functionality includes displaying concentration interfaces, drawing regions of interest (ROIs), generating concentration and nearest neighbor profiles, and individually range each mass-to-charge state peak as appropriate. IVAS

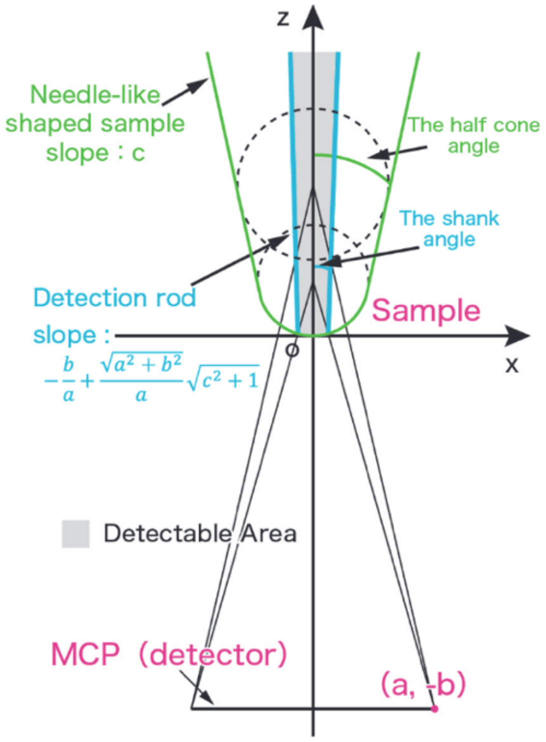

Figure 2-7: Schematic of tip geometry used in reconstruction from Yukawa et al. (2015).

can generate both time-of-flight and mass spectra, provide a simple background correction and export data tables containing ion counts assigned to specific nuclides and molecular species. For this work, only the mass-to-charge state spectra of the tips and subsets therein were used.

These spectra are plotted in log scale and without background correction in this work since the patterns that emerge from the background show how the analytical conditions affected the tip, which can help with interpreting the data. The background correction is linear: 3 to 5 data bins (with a size of 0.001 Da) to either side of a peak are averaged to calculate the base value. The average of these two points is then used as the background value for each data bin and subtracted over the width of the peak.

The width of each peak is determined individually, as the peak shapes are not regular or symmetrical, even within the same run. The beginning of the peak is determined by a sharp increase from noise, whereas the end of a peak can be harder to determine as thermal tails distort the peak shape. In this work, the end of the peak was determined by the slope reaching ~45°, and thus do not include the thermal tail. This definition of peak widths is called ranging of peaks and is done consistently throughout a every run in a project and are therefore standardized in this way.

Peaks are identified through both a material's nominal abundance and the relevant isotopic abundance pattern (mainly terrestrial or solar). Qualitative EDS analysis is useful for major elements, which can then be compared to the mass spectra produced by APT. Minor elements can be identified through analyses of the bulk soil, which can be useful for redeposition rims. This pattern can also be distinguished in the molecular ions and their different charge states that are formed during analysis; oxides are the most common. In general, peak labeling is best done with proper context of the sample – even qualitative EDS will be very helpful for determining which elements may be present. Isotopic abundances are also used in deconvolving isobaric peak overlaps. Elements can appear in the mass spectrum with different mass-to-charge state ratios. For example, Mg and Si have their highest peaks (with the analytical conditions used in this work) at 12, 12.5, 13 and 14, 14.5, 15. These correspond to $^{24}Mg^{2+}$, $^{25}Mg^{2+}$, $^{26}Mg^{2+}$ and $^{28}Si^{2+}$, $^{29}Si^{2+}$, $^{30}Si^{2+}$, respectively. Al, if present, can appear as triply charged ($^{27}Al^{3+}$) with a mass-to-charge ratio of 9, but other species are generally only common as doubly or singly charged. The ratio of singly-to-doubly charged ions of the same element or molecule can somewhat be controlled by the laser energy and is a proxy for the similarity of analytical conditions between different runs and datasets.

Mass spectra of bulk and subsets of the data is exported as a data table that includes the counts from every mass-to-charge state value, in our project we chose values from 0 to 400, with bin widths of 0.001 Da. Concentration profiles that show composition vs. depth are generated from a cylinder down the length of the tip for our datasets. Data is exported as a table with distance bins in widths of 1 nm and the abundances of all species that have been selected and ranged.

The errors are determined by Poisson counting statistics: $n \pm \sqrt{n}$ (Tsong et al., 1987). This error is propagated through any calculation. In time-of-flight mass spectrometry techniques such as APT, dead time, or the time after detection before the detector can detect another event, may need to be corrected for (Stephan et al., 2015). The effects are mainly important for isotope ratios of low-mass elements and are not important for the ion species of interest in samples of our study.

2.5 REFERENCES

Andrén, H. O., A. Henjered, and H. Norden. "Composition of MC precipitates in a titanium stabilized austenitic stainless steel." *Journal of Materials Science* 15, no. 9 (1980): 2365-2368.

Daly, L., P. A. Bland, D. W. Saxey, S. M. Reddy, D. Fougerouse, W. D. A. Rickard, and L. V. Forman. "Nebula sulfidation and evidence for migration of "free-floating" refractory metal nuggets revealed by atom probe microscopy." *Geology* 45, no. 9 (2017): 847-850.

Goldstein, J. I., Newbury, D. E., Michael, J. R., Ritchie, N. W., Scott, J. H. J., & Joy, D. C. "Scanning electron microscopy and X-ray microanalysis." Springer Nature, New York, 550 pp. (2017).

Heck, P. R., F. J. Stadermann, D. Isheim, O. Auciello, T. L. Daulton, A. M. Davis, J. W. Elam C. Floss, J. Hiller, D. J. Larson, J. B. Lewis, A. Mane, M. J. Pellin, M. R. Savina, D. N. Seidman, and T. Stephan. "Atom-probe analyses of nanodiamonds from Allende." *Meteoritics & Planetary Science* 49, no. 3 (2014): 453-467.

Kellogg, G. L., and T. T. Tsong. "Pulsed-laser atom-probe field-ion microscopy." *Journal of Applied Physics* 51, no. 2 (1980): 1184-1193.

Kelly, Thomas F., and Michael K. Miller. "Atom probe tomography." *Review of Scientific instruments* 78, no. 3 (2007): 031101.

Larson, D. J., D. T. Foord, A. K. Petford-Long, H. Liew, M. G. Blamire, A. Cerezo, and G. D. W. Smith. "Field-ion specimen preparation using focused ion-beam milling." *Ultramicroscopy* 79, no. 1-4 (1999): 287-293.

Larson, D. J., T. J. Prosa, R. M. Ulfig, B. P. Geiser, and T. F. Kelly. "Local Electrode Atom Probe Tomography." Springer, New York, NY, 2013.

Lewis, J. B., D. Isheim, C. Floss, and D. N. Seidman. "^{12}C/^{13}C-ratio determination in nanodiamonds by atom-probe tomography." *Ultramicroscopy* 159 (2015): 248-254.

Miller, M., and R. Forbes. "Atom-probe tomography: the local electrode atom probe." Springer. (2014).

Nagatani, T., S. Saito, M. Sato, and M. Yamada. "Development of an ultra high resolution scanning electron microscope by means of a field emission source and in-lens system." *Scanning Microscopy* 1, no. 3 (1987): 3.

Reddy, S. M., A. van Riessen, D. W. Saxey, T. E. Johnson, W. D. A. Rickard, D. Fougerouse, S. Fischer, T. J. Prosa, K. P. Rice, D. A. Reinhard, Y. Chen, D. Olson. "Mechanisms of deformation-induced trace element migration in zircon resolved by atom probe and correlative microscopy." *Geochimica et Cosmochimica Acta* 195 (2016): 158-170.

Reddy, S. M., D. W. Saxey, W. D. A. Rickard, D. Fougerouse, S. D. Montalvo, R. Verberne, and A. van Riessen. "Atom probe tomography: Development and application to the geosciences." *Geostandards and Geoanalytical Research* 44, no. 1 (2020): 5-50.

Rout, S. S., P. R. Heck, D. Isheim, T. Stephan, N. J. Zaluzec, D. J. Miller, A. M. Davis, and D. N. Seidman. "Atom-probe tomography and transmission electron microscopy of the kamacite–taenite interface in the fast-cooled Bristol IVA iron meteorite." *Meteoritics & Planetary Science* 52, no. 12 (2017): 2707-2729.

Schindelin, J., I. Arganda-Carreras, E. Frise, V. Kaynig, M. Longair, T. Pietzsch, S. Preibisch, C. Rueden, S. Saalfeld, B. Schmid, J.-Y. Tinevez, D. J. White, V. Hartenstein, K. Eliceiri, P. Tomancak, and A. Cardona. "Fiji: an open-source platform for biological-image analysis." *Nature Methods* 9, no. 7 (2012): 676-682.

Seidman, D N, and K Stiller. 2009. "An Atom-Probe Tomography Primer." *MRS Bulletin* 34.717-721.

Shariq, A., S. Mutas, K. Wedderhoff, C. Klein, H. Hortenbach, S. Teichert, P. Kücher, and S. S. A. Gerstl. "Investigations of field-evaporated end forms in voltage-and laser-pulsed atom probe tomography." *Ultramicroscopy* 109, no. 5 (2009): 472-479.

Stephan, T., P. R. Heck, D. Isheim, and J. B. Lewis. "Correction of dead time effects in laser-induced desorption time-of-flight mass spectrometry: Applications in atom probe tomography." *International Journal of Mass Spectrometry* 379 (2015): 46-51.

Stroud, R. M. et al. "Stardust Interstellar Preliminary Examination XI: Identification and elemental analysis of impact craters on Al foils from the Stardust Interstellar Dust Collector." *Meteoritics & Planetary Science* 49, no. 9 (2014): 1698-1719.

Thompson, K., D. Lawrence, D. J. Larson, J. D. Olson, T. F. Kelly, and B. Gorman. "In situ site-specific specimen preparation for atom probe tomography." *Ultramicroscopy* 107, no. 2-3 (2007): 131-139.

Tsong, T. T., Yee S. Ng, and S. V. Krishnaswamy. "Quantification of atom-probe FIM data and an application to the investigation of surface segregation of alloys." *Applied Physics Letters* 32, no. 11 (1978): 778-780.

Valley, J. W., A. J. Cavosie, T. Ushikubo, D. A. Reinhard, D. F. Lawrence, D. J. Larson, P. H. Clifton, T. F. Kelly, S. A. Wilde, D. E. Moser, and M. J. Spicuzza "Hadean age for a post-magma-ocean zircon confirmed by atom-probe tomography." *Nature Geoscience* 7, no. 3 (2014): 219-223.

White, L. F., D. E. Moser, K. T. Tait, B. Langelier, I. Barker, and J. R. Darling. "Crystallization and impact history of a meteoritic sample of early lunar crust (NWA 3163) refined by atom probe geochronology." *Geoscience Frontiers* 10, no. 5 (2019): 1841-1848.

Yukawa, T., M. Morita, M. Karasawa, S. Ishimura, N. Mayama, H. Uchida, Y. Kawamura, K. M. Itoh, and M. Owari. "Reconstruction in atom probe tomography considering the cone angle of needle-like shaped samples and evaluation of reliability." *e-Journal of Surface Science and Nanotechnology* 13 (2015): 235-238.

CHAPTER THREE: ATOM PROBE TOMOGRAPHY OF SPACE-WEATHERED LUNAR ILMENITE GRAIN SURFACES

3.1 ABSTRACT

The surfaces of airless bodies, such as the Moon and asteroids, are subject to space weathering, which alters the mineralogy of the upper tens of nanometers of grain surfaces. Atom probe tomography (APT) has the appropriate 3-D spatial resolution and analytical sensitivity to investigate such features at the nanometer scale. Here, we demonstrate that APT can be successfully used to characterize the composition and texture of space weathering products in ilmenite from Apollo 17 sample 71501 at near-atomic resolution. Two of the studied nanotips sampled the top surface of the space-weathered grain, while another nanotip sampled the ilmenite at about 50 nm below the surface. These nanotips contain small nanophase Fe particles (~3 to 10 nm diameter), with these particles becoming less frequent with depth. One of the nanotips contains a sequence of space weathering products, compositional zoning, and a void space (~15 nm in diameter) which we interpret as a vesicle generated by solar wind irradiation. No noble gases were detected in this vesicle, although there is evidence for ^{4}He elsewhere in the nanotip. This lunar soil grain exhibits the same space weathering features that have been well documented in transmission electron microscope studies of lunar and Itokawa asteroidal regolith grains.

3.2 INTRODUCTION

Transmission electron microscope (TEM) studies of naturally and artificially space-weathered materials have led to better understanding of the formation process of the rims around space-weathered grains, but there are still some open questions that need to be investigated at near atomic spatial resolution, including (1) what is the depth concentration profile, at high spatial resolution, of implanted H, OH, and noble gases within the space-weathered rims; (2) what is the concentration of noble gases within vesicles in space-weathered rims; and (3) what is the composition of different elements within multilayered space-weathered rims. The new generations of probe-corrected scanning transmission electron microscopes equipped with electron energy loss spectroscope and atom probe tomography (APT) have the required spatial resolution to try to answer the above questions.

Ilmenite ($FeTiO_3$) is an opaque oxide mineral that is a common accessory phase in terrestrial igneous and metamorphic rocks (Deer et al., 1992) and can comprise up to about 20% of lunar soils (e.g., Papike et al., 1991). Ilmenite has been proposed as a building resource for a future lunar base, specifically as a source of Fe, Ti, O, and solar wind–implanted H (O'Neill et al., 1977; McKay and Williams, 1979; Papike et al., 1991). However, as a soil accumulates more and more agglutinates with increasing exposure to the space environment, the soil becomes harder to utilize as a resource (McKay and Williams, 1979), making it necessary to better understand space weathering processes. Elements other than Mg that are commonly found in terrestrial ilmenite (e.g., Cr, Mn, Al) are typically present only at minor or trace levels in lunar samples (Papike et al., 1991). Ilmenite is more retentive to solar wind–implanted He and Ne than plagioclase and other minerals (Signer et al., 1977), and is therefore a prime target to study implanted noble gases.

The noble gas composition of ilmenite in lunar soil has been well studied, as the isotopic composition of the noble gases can provide an unambiguous signature of the soil's interaction with the solar wind. Noble gas mass spectrometry coupled with extraction through both stepwise heating and acid etching suggested that the noble gases were located in the outermost grain layers (Benkert et al., 1993). TEM work with electron energy loss spectroscopy has shown that the helium present in the outermost rims of these grains is concentrated in vesicles and planar defects (Burgess and Stroud, 2018).

Atom probe tomography is an analytical imaging technique that is increasingly being used for geo- and cosmochemistry (e.g., Heck et al., 2014; Valley et al., 2014, 2015; Parman et al., 2015; Lewis et al., 2015; Peterman et al., 2016; Daly et al., 2017; Rout et al., 2017). APT is a technique complementary to TEM, in that it generates quantitative 3-D information with atom-by-atom distribution of elements, at a higher resolution for compositional data. In APT, atoms are field evaporated from the surface of a sample and detected by a position-sensitive time-of-flight mass spectrometer. This way, both the local compositions and spatial distributions can be determined in three dimensions (Seidman and Stiller, 2009; Blum et al., 2017). With APT, a sample volume of typically 100 nm in diameter can be analyzed at near atomic spatial resolution, which makes it ideal to study the nanoscale features formed by space weathering. Here, we present the first APT study from a naturally space-weathered sample.

3.3 SAMPLES AND METHODS

3.3.1 Lunar Dust Sample

Atom probe nanotips were prepared from a single ilmenite grain from Apollo 17 sample 71501, aliquot 284, separated for ilmenite grains 150–200 µm in diameter. Soil 71501 has been classified as submature (Heiken and McKay, 1974). It is composed of mainly basalt fragments and basalt minerals. Ilmenite comprises 8% modal content of the soil in the 90–150 µm range. This sample has been of great interest particularly due to its high solar wind content (e.g., Hintenberger et al., 1974; Signer et al., 1977; Frick et al., 1988; Benkert et al., 1993).

3.3.2 Sample Preparation

We selected a single grain with a diameter of about 130 µm from an ilmenite separate that had been prepared by hand picking from a grain-size separate obtained by sieving under ethanol (Benkert et al., 1993). The ilmenite separate and single grains thereof had been previously extensively studied for noble gas concentrations and isotopic compositions (e.g., Benkert et al., 1993; Wieler et al., 1996). These studies showed that essentially all grains from this sample contain solar wind–implanted noble gases.

The grain used for this study was pressed into indium on an SEM Al stub mount (Figure 3-1A). Some of this In was then pressed over the edges of the grain to secure it. The grain's composition was analyzed qualitatively with SEM-EDS to confirm that it was ilmenite. The

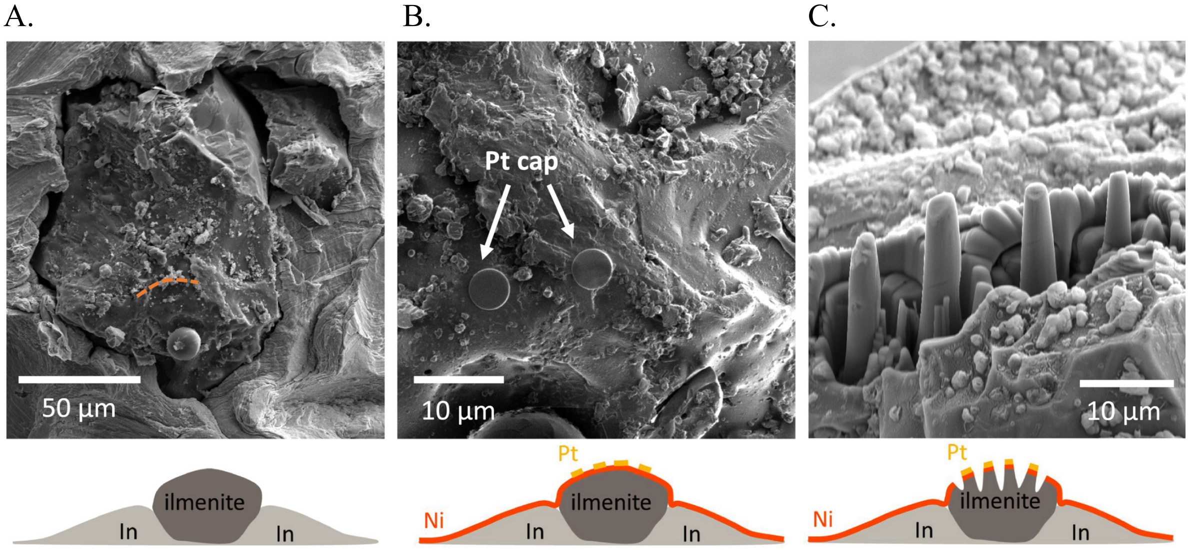

Figure 3-1: SEM images and drawings of grain and sample preparation for APT. A) Ilmenite is hand-picked and pressed into indium mounted on an SEM stub. The orange dashed line indicates the location of the grain ridge and represents a topographic high from where samples were extracted. B) The grain is ion beam sputter-coated with Ni and protective caps of Pt are deposited in the FIB with the Pt precursor gas injection system (GIS), and then (C) milled with annuli to produce spokes that will be lifted out.

sample was ion-beam-sputter coated with Ni to protect the mineral surface from Ga^+ ion irradiation during focused-ion beam (FIB)-based sample preparation (Figure 3-1B).

3.3.3 FIB Microscopy

To prepare samples for APT, we used the TESCAN LYRA3 FIB-SEM at the University of Chicago equipped with a Ga liquid-metal ion source, an Oxford Instruments OmniProbe 400 micromanipulator, and an Oxford Instruments OmniGIS gas injection system (GIS). Circular platinum caps 2 μm in diameter were deposited on top of the region of interest using ion beam–assisted deposition for 5–10 min to further protect the sample during milling (Figure 3-1B). This deposition was done with a low current (<10 pA) to minimize ion-beam implantation. The grain had no flat surfaces suitable for milling out a lamella as is done with traditional APT sample preparation (e.g., Rout et al., 2017). To reduce the milling required to produce a liftout, and to facilitate the liftout process, a topographic ridge of this grain was annularly milled with the FIB to produce several spokes 1–2 μm in diameter (Figure 3-1C), which were then lifted out using a micromanipulator. These spokes were then mounted onto flat-top Si micro tips (provided by CAMECA Instruments) by GIS Pt deposition. The spokes were shaped with the FIB following traditional APT sample preparation steps (e.g., Larson et al., 1999). The sample shaping started with a 10 kV, 35 pA beam. The sides of each sample were milled on both sides of the tip, rotated 90°, and then milled on the remaining two sides. This resulted in a truncated pyramid-shaped tip approximately 0.5 μm wide at the top. The tips were annularly milled from the top with a 10 kV, 15 pA beam to a radius of 0.2 μm, which rounds the tip out to a conical shape. At this point, any secondary tips (sharp points outside the annulus unintentionally created during sample preparation) were removed so that the primary tip stood alone for 5 μm. A low-energy mask with a 5 kV, 30 pA beam sharpened the tips to a final radius, ranging between 50 and 20 nm, and removed surface contamination. During milling, the sample was monitored with an in-beam backscatter electron detector, and the milling was stopped when the bright cap of platinum on the tip disappeared in the image. One of the nanotips (Tip D, discussed below), had surficial material removed so that deeper, unaltered material could be analyzed.

3.3.4 Atom Probe Tomography

The nanotips were analyzed with a LEAP 4000X Si atom probe tomograph at the NUCAPT facility of Northwestern University. The atom probe was run in laser mode with a UV laser (355 nm wavelength), with a pulse repetition rate of 250 kHz, a pulse energy of 35–50 pJ, and a temperature of 30 K, conditions suitable for electrically nonconductive materials. A total of four nanotips were produced for this analysis. Tip A was manually stopped at 5 M atoms. This nanotip did not yield useful data, as only coating materials were analyzed. Tip B was analyzed in two sessions. The first session analyzed coating materials, and after ~30 min of evaporation, the target material (ilmenite) was reached. The session was manually stopped, and analysis continued with only ilmenite present. Tip B fractured after 12.5 M atoms were counted. The analysis of Tip C was manually stopped at 16 M atoms, after the Fe present was no longer in nanophase form. Analysis of Tip D was manually stopped at 10 M atoms as enough atoms in the region of interest had been counted. The maximum voltage that was reached was 7 kV.

We have previously shown that APT can be used as a standardless analytical technique (Rout et al., 2017), since all elements have approximately the same detection efficiency. The samples described here were measured with the LEAP 4000X Si, with ~50% detection efficiency (e.g., Seidman and Stiller, 2009; Kelly and Lawson, 2012). A potential instrumental bias with detector dead time from C isotopes in diamond was found in previous work (Heck et al., 2014); this is caused by counting deficiencies due to highly correlated field evaporation and field evaporation of molecular ions in combination with detector dead-time limitations (Stephan et al., 2015). This combination of effects is particularly pronounced in materials that have irregular field evaporation behavior, such as diamond, or for elements with a single dominant isotope. For such samples, isotope data need to be corrected for by using a statistical method as described by Stephan et al. (2015). For most other materials with more uniform field evaporation behavior and multiple isotopes, such as the samples studied here, such a correction is very small and thus can be ignored (Rout et al., 2017).

Data were reduced using the CAMECA IVAS computer code, a commercial APT data analysis software. The elemental and molecular ion species that have been detected and identified

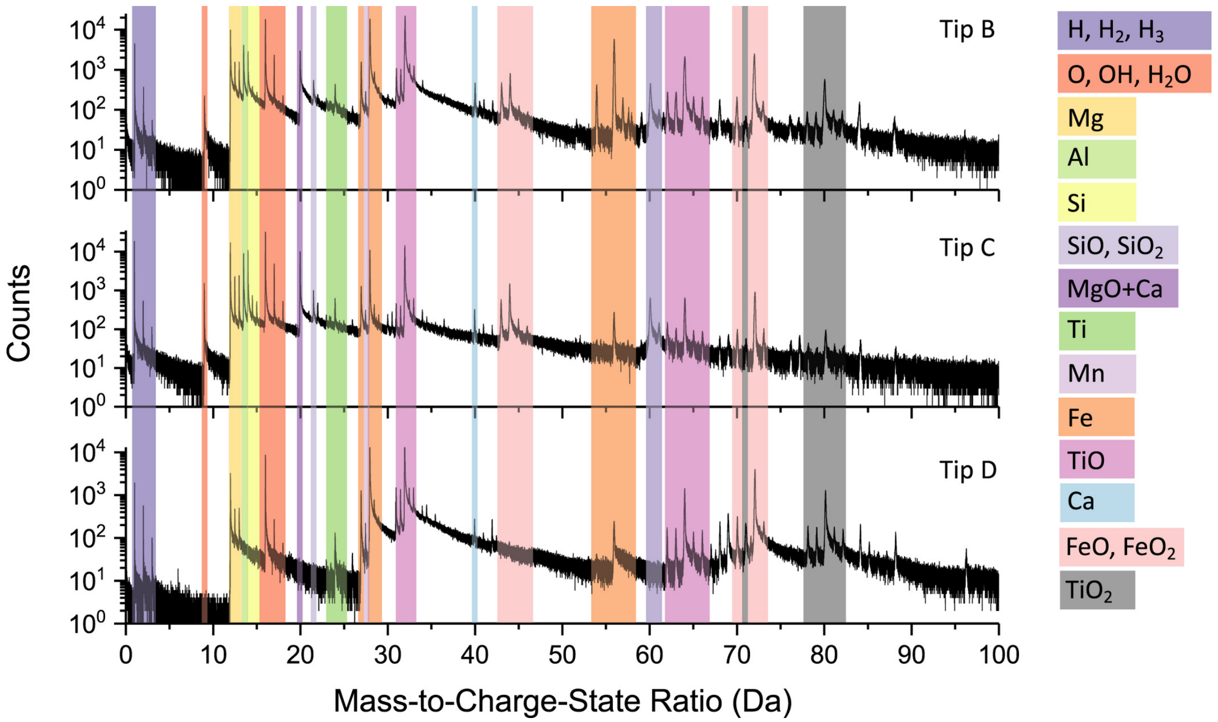

Figure 3-2: APT mass spectra of tips B, C, and D, before background correction. Identified peaks are labeled with colored stripes and can include both singly and doubly charged species.

in the mass spectrum are provided in Table 3-1, and the spectra for these samples with labeled peaks are shown in Figure 3-2. Species with peaks overlapping with isobaric interferences (listed in Table 3-1) were identified based on their natural solar system isotopic abundances. The automatic background correction from IVAS was applied to the mass spectrum. Molecular ions and both singly and doubly charged species were included in the 3-D reconstructions (Figures 3-3 and 3-4) and elemental concentrations. Nanotip geometry of the reconstruction was approximated using the half apex angle of the conical tip (also known as the shank angle) determined in SEM images. Subsets of the data were analyzed in selected spherical and cylindrical regions of interest (ROI). Concentration profiles were generated along the *z*-axis of the nanotip from binned cylindrical ROIs.

Isobaric peak overlaps prevented the identification of some rare species. Singly charged ^{20}Ne has a peak at a mass-to-charge-state ratio of 20 Da, but is obscured by the much larger $(^{40}\mathrm{Ca})^{+}$ and $(^{26}\mathrm{Mg}^{16}\mathrm{O})^{++}$ peaks at the same location in the mass spectrum (Table 3-1). The mass resolving power of the APT is generally insufficient to separate isotopic and molecular isobar peaks. For comparisons to published data, the APT data were converted from atom% to oxide wt%

Mass to Charge State Ratio	Assigned Species	Possible Interferences	Mass to Charge State Ratio	Assigned Species	Possible Interferences	Mass to Charge State Ratio	Assigned Species	Possible Interferences
1	^{1}H+		27	^{54}Fe++		58	^{58}Fe+	
2	$(^{1}H_{2})$+	^{2}H+	27.5	^{55}Mn++		60	$(^{28}Si^{16}O_{2})$+	
3	$(^{1}H_{3})$+	^{3}He+	28	^{56}Fe++		61	$(^{29}Si^{16}O_{2})$+	
9	$^{1}H_{2}{}^{16}O)$++		28.5	^{57}Fe++		62	$(^{46}Ti^{16}O)$+	$^{30}Si^{16}O_{2})$+
12	^{24}Mg++	^{12}C+	29	^{58}Fe++		63	$(^{47}Ti^{16}O)$+	
12.5	^{25}Mg++		31	$(^{46}Ti^{16}O)$++		64	$(^{48}Ti^{16}O)$+	
13	^{26}Mg++	^{13}C+	31.5	$(^{47}Ti^{16}O)$++		65	$(^{49}Ti^{16}O)$+	
13.5	^{27}Al++		32	$(^{48}Ti^{16}O)$++	^{32}S+	66	$(^{50}Ti^{16}O)$+	
16	^{16}O+		32.5	$(^{49}Ti^{16}O)$++		70	$(^{54}Fe^{16}O)$+	
17	$(^{16}O^{1}H)$+	^{17}O+	33	$(^{50}Ti^{16}O)$++		71	$(^{55}Mn^{16}O)$+	
18	$(^{1}H_{2}{}^{16}O)$+	^{18}O+	40	^{40}Ca+	^{40}Ar+, $(^{24}Mg^{16}O)$+	72	$(^{56}Fe^{16}O)$+	
20	$(^{24}Mg^{16}O)$++	^{20}Ne+	43	$(^{54}Fe^{16}O_{2})$++		73	$(^{57}Fe^{16}O)$+	
22	$(^{28}Si^{16}O)$++		44	$(^{56}Fe^{16}O_{2})$++	$(^{28}Si^{16}O)$+	74	$(^{58}Fe^{16}O)$+	
23	^{46}Ti++		44.5	$(^{57}Fe^{16}O_{2})$++	$(^{29}Si^{16}O)$+	78	$(^{46}Ti^{16}O_{2})$+	
23.5	^{47}Ti++		45	$(^{58}Fe^{16}O_{2})$++	$(^{30}Si^{16}O)$+	79	$(^{47}Ti^{16}O_{2})$+	
24	^{48}Ti++		54	^{54}Fe+		80	$(^{48}Ti^{16}O_{2})$+	
24.5	^{49}Ti++		56	^{56}Fe+		81	$(^{49}Ti^{16}O_{2})$+	
25	^{50}Ti++		57	^{57}Fe+		82	$(^{50}Ti^{16}O_{2})$+	
26	^{52}Cr++		57.5	^{115}In++				

Table 3-1: List of identified peaks and possible interferences.

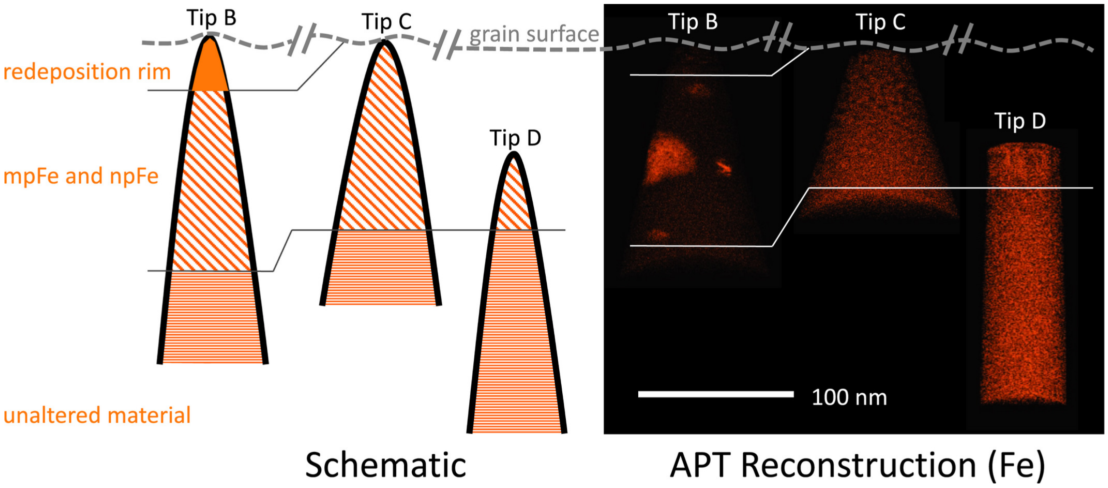

Figure 3-3: A “stratigraphic correlation-like” illustration of analyzed tips next to reconstructions of APT data (full projections), with only Fe atoms shown. The different zones are marked by thin gray lines. All three tips contain strikingly different features—the Fe atoms, represented by orange points in the right half of the figure, are distributed very differently from nanotip to nanotip. This is to be expected with Tip D, which was sampled from deeper in the grain, but Tip B and Tip C are both within approximately 10 nm of the surface. Distances are not to scale.

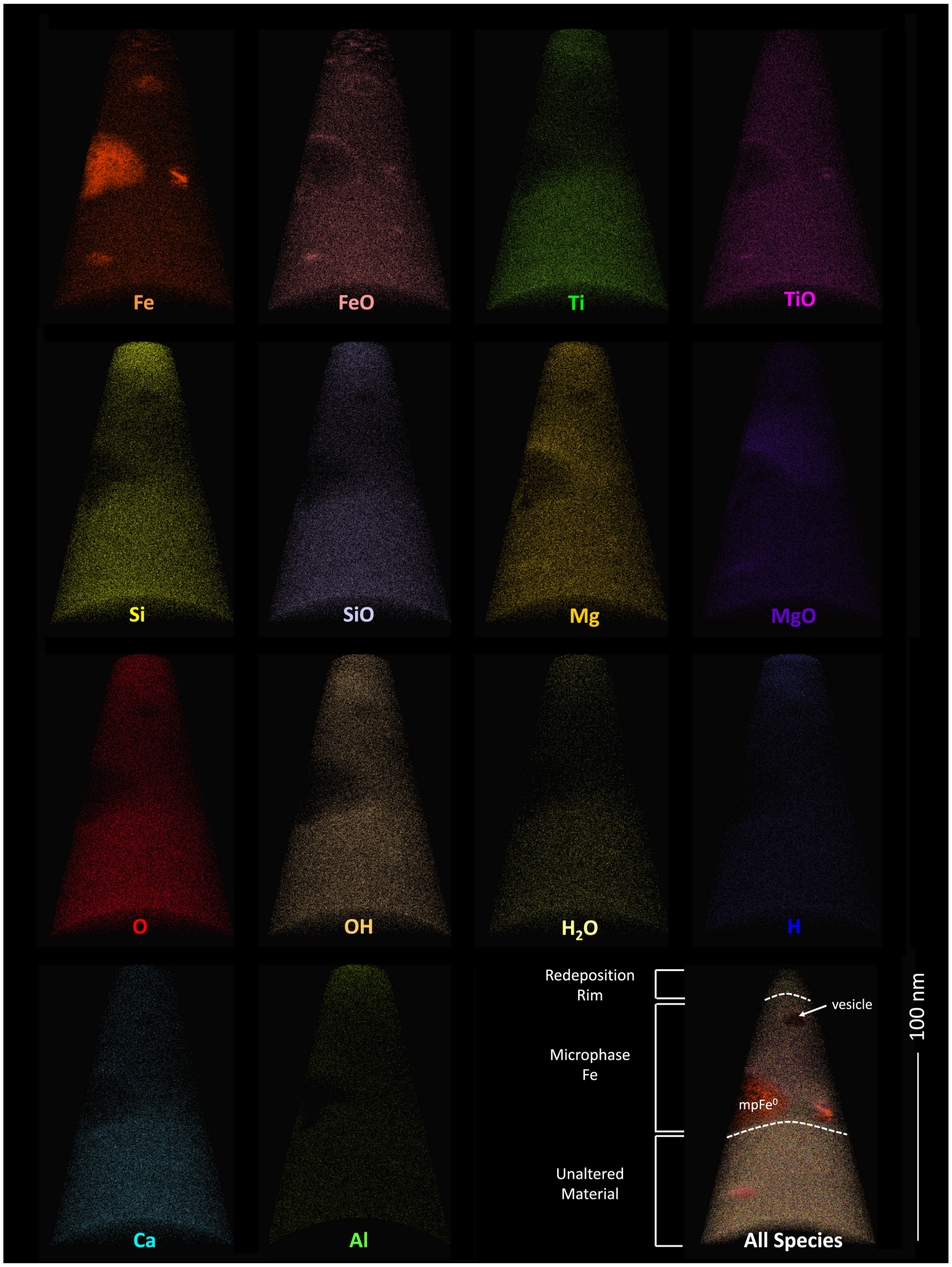

Figure 3-4: Reconstructions of Tip B in different atomic and molecular species, showing the heterogeneity of Fe when concentrated in nanophase particles, the higher concentration of species like Si and H near the top of the tip, and the absence of other species in the large, pure microphase Fe particle. The reconstruction in the lower right shows a cross section reconstruction of all identified species, exposing the vesicle. The vesicle is surrounded by an Fe-rich rim.

3.4 RESULTS

Of four nanotips that were produced from this grain, three yielded useful data—Tips B, C, and D (Figure 3-3; analysis of Tip A showed only coating materials). Tip B was extracted from the outermost surface of the grain. The suite includes the redeposition rim; nanophase and microphase Fe ranging from 5 to >30 nm in diameter; and a section near the base of the nanotip that is more homogenous in the distribution of elements, particularly Fe, than the above layers (Figure 3-3). During analysis of Tip B, the first atoms came from coating materials that were on top of this tip (not present in this reconstruction but preserved on a separate analysis that is not shown here). Tip C contains more npFe particles than Tip B, and these particles are all small, ranging from 2 to 10 nm in diameter (Figure 3-2), with no mpFe present. After these two nanotips were analyzed, Tip D was re-sharpened to expose more of the unaltered part of the grain. Although it still contains npFe in the top 40 nm, much of the nanotip has a homogenous distribution of Fe (Figure 3-2).

3.4.1 Zoning

The presence of space weathering features and differences in elemental composition allow us to distinguish three different zones with depth, similar to features described by Keller and McKay (1997), Noguchi et al. (2014), and Burgess and Stroud (2018).

3.4.1.1 Redeposition Rim

The redeposition rim was present in the reconstruction of Tip B. This rim is about 15 nm thick. Fe is heterogeneously distributed in both $(Fe)^{+,++}$ and $(FeO)^{+,++}$ as npFe particles ranging from 2 to 5 nm. Trace elements like Si, Mg, Ca, and Al are enriched in the rim (Figures 3-4 and 3-5).

3.4.1.2 Micro- and Nanophase Fe

The heterogeneity in the distribution of Fe is different in nanotips B and C. Tip C has a relatively homogenous distribution of Fe particles. These particles have a size of 2–10 nm, and as with the nanoparticles in the redeposition rim of Tip B, are correlated with $(FeO)^{+,++}$. In Tip B,

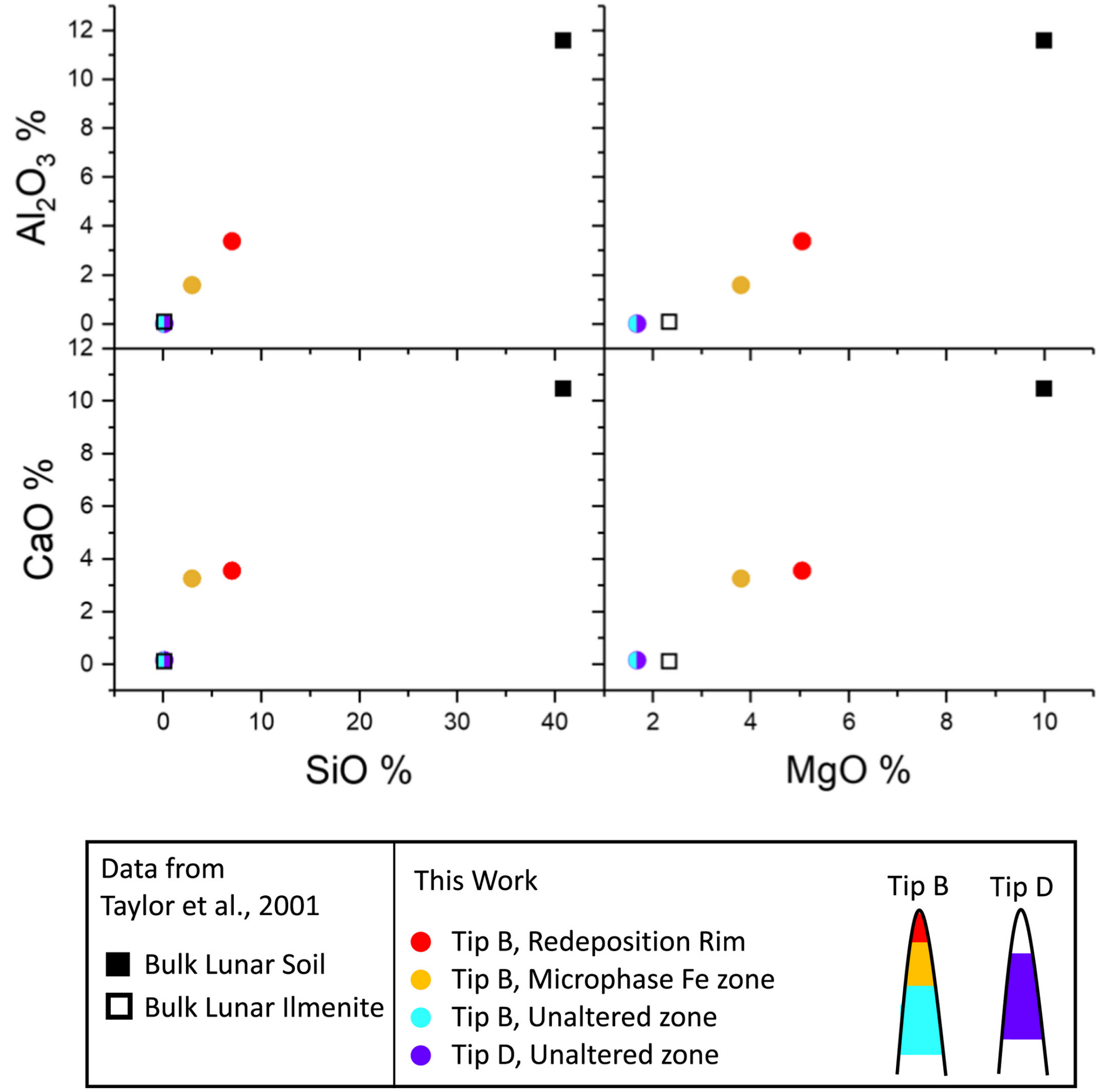

Figure 3-5: Minor and trace element compositions of selected regions within tips B and D compared to data from Taylor et al. (2001). In these diagrams, APT atomic% data were converted to oxide wt%. 1σ error bars are within the point for these data, and were not reported in Taylor et al. (2001).

there are no npFe particles below the redeposition rim. Instead, this section, approximately 110 nm thick, is dominated by a large mpFe particle, 30 nm in diameter (cutoff in the analysis, most likely >30 nm in total), and is not as enriched in Si, Mg, Ca, and Al as the redeposition rim (Figure 3-5). These particles are pure $(Fe)^{+,++}$, with $(FeO)^{+,++}$ only present within their rims. These $(FeO)^{+,++}$ rims are also slightly enriched in $(TiO)^{+}$ and $(MgO)^{+}$ relative to the rest of the sample. The entire zone is depleted in elemental Ti relative to other sections of the nanotip (Figure 3-4). This zone contains a void space approximately 20 nm in diameter.

3.4.1.3 Unaltered Material

Below the section of the nanotip containing large Fe particles in Tip B, and below the nanophase Fe particle-rich zone in Tips C and D, is material that contains no detected products of space weathering. All of the analyzed species are distributed homogenously throughout this zone, including Fe. Cr is more abundant in this zone than elsewhere (Figure 3-4).

3.4.2 Implanted Solar Wind

Tip B contains a void space, with a short axis of 8 nm and a long axis of 14 nm, which could either be a vesicle or a bubble that was formed due to implantation-generated defects (e.g., Linez et al., 2013) or escaping volatiles during the production and deposition of a melt or vapor splash. We interpret it as a vesicle similar to those described in Burgess and Stroud 2018. This is because we detect 3 ± 2 $(^{4}He)^{+}$ atoms (1σ) above background at the same depth and in close proximity to the vesicle. This $(^{4}He)^{+}$ detection seems to be due to the opening of the vesicle at the apex of the sample nanotip during analysis.

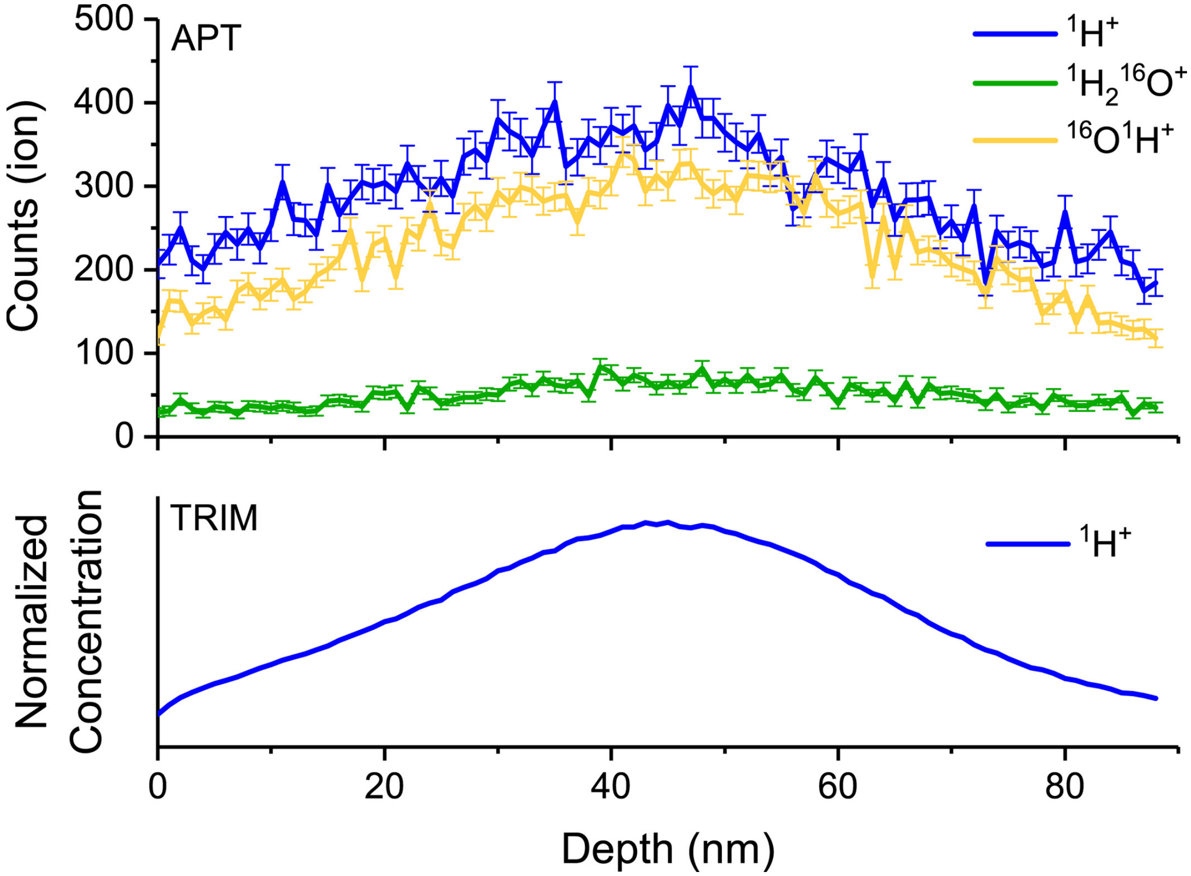

Figure 3-6: Concentration profile in Tip C of selected H-bearing species. The H-bearing species H^+ and OH^+ clearly show a concentration peak at a depth of 40–50 nm, with a shape consistent with H implantation at 4 keV into a $FeTiO_3$ glass with a density of 4.75 g cm^{-3} as simulated by SRIM/TRIM (Ziegler et al., 2012). Surface-adsorbed H usually present in large quantities on the top of the tip is not present in this reconstruction.

The solar wind ion implantation profiles are best represented by Tip C. The profile of H species present in Tip C is consistent with H implantation (Figure 3-6), not a tail-off that would be indicative of adsorbed residual H in the atom probe chamber, as in Tip B (Figure 3-7). The greatest concentration of H occurs at a depth of 40–50 nm, consistent with H^+ implantation at typical energies (Ziegler et al., 2012). H-bearing molecular ions, like OH^+ and H_2O^+, are also present (Figure 3-4); the H in these molecular ions is also sourced from the solar wind (i.e., Ichimura et al., 2012; Liu et al., 2012).

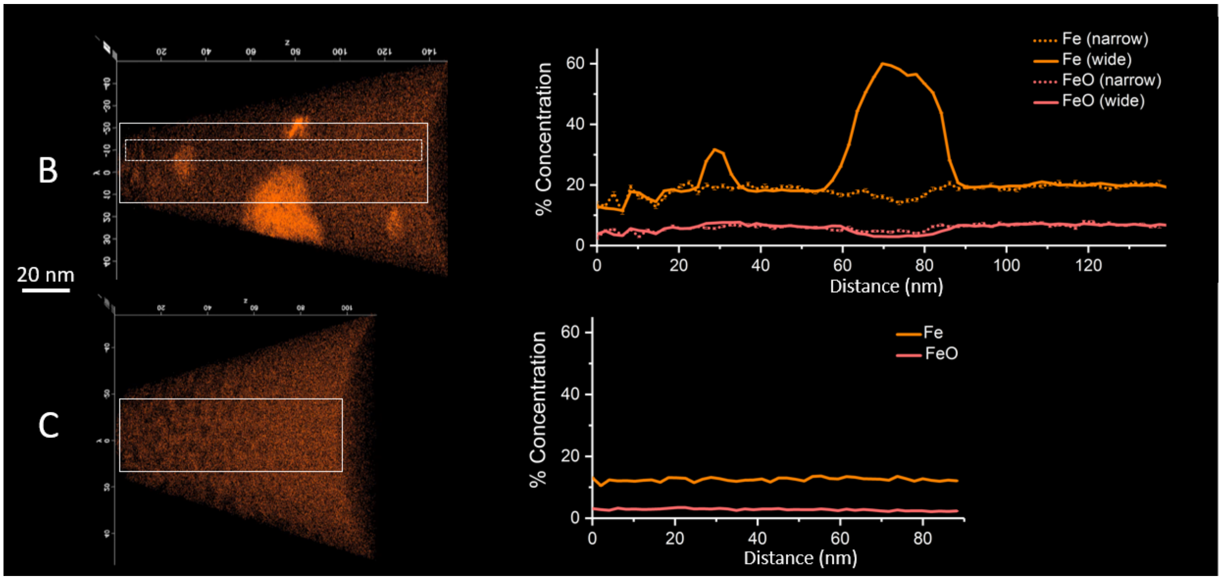

Figure 3-7: Concentration profiles of Fe and FeO in tips B and C.

No Ne was unambiguously detected in any of the nanotips nor their ROIs. The peak at mass-to-charge (m/z) state 20 corresponds to $(Ca)^{++}$, the molecular ion $(MgO)^{2+}$, as well as $^{20}Ne^{+}$, and these isobaric overlaps overwhelm any signal from $^{20}Ne^{+}$ that could be present. The $m/z = 20$ peak correlates with $(TiO)^{+}$, $(TiO)^{2+}$, and $(FeO)^{+}$ peaks, and therefore, the signal is likely to be dominated by Ca and MgO, not Ne. $(MgO)^{2+}$ is distributed heterogeneously throughout the nanotip, correlating to npFe and the microphase Fe particles. If the $m/z = 20$ species was mostly $^{20}Ne^{+}$, it would be expected to occur at discrete locations such as within the vesicle and within other defects, similar to the solar wind He (Burgess and Stroud, 2018). The species at a mass-to-charge-state ratio 40 does not correlate with $(MgO)^{2+}$ and is interpreted as $^{40}Ca^{+}$. The species at 22 is interpreted as $(Si^{28}O^{16})^{2+}$, and since the Si enrichment is in the outermost section of the nanotip (the same region we would expect Ne enrichment), and is much more abundant than Ne, ^{22}Ne could not be identified in the integrated data set of each nanotip. Any heavier noble gases were below our detection limit.

3.5 DISCUSSION

3.5.1 Comparison of Different Sample Tips

Lateral variability in products of micrometeorite impact melting on the nanometer and centimeter scale has been seen on lunar samples (Christoffersen et al., 1996; Noble et al., 2013). The characteristics of the sample nanotips vary greatly (Figure 3-3), though they were all extracted from a small surface area with dimensions of 5 × 25 µm on the same grain. Tips B and C were prepared using the same method. While none of the capping materials were measured on Tip C, the top of the nanotip is no more than 10 nm below the surface of the grain, as determined from careful monitoring of the nanotip during milling. Although this may be enough to remove a thin redeposition rim, the distribution of Fe between the different nanotips is still very different. Tip D was milled to expose a deeper part of the grain and, since most of the nanotip does not have npFe, is a more representative sample of unweathered grain material. The different distribution of space weathering products between B and C is due to the sample nanotip's original position in the grain, as the nanotips come from different locations on the grain's ridge, and therefore could have been exposed to different events. These results show the heterogeneous nature of space weathering on different regions of identical composition on even a single grain.

Two elemental concentration profiles, comprising a cylinder the length of the sample, were generated for Tip B. One of the Fe concentration profiles was generated to include most of the nanotip material, including the mpFe particle. There is a significant spike in Fe between 60 and 80 nm from a concentration of about 20 atom% to a maximum of 60 atom% (Figure 3-7). A profile in the same nanotip that does not include as much material but avoids all of the large particles shows a slight decrease in Fe concentration at the same depth as the largest particle. This suggests that the Fe in the particle is intrinsic to the samples, as Fe is depleted in the region immediately surrounding the microphase particle. In Tip C, which has no large mpFe particles, the concentration of Fe remains constant with depth. Tips B, C, and D were extracted from locations on the grain that were less than 25 μm apart, which illustrates the heterogeneity on the micro- as well as nanoscale.

3.5.2 Comparison with Other Space-Weathered Samples

Here, we analyze our samples within the framework that was developed by Noguchi et al. (2014). These authors defined three zones (I–III) that described the different types of space weathering modification found in grains from the asteroid Itokawa. The zones we observe in the lunar material have the same compositional characteristics as the Noguchi et al. (2014) zones but have different depth ranges. By using these zones, lunar and asteroidal space weathering effects can be directly compared, even for large differences in the duration of space exposure.

Zone I, composed of products from redeposition, is present on Tip B. However, in Itokawa particles, the redeposition rim is thinner (~5 nm) than that of our sample (~20 nm). The regolith of Itokawa is thought to be younger than the lunar regolith sampled by Apollo 17 as asteroidal regoliths have a shorter lifetime, due to the lower gravity compared to the Moon (Miyamoto et al., 2006; Nagao et al., 2011). Previous TEM studies of lunar ilmenite also show that this topmost layer (1) is Si-rich and ranges from 10 to 50 nm thick and (2) has a high concentration of npFe and vapor-deposited species like Ca, Al, Mg, and S (Christoffersen et al., 1996; Noble et al., 2006; Zhang and Keller, 2010).

Zone II, dubbed the partially amorphized zone in Noguchi et al. (2014), corresponds to the area of Tip B that is dominated by the microphase Fe particle (see Figure 3-5, yellow zone). The thickness of the npFe-bearing rim in Tip C is about 60 nm, which is comparable to the nanocrystalline and disordered rim described on lunar ilmenites (Christoffersen et al., 1996; Burgess and Stroud, 2018) and only 10–20 nm thicker than that of Itokawa olivine grains (Noguchi et al., 2011). The npFe particles are 2–5 nm in diameter, larger than those typically seen in Itokawa grains (Noguchi et al., 2014). The npFe particles in this zone range in size from 2 to >30 nm (2–5 nm in Tip C and 2–30 nm in Tip B) and this is similar to the range (10–50 nm) seen within the disordered rim of the ilmenite studied by Burgess and Stroud (2018) and Zhang and Keller (2010). We do not see nanophase sulfides. There is an isobaric overlap between $^{32}S^{+}$ and $(TiO)^{2+}$ (Table 3-1), but the species at *m/z* = 32 does not correlate with the nanophase particles and is therefore dominated by $(TiO)^{2+}$. We also do not see any TiO_2 precipitates within this region as seen by Christoffersen et al. (1996) and Burgess and Stroud (2018). While asteroids and the Moon do not experience the same space weathering environments, this shows that the process responsible for producing the npFe must be active on asteroids as well as the Moon, or that different processes result in the same behavior in different materials.

Elemental compositions of Zones I and II in our samples (Figure 3-5) fall between the two endmember compositions of bulk lunar soil and bulk lunar ilmenite (Taylor et al., 2001). The latter corresponds to the unaltered zones (see text below).

Zone III, the unaltered or crystalline zone, is present in both the base of Tips B and C, and most of Tip D (see Figure 3-5, green and purple zones). This area is homogenous and has a minor and trace element composition almost identical to bulk lunar ilmenite (Figure 3-5; Taylor et al., 2001). The MgO, CaO, and Al_2O_3 compositions of this zone in Tips B and D are nearly identical (MgO = 1.68 ± 0.55% for both nanotips, CaO = 0.15 ± 0.19% for both, and Al_2O_3 = 0.02 ± 0.13% for Tip B and 0.01 ± 0.06% for Tip D).

Although the Noguchi et al. (2014) zone classification can be applied well to Tip B, this classification does not necessarily accurately describe the other nanotips studied here or other lunar samples, which may have other products that were not seen in our samples (Keller and McKay, 1997). Zone II is similar to the outer rim described by Burgess and Stroud (2018), which has 10–50 nm Fe particles in a disordered matrix. The Itokawa samples do not contain the larger mpFe particles observed here, which are located in the section of Tip B that corresponds to Zone II. However, Tip B contains a vesicle with a size that is more comparable to the Itokawa grains (20–50 nm) than those found in other lunar regolith soil grains (100–200 nm; Noguchi et al., 2014). Previous TEM studies show that the npFe is sometimes elongated parallel to the surface of the host ilmenite grain, which is the orientation we see in our samples (Zhang and Keller, 2010).

3.5.3 Redeposition Rim Mixing

An advantage of APT is its high spatial resolution, which allows for compositional analysis of small volumes not resolvable with other techniques. When converted to oxide wt%, some of the minor elements plot on a mixing line (Figure 3-5) between the bulk lunar ilmenite and the bulk lunar soil as measured by Taylor et al. (2001). Generally, the unaltered material (Noguchi Zone III) is identical within error to bulk lunar ilmenite. In some cases, the unaltered material has smaller concentrations of these minor and trace elements, as the bulk ilmenite measurements may have included the space-weathered rim and are thus more enriched in elements like Mg and Al. The redeposition rim is distinguished from the rest of the nanotip by its different composition (Figure 3-4). The redeposition rim is more enriched in the minor elements than the nanophase Fe area, suggesting that some of the rim material is sourced from outside of the ilmenite grain and is a true redeposition rim, and the different composition is not due to just the preferential removal of Fe and O. We are unable to determine if this microstructure was altered by irradiation.

Previous TEM studies of ilmenite grains (Bernatowicz et al., 1994; Christoffersen et al., 1996; Noble et al., 2006; Zhang and Keller, 2010; Burgess and Stroud, 2018) from the lunar soil also show the presence of a redeposition rim on the grain surfaces that is enriched in Mg, Al, Si, and Ca. Since most of these elements are not present, or only present in minor amounts in ilmenite, this leads to the conclusion that they were formed by condensation of vapor produced by the impact of micrometeorites on adjacent (non-ilmenite) grains and by deposition of materials sputtered by energetic solar wind ions from the nearby grains. Although several studies have suggested that micrometeorite impacts are the dominant contributor to the deposition rims, Bernatowicz et al. (1994) suggested that solar wind radiation damage could also contribute to their formation.

3.5.4 Hydrogen and Noble Gases

Hydrogen is more abundant than He and Ne in the solar wind by factors of about 25 and 17,000 times, respectively (Wieler, 2002). We do not see these expected ratios in our samples. In Tip C, where the H profile is indicative of solar wind implantation, the concentration (from the "unaltered" volume used for Figure 3-6; purple) is 6.2×10^{20} H atoms cm^{-3}, and the fluence (irradiation over a surface area) is 6.9×10^{18} H atoms cm^{-2} (including atoms from H hydride compounds observed in the mass spectrum). In Tip B, the hotspot of ^{4}He, which shows three ^{4}He atoms above background (3 ± 2 ^{4}He atoms above background [1σ]), is observed in a location near the edge of the vesicle, which suggests that these atoms were evaporated when the vesicle was first opened during sample preparation with the FIB or field evaporation with APT.

We can attempt to estimate the expected ^{4}He amount present in our nanotips by (1) normalizing the noble gas concentration measured in other ilmenite grains from sample 71015 to the nanotip's volume and (2) dividing the measured H concentration in the tip by the H/He ratio in the solar wind (Wieler, 2002). With the first method, we estimate the number of ^{4}He atoms present in the volume of Tip B (3.7×10^{-16} cm^3) based on the ^{4}He concentrations measured in ilmenite separates from sample 71501 by Benkert et al. (1993). This is a very conservative estimate assuming that the entirety of the grains analyzed by Benkert et al. (1993) has the same solar wind He concentration as the nanotip representing mostly the outermost (solar wind–bearing) region of a grain. An expected count brings the estimate to ~4800 ^{4}He atoms in the entirety of Tip B. The measured ^{4}He concentration of the entirety of Tip B, 3 atoms, is only ~0.5‰ of the expected concentration of ^{4}He. In the second method, the surface-adsorbed H dominates the signal in Tip B, so we use the bulk H concentration of Tip C to estimate the expected amounts in Tip B. Assuming the ^{4}He concentration is homogeneous throughout the entire nanotip, we obtain an estimate of ~7800 ^{4}He atoms in the entirety of Tip B. This is within a factor of 1.6 of the estimate based on the first method. If there was no ^{4}He migration into the vesicle, ~20–30 ^{4}He atoms would be expected in a volume the size of the vesicle in Tip B (2.5×10^{-18} cm^3). However, given that the solar wind He was likely concentrated in the vesicle, it is possible that all of the ^{4}He from this nanotip was lost upon opening (either during sample preparation or analysis) before it could be analyzed.

We did not detect any Ne, although both the lower limits for ^{20}Ne and ^{22}Ne concentrations based on single grain analyses from Benkert et al. (1993) were above our detection limit in the spectrum of the vesicle (Figure 3-8). Using the H/Ne ratio from Wieler (2002), ~11 ^{20}Ne atoms are expected to be present in Tip B. Other species, like ^{3}He and ^{21}Ne, are not detectable above background in such an analysis, but are detectable if concentrated in a small volume, such as a vesicle. Even though there is an isobaric overlap between ^{20}Ne, ^{40}Ca^{++}, and (^{24}Mg^{16}O)$^{++}$, an increased concentration of a species with a mass-to-charge state of 20 that correlates with either other noble gases or a vesicle is likely to be ^{20}Ne, as Mg is present in the 1–7 wt% level but is only in the sample material, not the void space. ^{36}Ar is present in too low abundances to be expected to be present in a sample nanotip of this volume.

Burgess and Stroud (2018) showed that the He present in the grain rims is concentrated in these vesicles and in planar defects, and vesicles develop due the interaction between the soil particle and the solar wind. There could be several explanations or a combination thereof for a lower-than-expected concentration of He and the non-detection of Ne, including (1) the electric field was not high enough to quantitatively ionize He and Ne, which escaped to vacuum as neutrals; (2) after the vesicle was opened during APT analysis, most of the He and Ne escaped without

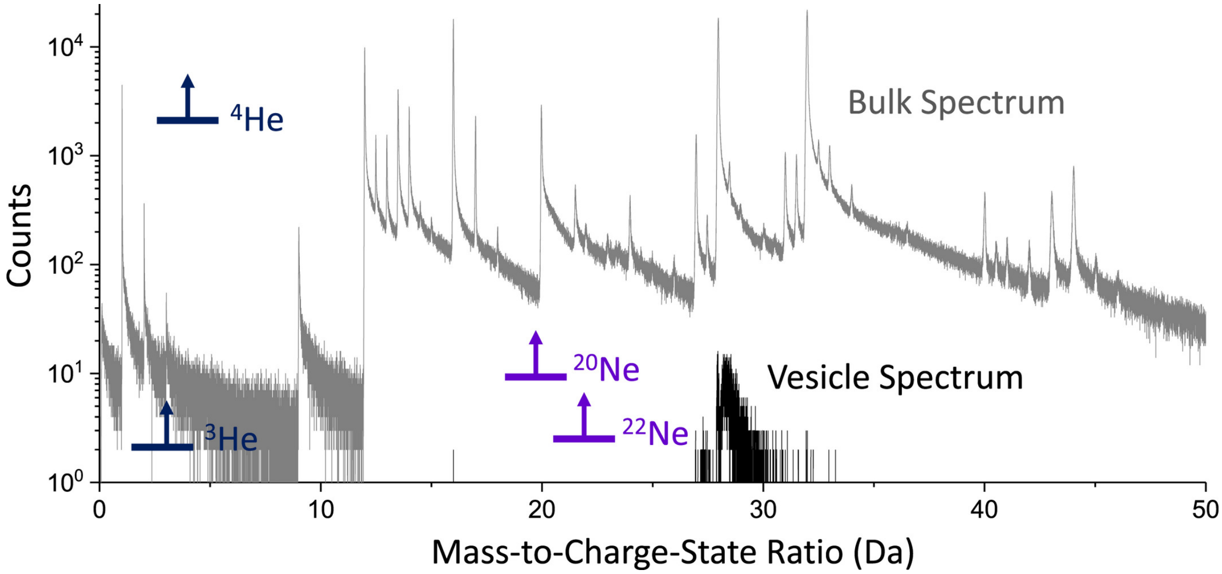

Figure 3-8: The gray spectrum shows the integrated composition of Tip B. The black spectrum shows the composition of a spherical ROI centered on the void space in Tip B. Some of the signal comes from the material immediately surrounding the vesicle, which was included due to the oblate nature of the vesicle. Lower limits on noble gas concentration for He and Ne based on bulk data (calculated as describe the main text) are shown.

having been ionized; (3) the sample was clipped during FIB milling for sample preparation and the majority of the gas escaped at this time. Although He in this form is a difficult element to measure with APT, due to the difficulty in controlling field evaporation and field ionization of gaseous He in a vesicle, there have been multiple studies that have detected He in metals (e.g., Wagner and Seidman, 1979; Seidman et al., 1980; Edmondson et al., 2013), and this remains an open area of study for cosmochemical materials.

3.6 SUMMARY AND CONCLUSIONS

We successfully used APT to characterize space weathering products in lunar ilmenite.

- In our samples, we see a redeposition rim, iron clusters (both a microphase Fe particle and nanophase Fe particles), and a vesicle that likely once held solar wind.
- We observe compositional heterogeneity in ilmenite at the nanoscale, the micron scale, and on different surfaces of the same grain. This implies small-scale intragrain variability of exposure to space weathering.
- In Tip C, H-bearing species are present in the greatest amounts at a depth range of 40–50 nm, fully consistent with solar wind implantation.
- In a vesicle at 30 nm depth below the surface 3 ± 2 ^{4}He atoms were detected. While this is significantly below the concentration expected (only 0.1% of the expected value), this is likely due to the difficulty of quantitatively ionizing He before it is lost to the sample chamber.
- We have shown that APT can be successfully used for targeted cosmochemical, tomographic analyses of space-weathered samples while keeping total sample consumption very low.

We conclude that APT is an ideal analytical method to study surface effects of precious samples, such as mission-returned samples like those presented here.

3.7 REFERENCES

Benkert, J., H. Baur, P. Signer, and R. Wieler. "He, Ne, and Ar from the solar wind and solar energetic particles in lunar ilmenites and pyroxenes." *Journal of Geophysical Research: Planets* 98, no. E7 (1993): 13147-13162.

Bernatowicz T. J., R. H. Nichols Jr., and C. M. Hohenberg. “Origin of amorphous rims on lunar soil grains.” *25th Lunar and Planetary Science Conference*. (1994): 105– 106.

Blum, T. B., J. R. Darling, T. F. Kelly, D. J. Larson, D. E. Moser, A. Perez-Huerta, T. J. Prosa, S. M. Reddy, D. A. Reinhard, D. W. Saxey, R. M. Ulfig, and J. W. Valley. "Best practices for reporting atom probe analysis of geological materials." *Microstructural geochronology: Planetary records down to atom scale.* Edited by D. E. Moser, F. Corfu, J. R. Darling, S. M. Reddy, and K. Tait. (2018): 369-373.

Burgess, K. D., and R. M. Stroud. "Phase-dependent space weathering effects and spectroscopic identification of retained helium in a lunar soil grain." *Geochimica et Cosmochimica Acta* 224 (2018): 64-79.

Christoffersen R., D. S. McKay, and L. P. Keller. “Microstructure, chemistry, and origin of grain rims on ilmenite from the lunar soil finest fraction.” *Meteoritics & Planetary Science* 31 (1996): 835– 848.

Daly L., P. A. Bland, D. W. Saxey, S. M. Reddy, D. Fougerouse, W. D. A. Rickard, and L. V. Forman. “Nebula sulfidation and evidence for migration of free floating refractory metal nuggets revealed by atom probe microscopy.” *Geology* 45 (2017): 847– 850.

Deer W. A., R. A. Howie, and J. Zussman. “An introduction to rock forming minerals, 2nd ed.” Harlow, UK: Longman Scientific & Technical (1992).

Edmondson P. D., C. M. Parish, Y. Zhang, A. Hallén, and M. K. Miller. “Helium distributions in a nanostructured ferritic alloy.” *Journal of Nuclear Materials* 434 (2013): 210– 216.

Frick U., R. H. Becker, and R. O. Pepin. “Solar wind record in the lunar regolith—Nitrogen and noble gases.” *Proceedings, 18th Lunar and Planetary Science Conference* (1988): 87– 120.

Heber V. S., K. D. McKeegan, D. S. Burnett, J. Duprat, Y. Guan, A. J. G. Jurewicz, C. T. Olinder, and S. P. Smith. “Accurate analysis of shallowly implanted solar wind ions by SIMS backside depth profiling.” *Chemical Geology* 390 (2014): 61– 73.

Heck P. R., F. J. Stadermann, D. Isheim, O. Auciello, T. L. Daulton, A. M. Davis, and J. W. Elam. “Atom-probe analyses of nanodiamonds from Allende.” *Meteoritics & Planetary Science* 49 (2014): 453– 467.

Heiken G. and D. S. McKay. “Petrography of Apollo 17 soils.” *Proceedings, 5th Lunar Conference*. (1974): 843– 860.

Hintenberger H., H. W. Weber, and L. Schultz. "Solar, spallogenic, and radiogenic rare gases in Apollo 17 soils, and breccias." *Proceedings, 5th Lunar Science Conference* (1974): 2005– 2022.

Ichimura A. S., A. P. Zent, R. C. Quinn, M. R. Sanchez, and L. A. Taylor. "Hydroxyl (OH) production on airless bodies: evidence from H^+/D^+ ion-beam experiments." *Earth and Planetary Science Letters* 345–348 (2012): 90– 94.

Keller L. P. and D. S. McKay. "The nature and origin of rims on lunar soil grains." *Geochimica et Cosmochimica Acta* 61 (1997): 2311– 2341.

Kelly T. F. and D. J. Lawson. "Atom probe tomography." *Annual Review of Materials Research* 42 (2012): 1– 31.

Larson D. J., D. T. Foord, A. K. Petford-Long, H. Liew, M. G. Blamire, A. Cerezo, and G. D. W. Smith. "Field-ion specimen preparation using focused ion-beam milling." *Ultramicroscopy* 79 (1999): 287– 293.

Lewis J. B., D. Isheim, C. Floss, and D. N. Seidman. "$^{12}C/^{13}C$-ratio determination in nanodiamonds by atom-probe tomography." *Ultramicroscopy* 159 (2015): 248– 254.

Linez F., E. Gilabert, A. Debelle, P. Desgardin, and M.-F. Barthe. "Helium interaction with vacancy-type defects created in silicon carbide single crystal." *Journal of Nuclear Materials* 436 (2013): 150– 157.

Liu Y., Y. Guan, Y. Zhang, G. R. Rossman, J. M. Eiler, and L. A. Taylor. "Direct measurement of hydroxyl in the lunar regolith, and the origin of lunar surface water." *Geoscience Nature* 5 (2012): 779– 782.

McKay D. S. and R. J. Williams. "A geologic assessment of potential lunar ores. In Space resources and space settlements." Edited by J. Billingham, W. Gilbreath, and B. O'Leary Washington, D.C.: NASA ARC. (1979): 243– 255.

McKay D. S., G. Heiken, A. Basu, G. Blanford, S. Simon, R. Reedy, B. M. French, and J. Papike. "The lunar regolith." Lunar Sourcebook, edited by G. H. Heinken, D. T. Vaniman, and B. M. French Cambridge, UK: Cambridge University Press. (1991): 285– 356.

Miyamoto H., H. Yano, D. Scheeres, S. Sasaki, O. Barnouin-Jha, R. W. Gaskell, A. Cheng, H. Demura, A. Fujiwara, T. Hashimoto, N. Hirata, C. Honda, M. Ishiguro, T. Kubota, T. Michikami, A. M. Nakamura, R. Nakamura, J. Saito, Y. Yokota, and the Hayabusa Team. "Regolith on a tiny asteroid: Granular materials partly cover the surface of Itokawa". *Lunar and Planetary Science 37* (2006).

Nagao K., R. Okazaki, T. Nakamura, Y. N. Miura, T. Osawa, K. Bajo, S. Matsuda, M. Ebihara, T. R. Ireland, F. Kitajima, H. Naraoka, T. Noguchi, A. Tsuchiyama, H. Yurimoto, M. E. Zolensky, M. Uesugi, K. Shirai, M. Abe, T. Yada, Y. Ishibashi, A. Fujimura, T. Mukai, M. Ueno, T. Okada,

M. Yoshikawa, and J. Kawaguchi. “Irradiation history of Itokawa regolith material deduced from noble gases in the Hayabusa samples.” *Science* 33 (2011): 1128– 1131.

Noble S. K., L. P. Keller, and R. Christoffersen. “Chemical mapping nanometer-scale of weathered lunar space soil: New view A”. *Lunar and Planetary Science* (2006): 37.

Noble S. K., L.P. Keller, R. Christoffersen, and Z. Rahman. “Variations lateral in patina lunar weathering on centimeter to nanometer scales.” *Lunar and Planetary Science* (2013): 44.

Noguchi T., T. Nakamura, M. Kimura, M. E. Zolensky, M. Tanaka, T. Hashimoto, M. Konno, A. Nakato, T. Ogami, A. Fujimura, M. Abe, T. Yada, T. Mukai, M. Ueno, T. Okada, K. Shirai, Y. Ishibashi, and R. Okazaki. “Incipient space weathering observed on the surface of Itokawa dust particles.” *Science* 333 (2011): 1121– 1125.

Noguchi T., M. Kimura, T. Hashimoto, M. Konno, T. Nakamura, M. E. Zolensky, R. Okazaki, M. Tanaka, A. Tsuchiyama, A. Nakato, T. Ogami, H. Ishida, R. Sagae, S. Tsujimoto, T. Matsumoto, J. Matsuno, A. Fujimura, M. Abe, T. Yada, T. Mukai, M. Ueno, T. Okada, K. Shirai, and Y. Ishibashi. “Space weathered rims found on the surfaces of the Itokawa dust particles.” *Meteoritics & Planetary Science* 49 (2014): 188– 214.

O'Neill G. K., J. Billingham, W. Gilbreath, B. O'Leary, and B. Gossett. “Space resources and space settlements.” SP-NASA428. (1977).

Papike J., L. Taylor, and S. Simon. “Lunar minerals.” *Lunar Sourcebook*, edited by G. H. Heinken, D. T. Vaniman and B. M. French Cambridge, UK: Cambridge University Press. (1991): 121– 181.

Parman S. W., D. R. Diercks, B. P. Gorman, and R. F. Cooper. “Atom probe tomography of isoferroplatinum.” *American Mineralogist* 100 (2015): 852– 860.

Peterman E. M., S. M. Reddy, D. W. Saxey, D. R. Snoeyenbos, W. D. A. Rickard, D. Fougerouse, and A. R. C. Kylander-Clark. “Nanogeochronology of discordant zircon measured by atom probe microscopy of Pb-enriched dislocation loops.” *Science Advances* 2 (2016): https://doi.org/10.1126/sciadv.1601318

Reisenfeld D. B., R. C. Wiens, B. L. Barraclough, J. T. Steinberg, M. Neugebauer, J. Raines, and T. H. Zurbuchen. “Solar wind conditions and composition during the genesis mission as measured by in situ spacecraft.” *Space Science Reviews* 175 (2013): 125– 164.

Rout S. S., P. R. Heck, D. Isheim, T. Stephan, N. J. Zaluzec, D. J. Miller, A. M. Davis, and D. N. Seidman. “Atom-probe tomography and transmission electron microscopy of the kamacite–taenite interface in the fast-cooled Bristol IVA iron meteorite.” *Meteoritics & Planetary Science* 52 (2017): 2707– 2729.

Seidman D. N. and K. Stiller. “An atom-probe tomography primer.” *MRS Bulletin* 34 (2009): 717– 724.

Seidman D. N., J. Amano, and A. Wagner. “The study of defects, radiation damage and implanted gases in solids by field ion and atom-probe microscopies.” Ithaca, New York: The Materials Science Center. (1980).

Signer P., H. Baur, U. Derksen, P. Etique, H. Funk, P. Horn, and R. Wieler. “Helium, neon, and argon records of lunar soil evolution.” *Proceedings, 8th Lunar Science Conference* (1977): 3657–3683.

Stephan T., P. R. Heck, D. Isheim, and J. B. Lewis. “Correction of dead time effects in laser-induced desorption time-of-flight mass spectrometry: Applications in atom probe tomography.” *International Journal of Mass Spectrometry* 379 (2015): 46– 51.

Taylor L. A., C. M. Pieters, L. P. Keller, R. V. Morris, D. S. McKay, A, Patchen, and S. Wentworth. “The effects of space weathering on Apollo 17 mare soils: petrographic and chemical characterization.” *Meteoritics & Planetary Science* 36 (2001): 285– 299.

Valley J. W., A. J. Cavosie, T. Ushikubo, D. A. Reinhard, D. F. Lawrence, D. J. Larson, and P. H. Clifton. “Hadean age for a post-magma-ocean zircon confirmed by atom-probe tomography.” *Nature Geoscience* 7 (2014): 219– 223.

Valley J. W., D. A. Reinhard, A. J. Cavosie, T. Ushikubo, D. F. Lawrence, D. J. Larson, T. F. Kelly, D. R. Snoeyenbos, and A. Strickland. “Nano- and micro-geochronology in Hadean and Archean zircons by atom-probe tomography and SIMS: New tools for old minerals.” *American Mineralogist* 1 (2015): 34– 42.

Wagner A. and D. N. Seidman. “The range profiles of 300 and 475 eV ^{4}He+ ions and diffusivity of ^{4}He in tungsten.” *Physical Review Letters* 42 (1979): 515– 518.

Wieler R. “Noble gases in the solar system.” *Reviews in Mineralogy and Geochemistry* 47 (2002): 21– 70.

Wieler R., K. Kehm, A. P. Meshik, and C. M. Hohenberg. "Secular changes in the Xenon and Krypton abundances in the solar wind recorded in single lunar grains.” *Nature* 384 (1996): 46– 49.

Zhang S. and L. P. Keller. “Formation of ilmenite rims in lunar soils: Deposition vapor, irradiation, and thermal effects.” *Lunar and Planetary Science* 41 (2010).

Ziegler J. F., J.P. Biersack, and M. D. Ziegler. “SRIM: The stopping and range of ions in matter.” Morrisville, North Carolina: *Lulu Press Co* (2012) http://www.srim.org.

CHAPTER FOUR: CHARACTERIZING NANOSCALE SPACE WEATHERING FEATURES OF MATURE LUNAR SOILS USING CORRELATED APT AND TEM ANALYSES

4.1 ABSTRACT

Space weathering is the alteration of the outer surfaces of grains on airless bodies when irradiated by cosmic rays, the solar wind, electromagnetic radiation, and impacts from micrometeorites (Pieters and Noble, 2016). While the various space weathering products have been described, more nanoscale compositional studies of the diversity of materials that experienced different degrees of space weathering are needed to characterize their range of space weathering products due to the materials' different susceptibilities to space exposure. Vesicles are one of the features that can form when a mineral grain is exposed to the space weathering environment, and it has been suggested that the solar wind is particularly important in the development of these features, implanting H and He ions that concentrate in defects that can develop into vesicles (e.g., Bradley et al., 2014; Burgess and Stroud 2018; Thompson et al., 2016). In this case, materials that are closer to the Sun should have more developed vesicle features, and characterizing samples that are exposed at 1 AU (i.e. the Moon) is necessary to put other samples that were exposed further away from the Sun (e.g., the moons of Mars and main belt asteroids) in proper context. However, because of the multiple processes that contribute to the weathering of a sample simultaneously, it can be difficult to determine the relative importance of each. In order to successfully disentangle this (through methods such as simulating space weathering; i.e. Laczniak et al., 2021), the natural products of space weathering need to be fully characterized. Here we present atom probe tomographic analyses of mature lunar soil 79221 to investigate the difference

in nanoscale space weathering products to submature soil 71501 (chapter 3), with a specific emphasis on vesicles.

4.2 INTRODUCTION

Space weathered surfaces can be seen at the microscale in “bubbly” surface textures, but many products can only be characterized at the nanoscale. Atom probe tomography (APT) is a technique that field-evaporates atoms from a sample nanotip and uses time-of-flight and a position-sensitive detector to recreate the sample in 3D and is an ideal method to investigate the outermost ~100s of nanometers of the surfaces of space weathered samples (e.g., Greer et al., 2020; Daly et al, 2021). Samples exposed for a long time to space weathering are termed mature (a qualitative classification, see chapter 1) and contain a higher density of vesicles (Keller et al., 1999). In sampling at the nanoscale level, we see a heterogeneity in the products of space weathering that spans the entire range of soil maturity classification among different minerals even from the same soil sample. Thus, while soil maturity is a useful classification for soils in bulk, it fails to capture the wide range of features that are seen in the surfaces of these grains at the nanoscale. Apollo 17 sample Soil 79221 is classified as mature and has previously been used to study space weathering on the Moon (Keller et al., 1999, Taylor et al., 2001, Thompson, 2016). An object’s average heliocentric distance is an important factor on how space weathering features will develop, but even on the Moon a range of soil maturities are present due to different shielding histories and susceptibilities to space weathering. It is therefore important to explore the range of alteration the lunar regolith has experienced. In this work, we also explore how initial composition affects space weathering of different soil materials.

4.3 METHODS

To obtain individual soil grains for analysis the soil sample was sieved to > 45 µm, and this size fraction was transferred to C tape on an SEM stub. The mount was analyzed using EDS at Purdue University with a Hitachi TM 4000 Plus benchtop SEM, and grains in the 100-200 µm range with surface features such as vesicles or bubbles were targeted. Using a FIB-SEM microscope at the University of Chicago, a 1 µm × 10 µm area of interest was coated with Pt to protect it from damage by the FIB, and a lamella was lifted out of 4 target grains with compositions identified as plagioclase, olivine, ilmenite and an agglutinate that was initially misidentified as a clinopyroxene. These lift-outs were performed close (within 10 µm) to the location of lamellae extracted for correlative TEM analyses, but far enough to avoid beam damage from previous FIB sample preparation. Out of each lamella, 4 to 5 nanotips, labeled A to E, were prepared using the methods outlined in chapter 2 and analyzed with a CAMECA LEAP 5000XS at the NUCAPT facility of Northwestern University. Tomographic reconstructions were done with CAMECA's IVAS software. TEM analyses were done with a Thermo Scientific Themis Z monochromated and aberration-corrected TEM equipped with a Gatan Quantum 965 EELS detector at Purdue University (Kling et al., 2022).

4.4 RESULTS

A total of 17 nanotips were analyzed for their space weathering features, with 8 providing useful data. From the four different materials analyzed for this project, only the ilmenite and olivine nanotips contained vesicles in the samples that could be tomographically reconstructed. The agglutinate tips contained various Fe-rich structures, while the feldspar was homogenous. The feldspar more easily field-evaporated than the Pt cap protecting it, so in order to prevent tip failure, the cap needed to be completely milled away. Therefore, the outermost 10 nm may be missing from this sample. The mass to charge state ratio spectra are presented in Figures 4-1 and 4-2.

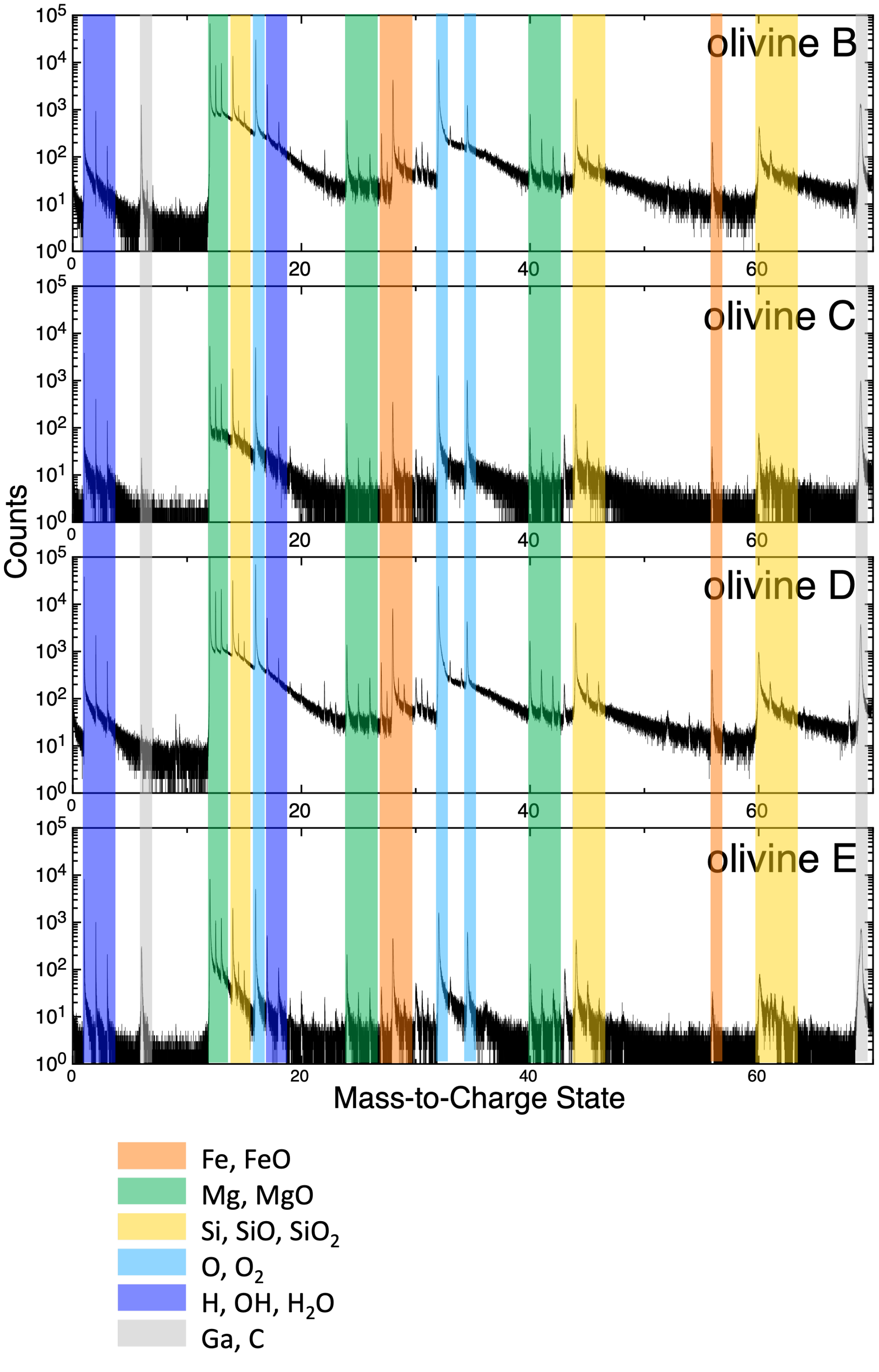

Figure 4-1: Mass-to-charge state ratio spectra of the successful tips in the olivine grain.

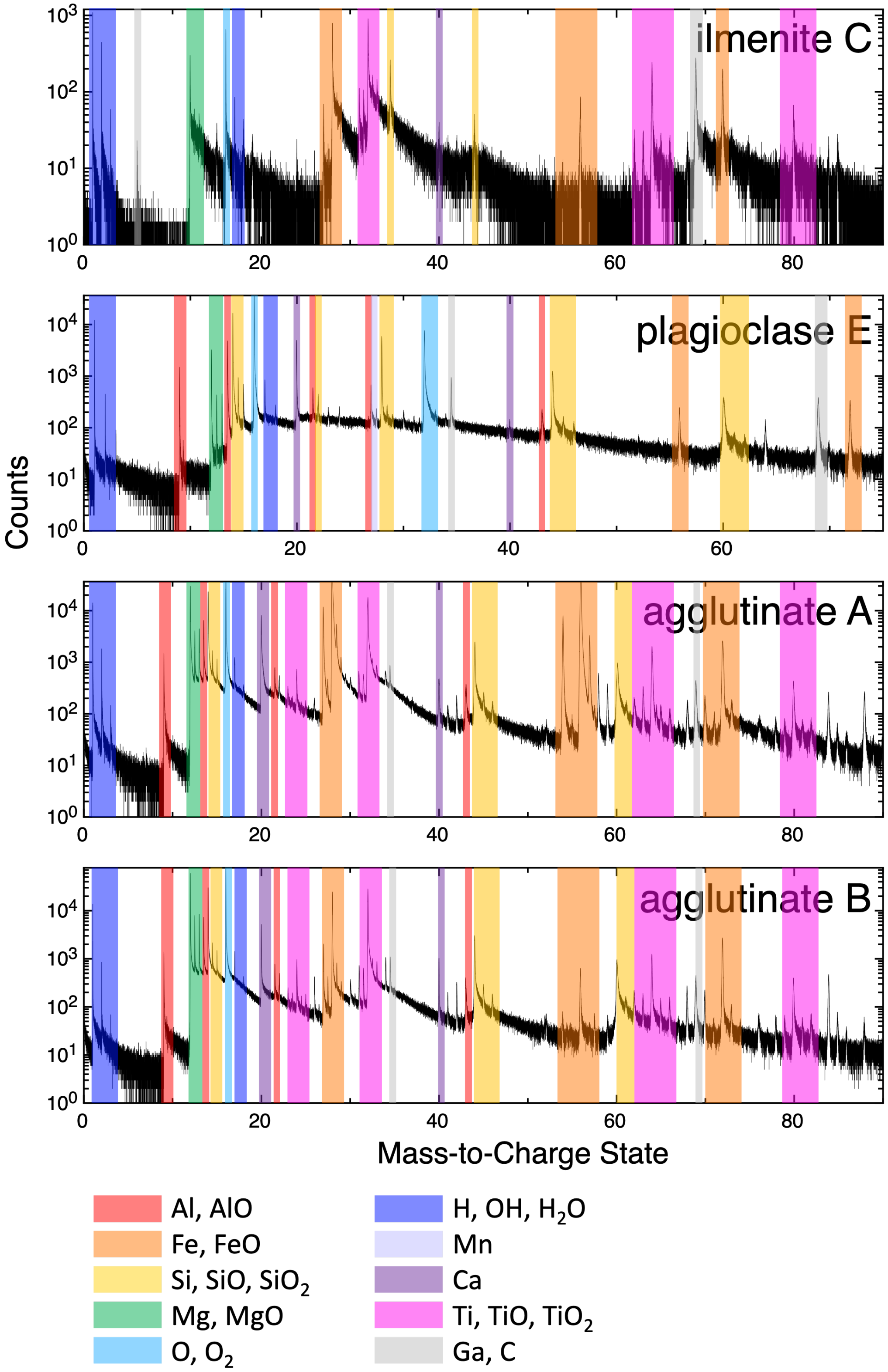

Figure 4-2: Mass-to-charge state ratio spectra of the successfully analyzed tips from the mature ilmenite, plagioclase, and agglutinate lunar soil grains.

4.4.1 Olivine

Olivine nanotip A only showed capping materials. Olivine nanotip B also contained capping materials (Pt and C), but only at the top 10 nm, verifying that this tip captured the outermost olivine grain surface. Nanotip C did not preserve the outermost surface, but did contain a large void space. This tip fractured after a relatively short analysis run (only analyzing several 100k of atoms, or analyzing only several nm of material deep in to the tip) , likely because the void space, likely a spherical vesicle, reached into the volume that was being field-evaporated and caused the mechanical failure that ended the analysis. Nanotip D did not have capping materials, but the slightly increased concentration of Pt at the top suggests that it captured the area very close to the surface of the grain.

Olivine nanotip E contains capping material, some of which filled in a cavity in the surface. This could be a vesicle that was exposed to the surface before sample analysis rather than an inclusion that plucked out. This tip also contained a large void space that appears to be part of a network of defects. There are also some smaller void spaces that appear to be vesicles. This tip fractured likely because the defect passed through the tip, resulting in a tip geometry that is not stable during field-evaporation.

Olivine nanotip E contains capping material, some of which filled in a cavity in the surface. This could be a vesicle that was exposed to the surface before sample analysis rather than an inclusion that plucked out. This tip also contained a large void space that appears to be part of a network of defects. There are also some smaller void spaces that appear to be vesicles. This tip fractured likely because the defect passed through the tip, resulting in a tip geometry that is not stable during field-evaporation.

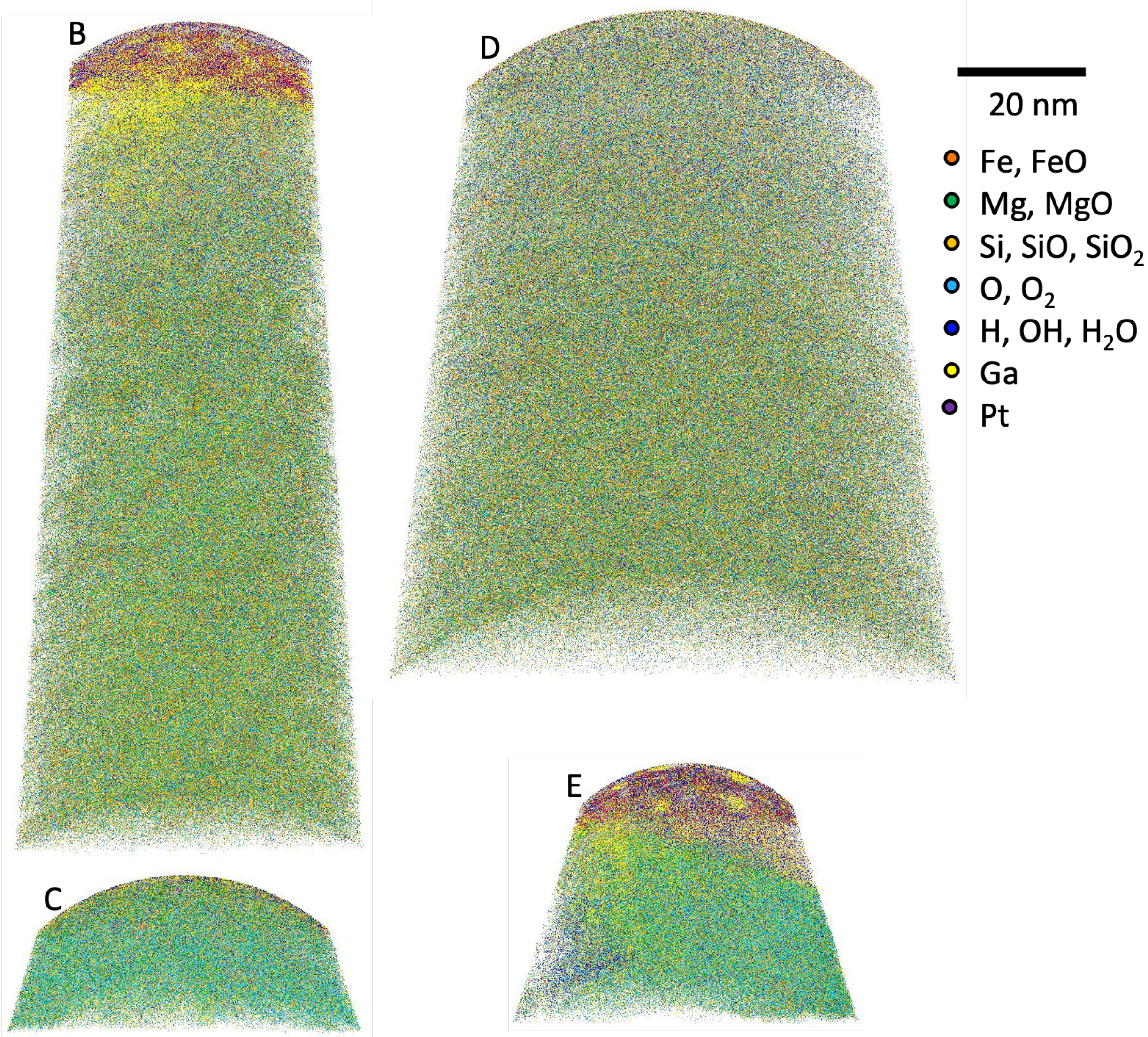

Figure 4-3: 2D projections of tomographic reconstructions of the four successful olivine tip analyses that comprise at least 1M atoms. Mineral grain surface at top here and in all subsequently shown reconstructions.

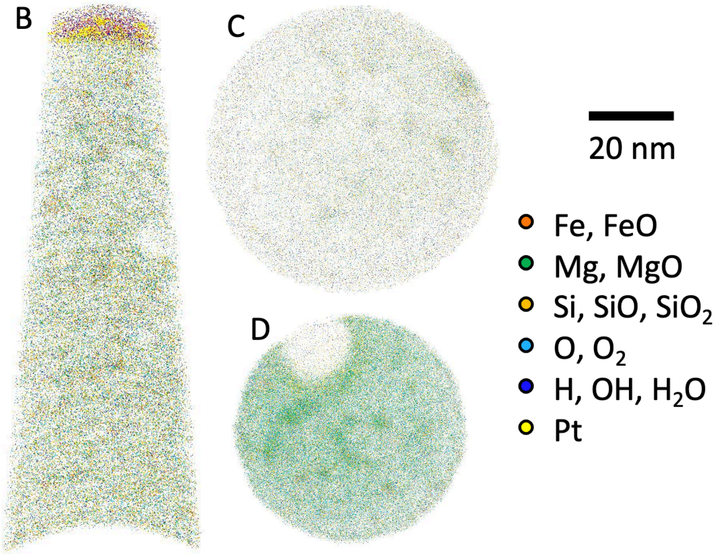

Figure 4-4: Slices through the reconstructions of olivine tips B, C, and D.

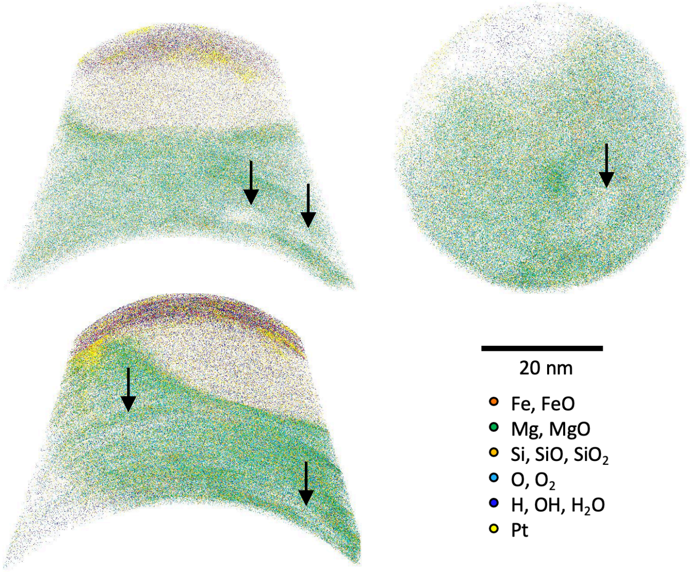

Figure 4-5: Slices in x, y, and z through olivine tip E. Some of the irregularly shaped void spaces are labeled with black arrows.

This particular olivine grain is Mg-rich. Several nanotips preserved the outermost surface of the grain (Figure 4-3), but lack nanophase Fe particles. Other nanotips had zones of decreased density that could be interpreted as vesicles (such as in the upper left of tip D, Figure 4-4). These zones were enriched in H-bearing species relative to the other elements present in olivine. Other tips showed areas of increased density, which are represented as clusters of increased concentration in all elements. The void space structures can be quite complex, as seen in Figure 4-5. Some of the void spaces are not simply individual, isolated bubbles but complex interconnected networks.

4.4.2 Agglutinate

There were no regions of decreased density that could represent vesicles in the two agglutinate nanotips. Instead, these nanotips are dominated by Fe-rich structures, including wisps of increased oxidation with an ilmenite-like composition and a microphase Fe particle. Although TEM images (Figure 4-6) show that there are vesicles present, in the two nanotips that we analyzed we do not see these features. The vesicle-rich layer across the surface is not continuous, so they may not have been sampled by these tips. It is also possible that the atom probe sampled a volume of different composition than the TEM lamella, as it appears there are multiple lithologies present in the single grain.

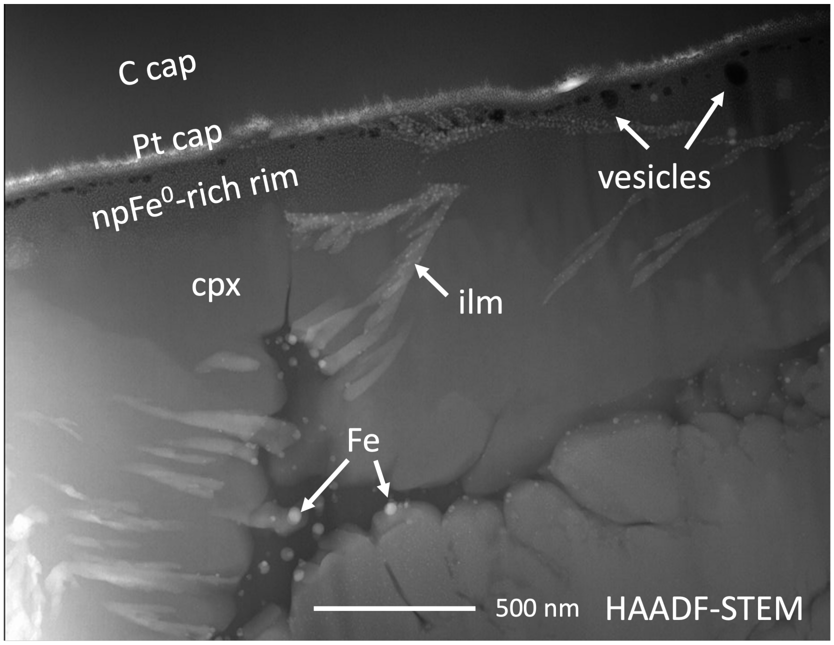

Figure 4-6: Dark field STEM image of a slice of the agglutinate grain. Vesicles appear as dark areas while Fe particles appear as light areas.

Agglutinate tip A contains a large microphase Fe particle with a Ti-rich rim (Figure 4-7). Though this particle is pure Fe, there is a Fe and Ti-rich structure at the top of the tip where the two components are mixed. At the base of this tip, all elements are homogenous. Agglutinate tip B contains some nanophase Fe particles at the very top (Figure 4-8), before transitioning into an area that is more homogenous. At the base is a Fe and Ti-rich vein similar to that seen at the top of tip A. While these veins contain nanophase Fe in the TEM image, we do not see these features in the APT samples.

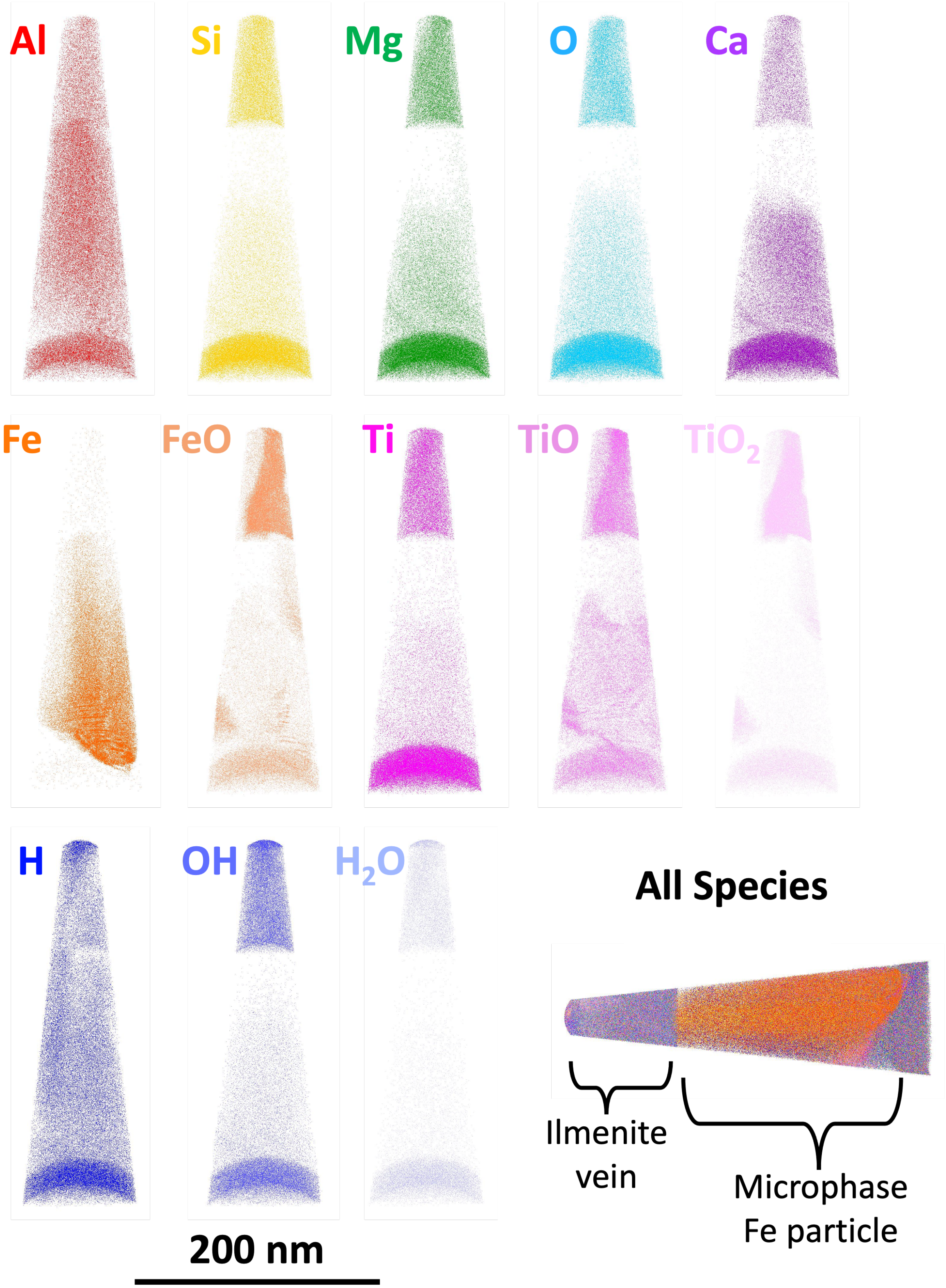

Figure 4-7: Tomographic reconstructions of agglutinate tip A; 2D projections of all atoms.

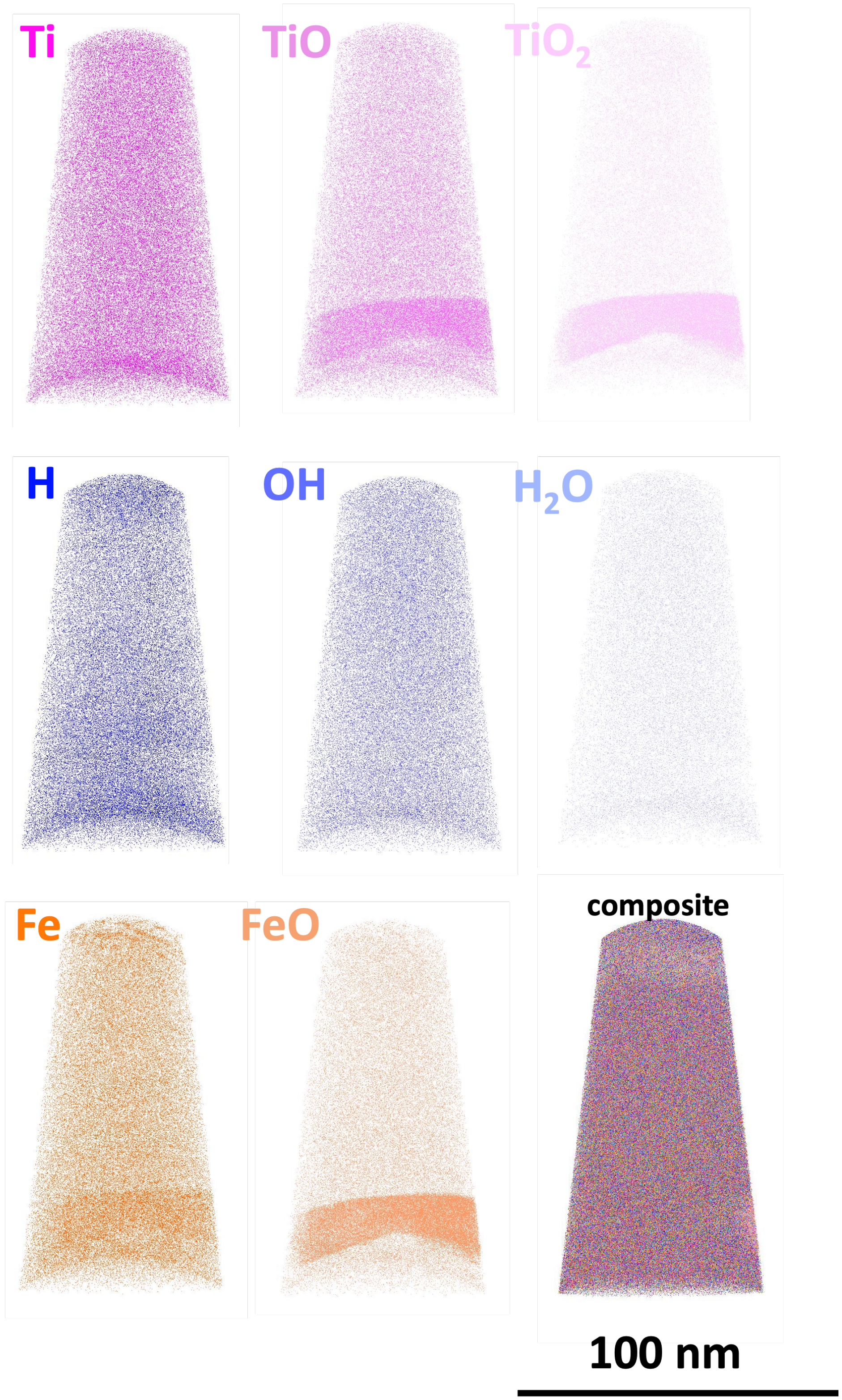

Figure 4-8: 2D projections of tomographic reconstructions of agglutinate tip B.

4.4.3 Feldspar

A total of 5 nanotips were prepared from a lamella milled out of the grain that was identified as plagioclase feldspar by TEM. Three of these nanotips tips fractured without reaching target material, while another fractured at the Pt cap/feldspar interface. Due to the circumstances of the tip failures, the remaining Pt on the fifth nanotip was milled away. Because of this, the uppermost 10 nm of the surface of the grain may be missing. However, there is a small amount of Pt at the apex of the nanotip, and therefore perhaps only part of an irregular top ~5 nm of the grain surface is not sampled.

The major elements present in the feldspar nanotip are Ca, Al, Si, and O, representing the anorthite endmember of plagioclase. Elements that are present at lower abundances include Mg, Mn, and Fe. Mg and Mn are more abundant deeper into the tip, further away from the surface, while Fe is present in higher concentrations at the top of the tip. Mg and Mn are distributed homogenously, whereas the Fe is distributed heterogeneously, forming clusters of increased concentration (Figure 4-9), but not as pure Fe-bearing particles, such as npFe^0, as these clusters are not solely Fe and contain other major elements present in the mineral. The presence of these elements may be due to redeposition from other minerals, but are not clearly present as a redeposition rim. There were no unambiguous void spaces present.

We interpret the H present in this nanotip as solar-wind implanted H. OH and H_2O have concentration profiles consistent with adsorbed species- increased concentration at the apex of the sample, which then sharply levels off. The H concentration decreases in a more linear pattern for the first 35 nm before beginning to level off to a constant concentration. Such a profile is consistent with H intrinsic to the sample rather than H from the analysis chamber (Daly et al. 2021). However, this profile does not match that of simulated implanted solar wind (as presented in Chapter 3), requiring mobility of H.

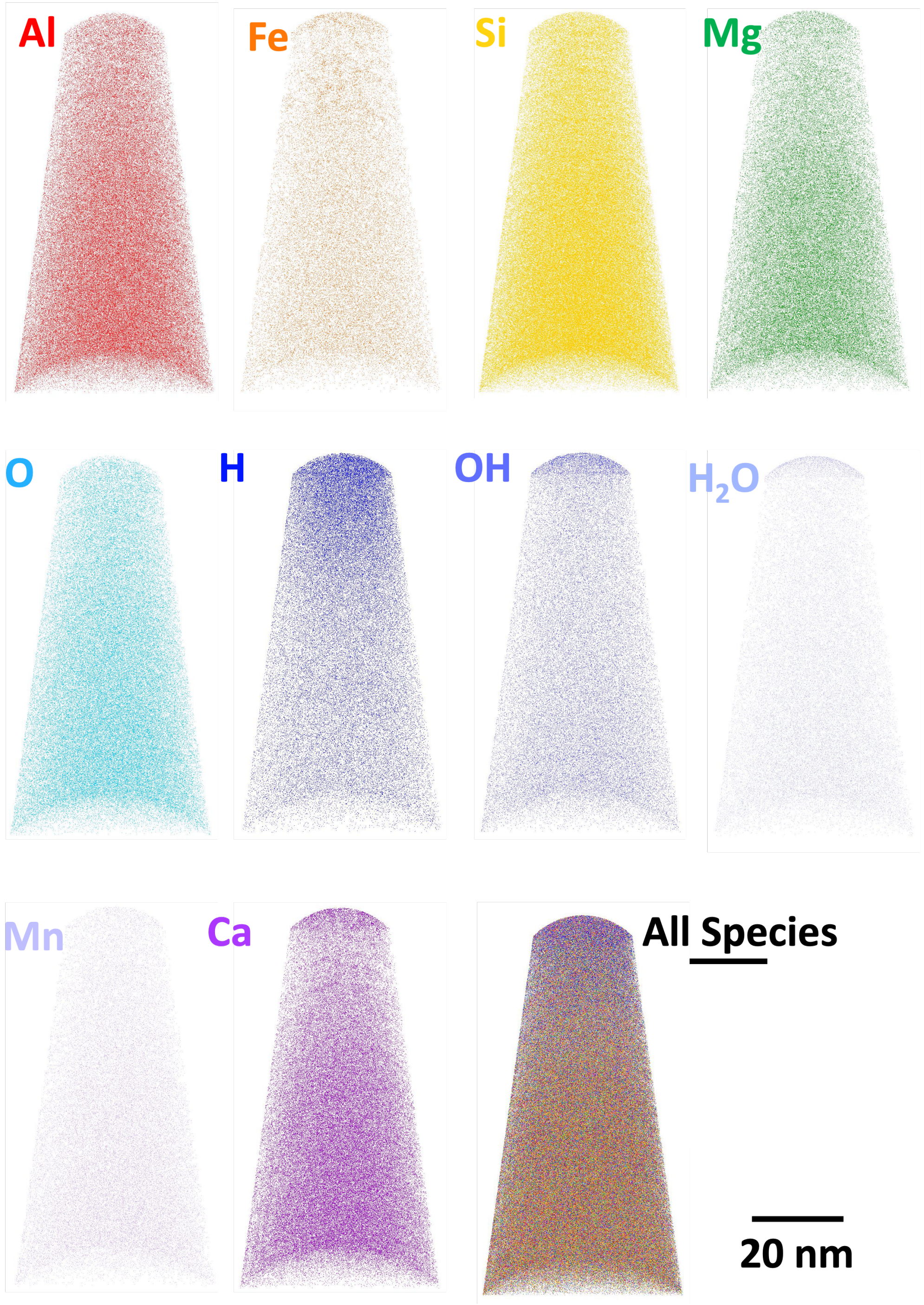

Figure 4-9: 2D projections of tomographic reconstructions of feldspar tip E.

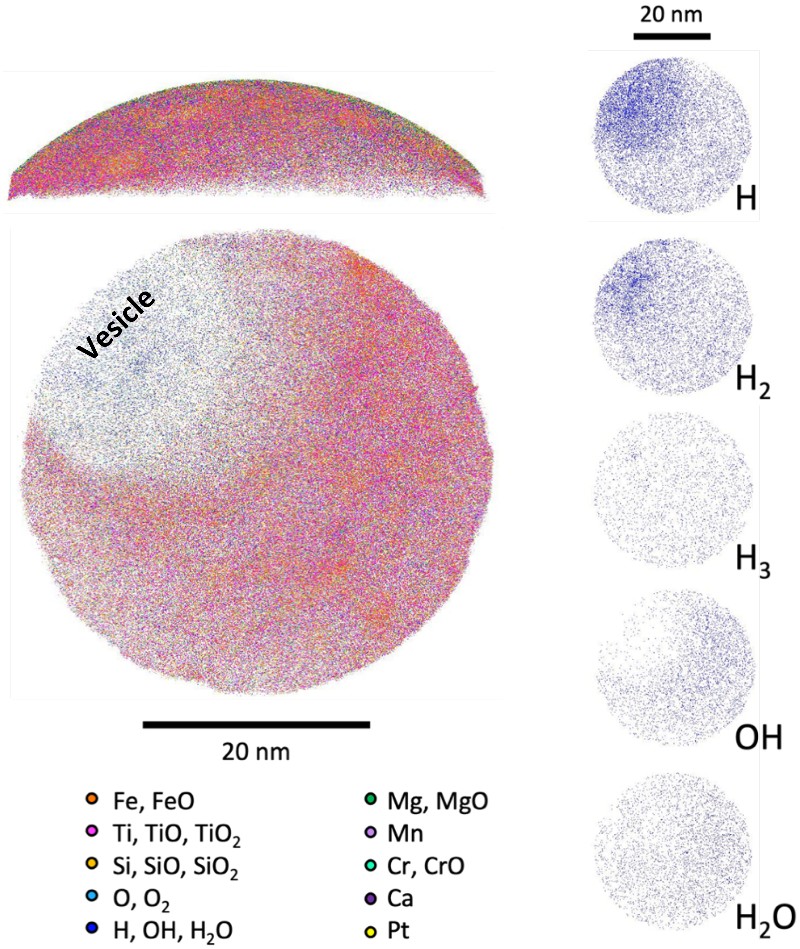

Figure 4-10: 2D projections of tomographic reconstructions of the ilmenite tip. The left column shows the tip from the side and looking down the z axis, respectively. The right column shows the distribution of H species in the same tip looking down the z-axis, with important species labeled. The vesicle is apparent in the 1st quadrant of the top-down projections.

4.4.4 Ilmenite

A total of 5 nanotips were prepared from a lamella lifted out of the grain that was identified as ilmenite by TEM. Only one nanotip returned data from the target material, and only sampled a few nm in depth. Despite this small dataset, there are still features that can be analyzed. The major elements present in this sample are Fe, Ti, and O with some Mg and Si. Both Ti and Fe are distributed heterogeneously. We observed a large void space (vesicle) measuring about 20 nm across, which contains H and H-bearing species, and a small amount of ^{4}He (see discussion section) which anticorrelate with the concentrations of Fe, Ti, O, Mg and Si, the of major and minor elements of ilmenite. A small burst of ions at mass-to-charge-state ratio 3 (Figure 4-10, middle right), interpreted as H_3, was detected at the top the vesicle (Figure 4-10).

4.5 DISCUSSION

Each nanotip presents a unique composition and structure, even though they are only separated by 1 µm on the grain's surface, consistent with what was observed in the submature lunar soil described in Chapter 3. Here, I presented a series of nanotips from a sample that was classified as mature based on bulk analyses but find that the space-weathering products are different in each tip even when extracted from the same grain. The nanoscale distribution of the space-weathering products highlights the complexity of space weathering products. In chapter 3 we describe a vesicle in a lunar ilmenite grain from Apollo 17 submature sample Soil 71501 with a possible ^{4}He detection (3±2 atoms, 1σ above background). This vesicle was similar in size (~8 nm × 14 nm) to the mature ilmenite nanotip presented in Figure 4-10 (~11 nm × 16 nm). This sample (Figure 4-10) also included a possible He signal. The burst at the top of the vesicle included an increased detection of H_2 and H_3 and ^{4}He (7±3, 1σ, above background; ^{3}He is too low in abundance to be detected here). Like the nanotip described in chapter 3, this sample is missing at least 3 orders of magnitude of He atoms when compared to whole grain analyses (Benkert et al., 1993). Although the detected amount of He is significantly less than the estimated He content from whole grain analyses of other grains from this soil sample (see discussion in Chapter 3; Greer et al., 2020), the ^{4}He peak in the mass spectrum is above the background and above the ^{4}He signal anywhere else in the sample. To determine this, we measure only 0 to 2 counts of ^{4}He counts in a volume of identical geometry as the vesicle at random locations in the sampled volume outside the vesicle.

This requires He loss likely during the opening and degassing of the vesicle as the top of the nanotip was eroded during analysis. The increased concentration of H and He species detected at the top of these vesicles suggests that the gaseous contents largely escaped into the vacuum without being analyzed, with only a small fraction of these atoms or molecules being ionized and detected, resulting in the increased detection.

The detection of He in vesicles in space weathered samples using APT remains a challenge as closed vesiculated textures in space weathered samples have non-ideal geometries. The topography of the nanotip is not symmetrical and hemispherical due to the presence of these vesicles, which may change the local electric field in ways that lead to nanotip failure. Vesicles that are open to the nanotip's surface and not fully infilled with capping Pt may introduce an instability that leads to nanotip failure during analysis.

The complex network of vesicles and defects that are filled with implanted solar wind may not be resolvable with APT; as these features change the field-evaporation pattern in the tip, the exact location of some of the ions is not preserved. It appears that smaller vesicles manifest themselves as clusters, while larger ones appear as void spaces. The larger void spaces display more structure, but it is possible that this is true for the smaller vesicles as well but this is not preserved in the reconstruction.

Direct comparison with the samples analyzed in Chapter 3 is difficult: although ilmenite was included in the mature samples that were analyzed so that they could be compared to the submature soil, the mature ilmenite tips did not capture a full profile of space weathering products. The mature ilmenite tip (tip C) with the highest counts sampled less than 5 nm depth before it fractured. It is likely that the other mature ilmenite tips fractured due to the increased concentration of vesicles, which altered the electric field at the apex of the tip enough so that the tip became mechanically unstable. The data that was collected is similar to that of the immature samples. Both contain vesicles with increased counts of He as well as nanophase Fe.

The well-defined Noguchi zones (Noguchi et al., 2014) that were described in olivine, pyroxene, and plagioclase from samples collected on asteroid Itokawa by JAXA's Hayabusa mission and were displayed in chapter 3 are not present here. Zone I, the redeposition rim, was not present in any of the APT tips; in addition, this layer was not apparent in any of the TEM sections (Figure 4-6). Zone II, the area with nanophase Fe particles, was not ubiquitous throughout all Fe-bearing mineral samples. There were no npFe^0 present in the olivine tips. The ilmenite tip was the sample with the most obvious clustering in Fe, though this was also present in the feldspar tip, despite the low concentration of Fe. The presence of npFe0 is not limited to the surface of the grains- as seen in Figure 4-6, npFe0 can be present quite deep, several hundred nm, into the sample, in the ilmenite veins. This is evidence of complex reworking of this sample which could be processing by something other than space weathering, likely meteorite impacts that can cause regolith gardening and (partial) melting and can result in grains experiencing complex space exposure histories and reprocessing.

4.6 CONCLUSIONS

The nanotips analyzed by APT from soil 79221 exhibit more complex structures than those seen in the nanotips made from the ilmenite of soil 71501, which are a product of their increased exposure to the space weathering environment and meteorite impacts. Such structures include the irregularly shaped void spaces and heterogenous Fe structures that are not simply nanophase or microphase Fe. The space-weathered regions of these samples are also more complex than the features seen in Itokawa particles, which are generally limited to redeposition rims, nanophase Fe, and vesicles (Noguchi et al. 2014). Despite these samples ostensibly having the same level of maturity, the variable alteration of the different minerals is broadly expressed, from the slight heterogeneity of the feldspar to the intensely vesiculated ilmenite. With such diversity at the nanoscale in only 4 mineral samples, it is unlikely that the full complexity of these samples has been explored, and more analysis of mature samples from this soil is needed.

4.7 REFERENCES

Benkert, J.-P., H. Baur, P. Signer, and R. Wieler. "He, Ne, and Ar from the solar wind and solar energetic particles in lunar ilmenites and pyroxenes." *Journal of Geophysical Research: Planets* 98, no. E7 (1993): 13147-13162.

Bradley, J. P., H. A. Ishii, J. J. Gillis-Davis, J. Ciston, M. H. Nielsen, H. A. Bechtel, and M. C. Martin. "Detection of solar wind-produced water in irradiated rims on silicate minerals." *Proceedings of the National Academy of Sciences* 111, no. 5 (2014): 1732-1735.

Burgess, K. D., and R. M. Stroud. "Phase-dependent space weathering effects and spectroscopic identification of retained helium in a lunar soil grain." *Geochimica et Cosmochimica Acta* 224 (2018): 64-79.

Daly, L., M. R. Lee, L. J. Hallis, H. A. Ishii, J. P. Bradley, P. Bland, D. W. Saxey, D. Fougerouse, W. D. A. Rickard, L. V. Forman, N. E. Timms, Jourdan, F., S. M. Reddy, T. Salge, Z. Quadir, E. Christou, M. A. Cox, J. A. Aguiar, K. Hattar, A. Monterrosa, L. P. Keller, R. Christoffersen, C. A. Dukes, M. J. Loeffler, and M. S. Thompson "Solar wind contributions to Earth's oceans." *Nature Astronomy* 5, no. 12 (2021): 1275-1285.

Greer, J., S. S. Rout, D. Isheim, D. N. Seidman, R. Wieler, and P. R. Heck. "Atom probe tomography of space-weathered lunar ilmenite grain surfaces." *Meteoritics & Planetary Science* 55, no. 2 (2020): 426-440.

Keller, L. P., S. J. Wentworth, D. S. McKay, L. A. Taylor, C. Pieters, and R. V. Morris. "Space weathering in the fine size fractions of lunar soils: Soil maturity effects." *New Views of the Moon 2: Understanding the Moon Through the Integration of Diverse Datasets* (1999): 32.

Kling, A. M., J. Greer, M. S. Thompson, and P. R. Heck. "Identification of solar wind-sourced water in the space weathered rims of lunar soils." *LPI Contributions* 2678 (2022): 1504.

Laczniak, D. L., M. S. Thompson, R. Christoffersen, C. A. Dukes, S. J. Clemett, R. V. Morris, and L. P. Keller. "Characterizing the spectral, microstructural, and chemical effects of solar wind irradiation on the Murchison carbonaceous chondrite through coordinated analyses." *Icarus* 364 (2021): 114479.

Noguchi, T., M. Kimura, T. Hashimoto, M. Konno, T. Nakamura, M. E. Zolensky, R. Okazaki et al. "Space weathered rims found on the surfaces of the Itokawa dust particles." *Meteoritics & Planetary Science* 49, no. 2 (2014): 188-214.

Pieters, C. M., and S. K. Noble. "Space weathering on airless bodies." *Journal of Geophysical Research: Planets* 121, no. 10 (2016): 1865-1884.

Taylor, L. A., C. Pieters, L. P. Keller, R. V. Morris, D. S. McKay, A. Patchen, and S. Wentworth. "The effects of space weathering on Apollo 17 mare soils: Petrographic and chemical characterization." *Meteoritics & Planetary Science* 36, no. 2 (2001): 285-299.

Thompson, M. S., T. J. Zega, P. Becerra, J. T. Keane, and S. Byrne. "The oxidation state of nanophase Fe particles in lunar soil: Implications for space weathering." *Meteoritics & Planetary Science* 51, no. 6 (2016): 1082-1095.

Thompson, M. S., T. J. Zega, and J. Y. Howe. "In situ experimental formation and growth of Fe nanoparticles and vesicles in lunar soil." *Meteoritics & Planetary Science* 52, no. 3 (2017): 413-427.

CHAPTER FIVE: ATOM PROBE TOMOGRAPHY OF 4.45 BILLION YEAR OLD LUNAR ZIRCON FROM THE APOLLO 17 CIVET CAT NORITE CLAST

5.1 ABSTRACT

The crystallization ages of rock lithologies from the Moon provide critical constraints on the minimum age formation of the Moon and its early evolution. Here we report atom probe tomography of a previously dated zircon grain from the ‘Civet Cat’ norite fragment found in the Apollo 17 lunar impact melt breccia 72255 and show that the absence of nanoscale clusters of excess mobile radiogenic lead supports a 4.46 Gyr ago U-Pb crystallization age for the zircon grain. The deformed zircon crystals preserved ancient domains with a concordant average uranium-lead radiometric age of 4,461 ± 33 Myr ago (Zhang et al., 2021), pushing the minimum formation age of the lunar crust back by ~ 40 Myr. The significance of this age holds on the preservation of domains which may have been modified by post-crystallization processes. The atomic spatial resolution of individual mineral grains supports the earliest evidence of planet-wide crust evolution in the Solar System and a minimum age for the giant impact event that formed the Earth-Moon system.

5.2 INTRODUCTION

The leading hypothesis for the formation of the Earth-Moon system is the Giant Impact hypothesis where a Mars-sized object collided with growing proto-Earth (Cameron and Ward 1976; Canup 2004), which may have resulted in a globally molten Moon known as the lunar magma ocean

(LMO; Wood et al. 1970). The LMO model explains the proposed structure of the lunar interior, with dense mafic materials forming the mantle, a felsic anorthositic crust, and a uniform residual liquid with high concentrations of incompatible elements potassium, rare-earth elements, and phosphorus (KREEP) crystallizing between the two (Warren 1985).

The timing of the Giant Impact is debated (Borg et al., 2015). ^{182}Hf-^{182}W radiogenic systematics (Thiemens et al., 2019), Hf model ages (Barboni et al., 2017) and dynamical modelling (Bottke et al., 2015) place the Moon-forming event early in the Solar System's history, between 4.52 to 4.47 billion years ago, whereas lunar Pb model ages (Connelly and Bizzarro, 2016) and thermal modeling (Maurice et al., 2020) place it in the range of 4.43 to 4.42 billion years ago. Zircon crystallization was likely part of the urKREEP – the primordial KREEP component – because of the enrichment in incompatible elements needed to form this mineral (e.g., Warren and Wasson, 1987), and was therefore part of the initial crystallization of the LMO. The U-Pb system in zircon is a particularly robust lunar chronometer, as the zircons readily incorporate U but not Pb into their crystal lattices. The U-Pb chronology of lunar zircon provides constraints on the LMO crystallization and the minimum timing of the giant impact. A precise lower age limit for LMO crystallization is given in Nemchin et al. (2009), which reported a SIMS U-Pb zircon age of 4417±6 Myr ago from Apollo 17 sample 72255. A prolonged duration of the LMO is favored by the geochronology of multiple lunar suites: the source of mare basalts, selected ferroan anorthosites, urKREEP, Mg-suite and zircon have concordant ages of ~4.3 Ga (Borg et al., 2015).

Zhang et al. (2021) reported the U-Pb isotopic composition of six zircon grains using NanoSIMS (Nanoscale Secondary Ionization Mass Spectrometry) on a total of 15 spots in Apollo 72255 Civet Cat norite. The euhedral and subhedral zircons in this sample are small (10 to 25 µm; Figure 5-1). The five oldest ages have a weighted mean Pb-Pb age of 4452±35 Myr ago, and define a concordant U-Pb average age of 4461±35 Myr ago. These U-Pb ages have the potential to constrain the lower limit of timing of Giant Impact and LMO crystallization at 4460 Myr ago. However, the ancient zircon ages reported by Zhang et al. (2021) could result either from radiogenic Pb mobilization or the mixing of Pb-retention and Pb-loss nanodomains. In the former scenario, radiogenic Pb mobilization could compromise the authenticity of zircon U-Pb ages (Ge et al., 2018, 2019; Kusiak et al., 2013a,b), while in the latter, the ancient ages of the Civet Cat norite zircons should be intrinsic normal Pb-loss domains (Arcuri et al., 2020).

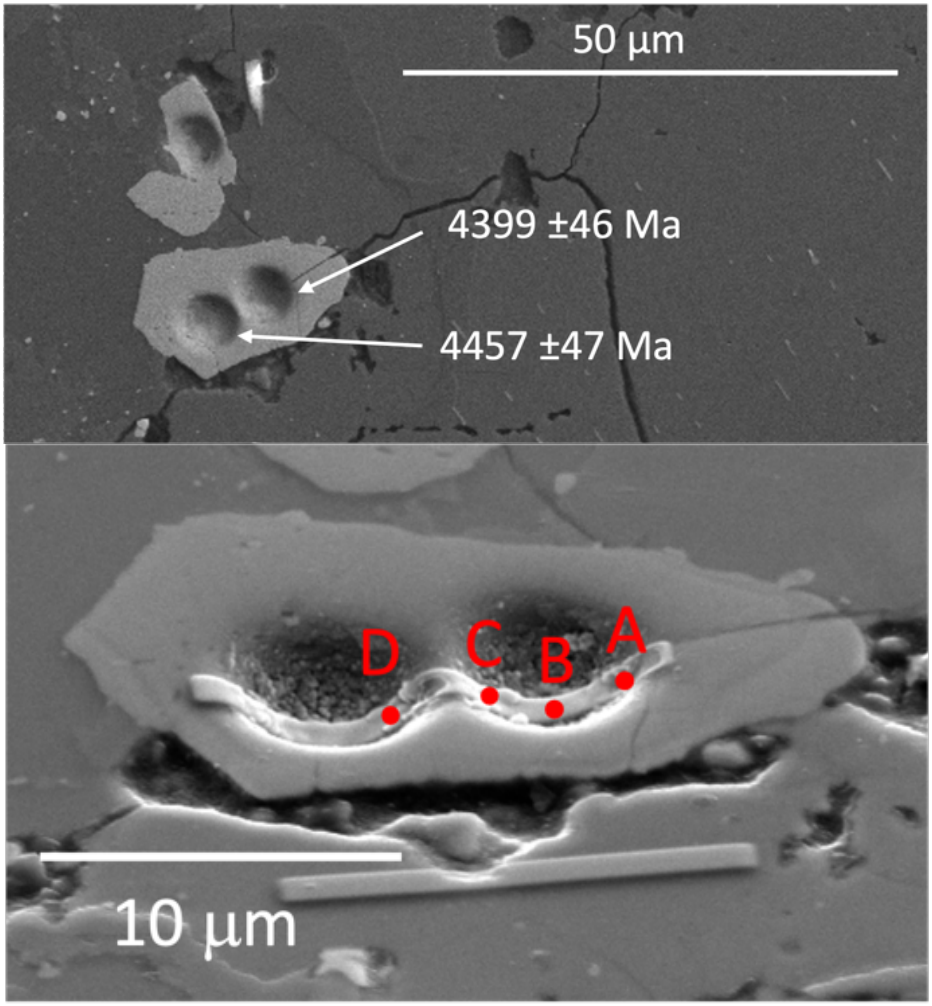

Figure 5-1. Images of zircon. Top: top-down image showing SIMS pits; bottom: image tilted at 55°, showing zircon with Pt deposit to be lifted out. The approximate positions of the successfully analyzed APT samples are labeled.

Here, we use a nanometer-scale tomographic mass spectrometry method, atom-probe tomography (APT), to investigate the Pb spatial distribution within an old lunar zircon domain to test if the ancient zircon ages in Civet Cat norite by Zhang et al. 2021 are authentic. Zircon Z14 (^{207}Pb/^{206}Pb age = 4453 ± 34 Myr ago; Figure 5-1) is one of the six oldest domains in the Civet Cat norite (Zhang et al., 2021) and hence is selected for APT analysis to investigate its Pb distribution at the nanoscale in this study. During APT analysis, atoms of a sample tip are field-evaporated through a combination of high surface fields and laser pulses and analyzed with position-sensitive time-of-flight mass spectrometry, yielding the three-dimensional distribution of elements and isotopes throughout the analyzed sample (i.e., Fig 2). Atom-probe tomography has been previously used in conjunction with SIMS to investigate if Pb was mobilized at the nanoscale and date up to 4.4 Ga terrestrial zircons (Hadean Jack Hills, Valley et al., 2014, Valley et al., 2015; Archean Beartooth Mountains, Blum et al., 2017), and in the case of the Jack Hills zircons, verifying the ancient SIMS ages. The APT method showed that nanoscale Pb clustering is usually associated with Y clustering (as shown in Valley et al., 2014), which is the result of the enrichment of less compatible elements after the formation of the zircon. These Pb clusters, while demonstrating heterogeneity in Pb distribution, are much smaller than that of the SIMS spot used to date the zircon (clusters are ~10 nm in diameter, SIMS spot is 10s of µm), and are therefore homogenous on the scale of the SIMS analysis. The APT has a 100× higher spatial resolution than previous analyses of this zircon using NanoSIMS (which uses a smaller spot size a few µm across in order to analyze a statistically significant number of atoms to produce an age), and can analyze samples at near-atomic resolution.

5.3 METHODS

The zircon grain Z-14 used in this study measures 22 × 12 µm, (Figure 5-1) and was analyzed for U-Pb systematics by Zhang et al. (2021) using NanoSIMS and SIMS. The size of the grain presents some challenges in APT sample preparation. A strong bond to the substrate is essential as the mechanical stresses at the tip are large, and a weak point in a sample can lead to specimen fracture during APT analysis (Kelly and Miller, 2007). A large thick base allows heat introduced by the laser to be more efficiently conducted away from the apex of the tip to its base. Grain boundaries represent weak points, and therefore the tips from this zircon need to be shorter than tips from larger zircon grains, such as those in Valley et al. (2014), to make sure that the grain boundary is not included. A lamella of approximately 1 × 10 µm was milled with a focused ion beam (FIB), lifted out (Figure 5-1) using a micromanipulator and firmly attached onto Si flat-topped posts with gas injection system (GIS)-deposited Pt. Subsections of the zircons were further milled to produce the nanotips as seen in Figure 2-6. The material within several tens of nm of the surface could have been subjected to sputtering-induced amorphization during NanoSIMS analysis (Aléon-Toppani et al., 2021), therefore the tips were made to exclude this zone using a FIB that milled away the top material.

Atom-probe tomography works by applying a high electric field in conjunction with a pulsed picosecond UV laser that leads to field-evaporation of atoms from a sample shaped to a nanotip. The field-evaporated ions are then accelerated through a local electrode and detected by a position-sensitive multichannel plate. This gives both the composition and distribution of the elements and isotopes in a sample. We used a Cameca LEAP 5000 XSi equipped with a picosecond UV laser, with a wavelength of 355 nm, energy of 50 or 200 pJ and a repetition rate of 200 kHz. A total of six nanotips were analyzed from zircon Z-14. Tips A, B, and C were located in the (right)

NanoSIMS pit (Figure 5-1) that gave a Pb-Pb age of 4399±46 Myr ago, and tips D, E, F were located in the (left) NanoSIMS pit that gave a Pb-Pb age of 4457±47 Myr ago. The first two tips (E, F) were unsuccessful, and fractured before steady-state evaporation. These tips were analyzed

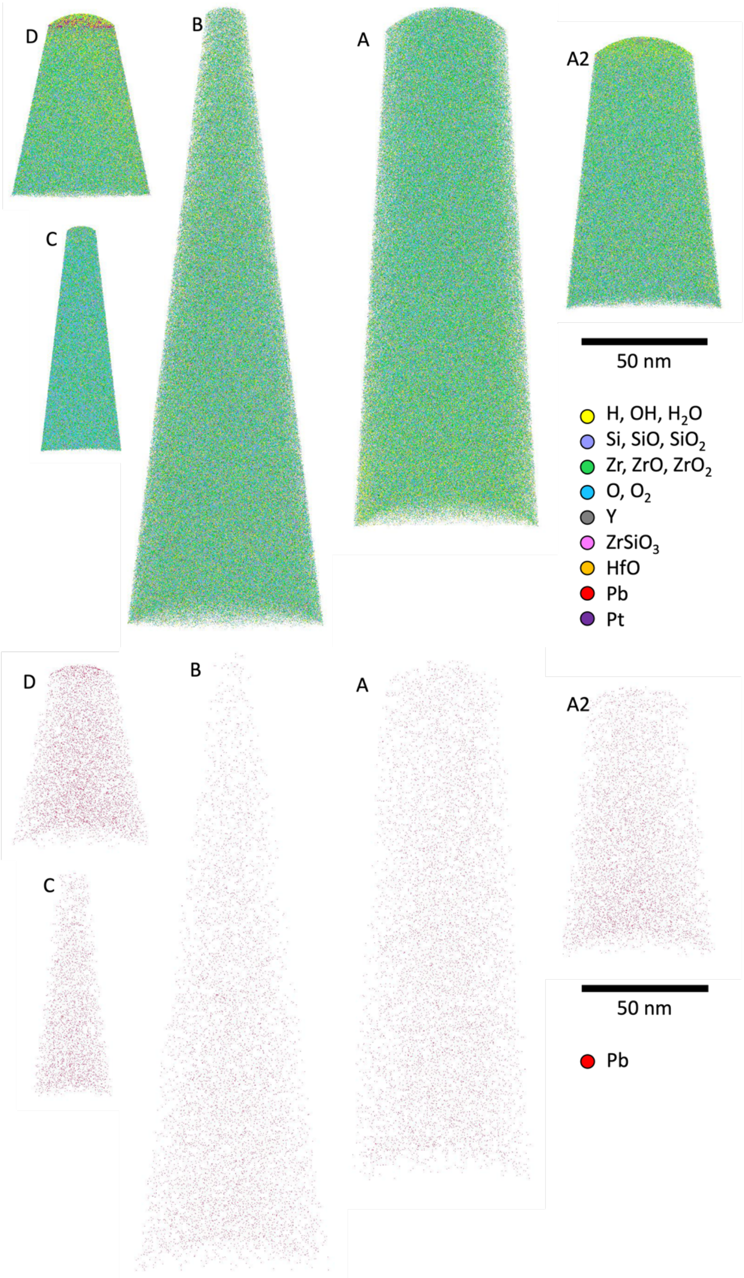

Figure 5-2. Reconstructions of the nanotips. The top image shows the major ionic species present, with each ion identified as an individual point and color coded, while the bottom shows just $^{208}Pb^{++}$ in red. Since these are 2D projections of 3D data, as a result some pixels appear closer to each other than average and may appear as clusters, but these projection artifacts are not real and not present in 3D space.

with APT conditions (pulse energy = 200 pJ) that have been previously reported for zircon (e.g., Valley et al., 2014), but these high pulse energies turned out to be unsuitable for these samples. Of the four successful tips, all were analyzed with 50 pJ laser energy. The run for Tip A was stopped manually, then resharpened and reanalyzed as Tip A2 (Table 5-1).

Tip Name	Temperature (K)	Pulse Energy (pJ)	Pulse Rate (kHz)	Total # of detections	Length of tip (nm)
F	50	200	200	n/a	n/a
E	50	200	200	n/a	n/a
D	30	50	200	~14.5 M	~70
C	50	50	200	~7.5 M	~90
B	50	50	200	~18.3 M	~240
A	30	50	200	~31.6 M	~200
A2	30	50	200	~15.0 M	~110

Table 5-1. Summary of the APT analytical conditions and yields from the zircon nanotips. Unsuccessful analyses are denoted by n/a in the total # of detections and length of tip columns.

5.4 RESULTS

A total of five nanotips were successfully produced from a lamella of zircon lifted out of the pits (Figure 5-1) produced by NanoSIMS analysis. The nanotips were shaped to sample a volume immediately adjacent to the material analyzed by NanoSIMS, to not include material that had been amorphized due to NanoSIMS primary ion beam damage. The tips were instead extracted from several hundred nm beneath the analyzed surface. Species that were detected include the major elements in zircon (Zr, Si, O), various H species, Y, HfO, Pb, and Th (Figure 5-2, Figure 5-3). The only isotope of Pb detected above background is $^{208}Pb^{++}$, which can be used as a proxy for all Pb isotopes as they are expected to exhibit the same chemical behavior during secondary processes on the Moon. In the tomographic reconstructions of the datasets, we find no evidence of clustering of Pb, Y, or any other elements. We used the nearest neighbor distribution analysis, one of the most robust ways to assess clustering. In nearest neighbor analysis, each Pb atom is examined for the closest distance to the next Pb atom, and the distribution of the distances is plotted (red, Figure 5-4). This is then compared to a random distribution of points (black, Figure 5-4). All

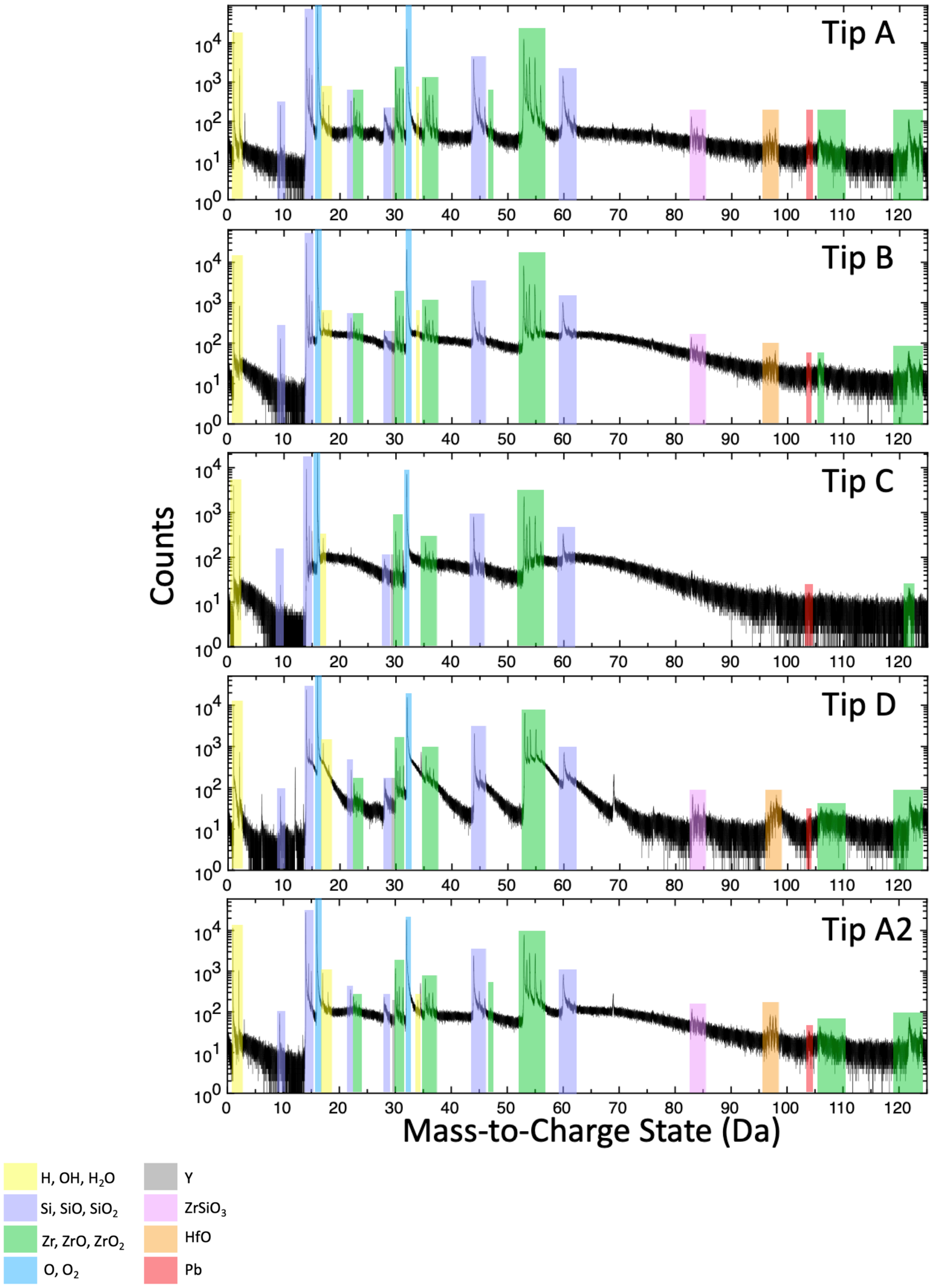

Figure 5-3. Mass-to-Charge State ratio spectra for the 5 tips analyzed. Important ions have been labeled with a corresponding color. This can include singly, doubly, and triply charged species, as well as complex ions.

datasets had prominent 104 Da peaks ($^{208}Pb^{++}$) above background. We did not see any peaks of radiogenic Pb (ex. $^{206}Pb^{++}$ at 103 Da) because the concentration of uranogenic Pb is below

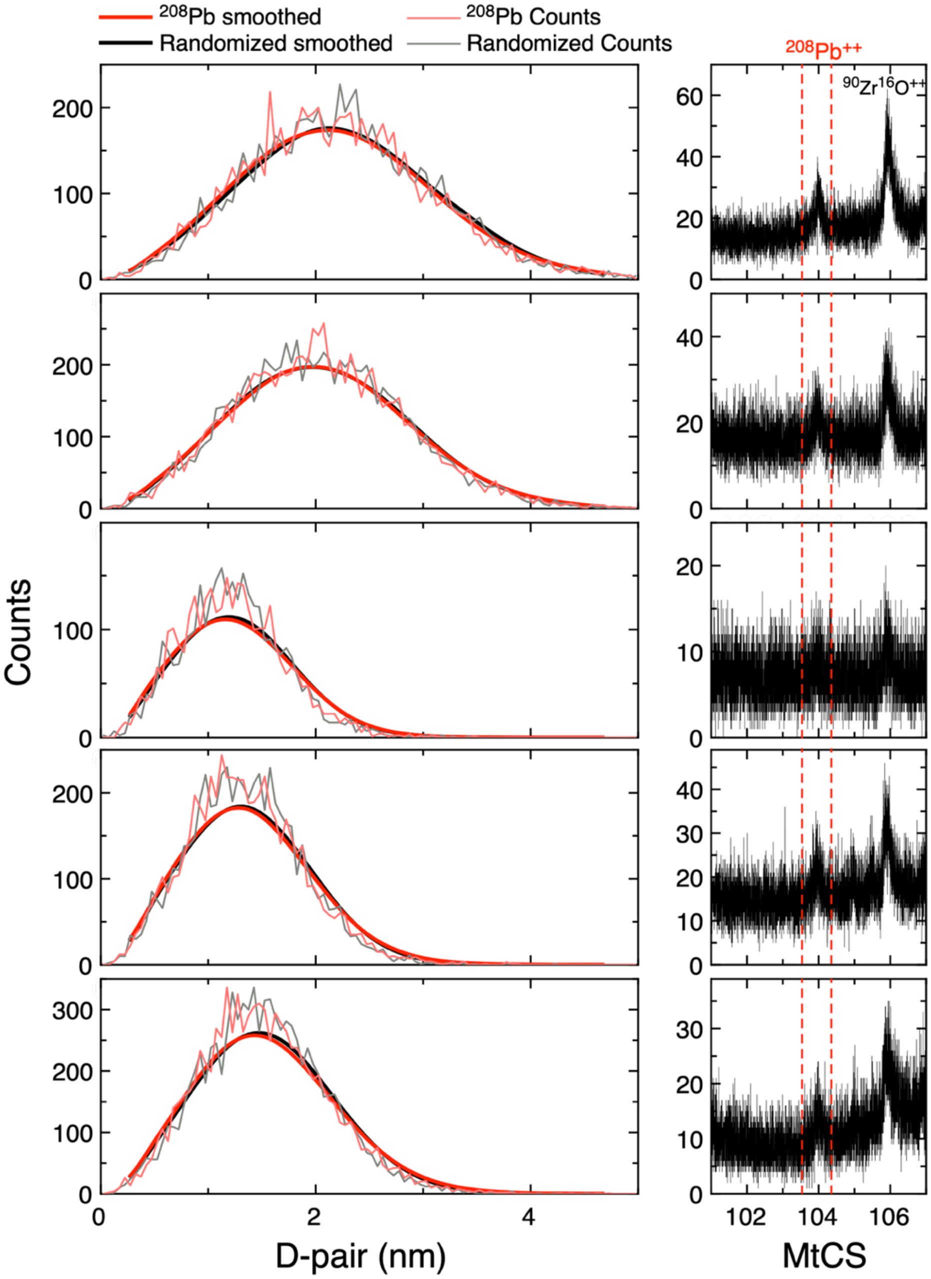

Figure 5-4: Nearest neighbor distribution of all analyzed tomographic datasets. To the left are the distributions of Pb atoms in the sample (plotted in light red) and randomized distribution (plotted in gray) shown along smoothed curves to remove noise. The pairs of curves are overlapping, and any slight deviation is within the noise of the signal from the low counts. On the right are plots of mass spectra of each of the 5 datasets for the Mass-to-Charge State (MtCS) range around $^{208}Pb^{2+}$. The dotted red line defines the range of the Pb peak that was included in the nearest neighbor calculation.

background. However, secondary Pb mobility would have affected all Pb atoms, regardless of their isotopic masses. Therefore, we can use the Pb isotope with the highest concentration as a proxy for all secondary Pb mobility in the sample. There is an isobaric overlap at this position: $^{28}Si_2{}^{16}O_3{}^+$. However, the other peaks associated with this molecular ion ($^{28}Si_2{}^{16}O_3$ at 106 Da and $^{28}Si_2{}^{16}O_3$ at 108 Da) do not follow the natural abundance pattern. Instead, the isotopic pattern at 106-110 Da matches that of the distribution of $Zr^{16}O^{++}$ molecular species that do not overlap with the 104 Da peak. Therefore, we conclude that the 104 Da peak is $^{208}Pb^{++}$. Even in samples where the peak at 104 would represent the combined concentration of $^{208}Pb^{++}$ and $^{28}Si_2{}^{16}O_3{}^+$, any Pb clustering, if present, would still be observable in the dataset from the combined peak if the Pb signal that

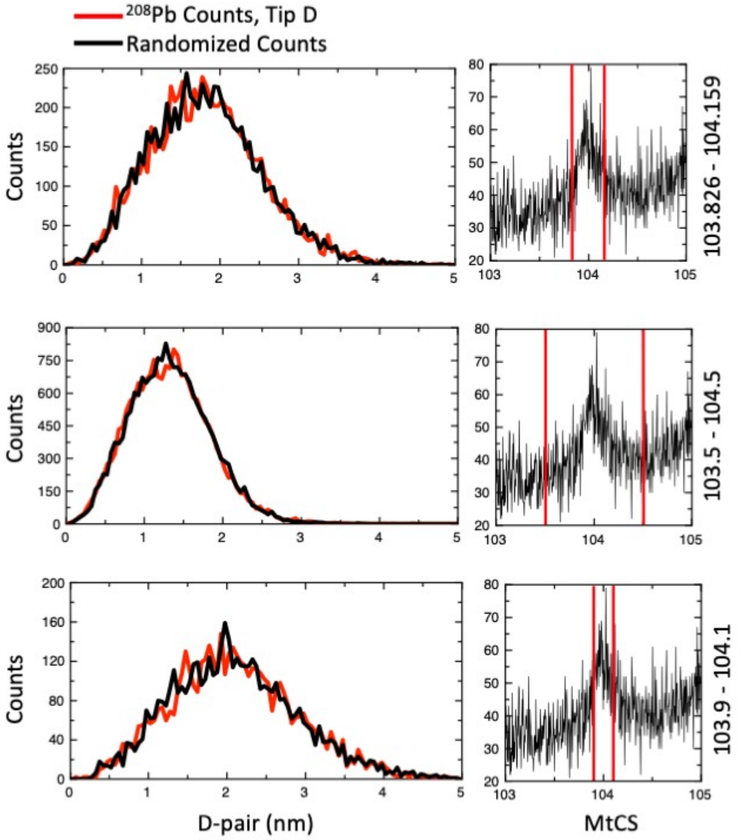

Figure 5-5: Nearest neighbor plots with different ranges, showing there is no clustering no matter how Pb is ranged. The distribution of Pb atoms in the sample (red) and random distribution (black) is plotted to the left. On the right are the Mass-to-Charge State (MtCS) spectra showing the range (bracketed by red lines) that was plotted in the left.

contributes to the 104 Da peak is above background. In addition to this, we determined our method is robust and not sensitive to the peak brackets or windows, also referred to as the *range* in APT publications, for which Pb abundances are determined and does not affect the result of the nearest neighbor distribution and clustering (Figure 5-5). Valley et al. 2015 reported clustering in both the Pb and Y distribution; with stronger Y clusters. The most prominent Y peak occurs at 29.67 Da, corresponding to Y^{+++}. While only Tip A has a Y peak above background (Figure 5-6), there are no major overlaps at this position, so this can be used unambiguously. Y clusters are present in a higher concentration than the Pb clusters and thus can be used as a proxy in our case with a low

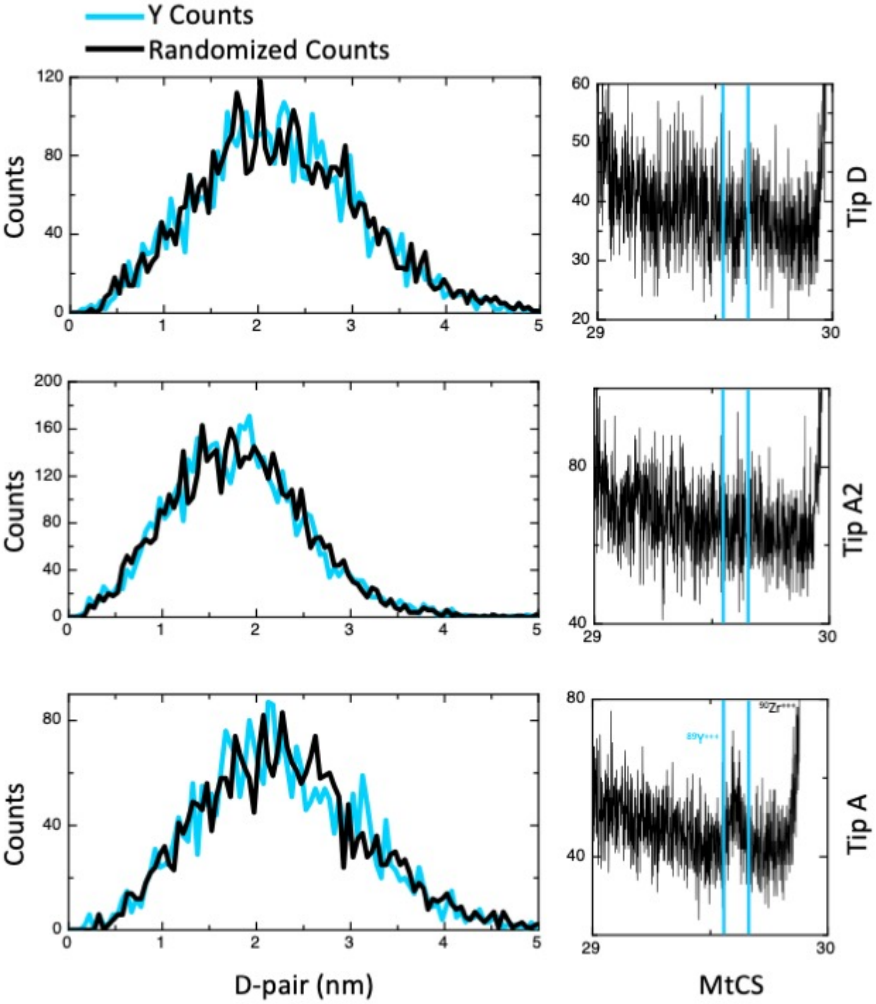

Figure 5-6: Nearest neighbor plots of Y, showing that there is no clustering in Y.

Pb concentration. Thus even if $^{28}Si_2{}^{16}O_3{}^+$ would dominate the signal at 104 Da, the absence of Y clusters implies that there is no Pb clustering. While resistive materials like zircon can have many different species of complex molecular ions in their mass spectra (e.g., Valley et al., 2015), conditions for these analyses were chosen to minimize the presence of molecular ions; most importantly by using a lower laser pulse energy.

5.5 DISCUSSION

We do not see any clustering in Pb or Y in any of the datasets which demonstrates that the zircon is homogenous on the nanoscale for all detected native species. While the absence of clustering in one dataset may indicate that the intercluster distance is larger than the sampled volume, the fact that none of the sampled volumes show clusters (Figure 5-4), even when separated by 1-2 µm, demonstrates that there is no nanoscale clustering in the analyzed domain of this zircon. There is heterogeneity in Pb distribution at the microscale, as shown by Zhang et al., 2021, however, this cannot be due to mixing of Pb nanoclusters. NanoSIMS analyses that report younger ages sampled domains of Pb-loss which happened post-crystallization, while the oldest ages sampled domains where the radiogenic Pb was retained. The other explanation for these ancient ages, the presence of clusters of excess Pb, does not apply to these samples as our analyses ruled this out. We therefore conclude that the age of this zircon as reported by NanoSIMS is the age of crystallization, and the minimum age of this old zircon population is 4460±30 Myr ago (2σ), which gives a minimum age of the formation of the Moon.

Thermal modelling by Elkins-Tanton et al., 2011 suggests that lunar differentiation took place rapidly, with 80 vol.% of the LMO solidified within thousands of years, which is significantly different from the thermal models produced by Maurice et al., 2020, which models a

KREEP formation age of to 200 Myr. In addition, the identical abundance of ^{182}W (produced by the decay of ^{182}Hf, $t_{1/2}$=8.9 My) among lunar rock suites suggests that internal differentiation occurred at least 70 My after the Solar System. With this timeframe, if the ^{176}Hf/^{177}Hf model age of the crystallization of the KREEP is 4478±46 Myr ago (Taylor et al., 2009), the age of the zircon analyzed by Nemchin et al., 2009 (4417±6 Myr ago) likely points to the formation of the evolved, late-forming alkali suite (McLeod et al., 2016). These ages, with the age of the Civet Cat zircons presented in Zhang et al., 2021, are a strong indication that the LMO had largely been solidified as early as ~4.46 Ga, and that the Giant Impact must have occurred before that within the first 100 million years of the formation of the solar system.

Subsequent bombardment events reworked or melted the earliest crust, modifying parts of the zircons, while pristine domains were preserved. The significance of this age depends on the preservation of domains which may have been modified by post-crystallization processes. The nanoscale analysis of these zircon grains demonstrates such preservation in these samples.

5.6 CONCLUSIONS

In this study, the NanoSIMS dating by Zhang et al., 2021 has been confirmed by APT. We have not observed any clustering, in either Pb or Y, in any of the nanotips which were lifted out from a volume that spans ~7 µm across the zircon and comprise a total analyzed volume ~1 µm if added up in length. Thus, there is no Pb and Y clustering in a volume larger than the NanoSIMS spot size, and therefore we conclude that the concordant U-Pb age of 4461±33 Myr ago from the Civet Cat norite (Zhang et al., 2021) is the oldest age for lunar zircons to date. If we observed Pb and/or Y clusters whose intercluster distance is more comparable to the NanoSIMS spot size, or concentration gradients within the nanotips, we would have clear evidence for Pb mobility which would imply the age is not valid. Not only have these zircons been characterized at the nanoscale, they are also the first ancient lunar zircon grains that still preserved in their lithologic context. This finding pushes the timing of the solidification of the lunar crust to within at least the first 100 Myr of the formation of the Solar System. Together with ^{182}Hf-^{182}W isotopic evidence that the internal differentiation of the Moon occurred at least 70 My after the formation of the Solar System, we can now place an age bracket on the timing of the Giant Impact and subsequent LMO crystallization to the between 4.50 and 4.46 Gyr ago. This serves an anchoring age interval for the onset of the intense gravitational effects that the early, much closer Moon had on the young Earth, as well as when the Moon began recording a history of bombardments, providing a chronometer for the inner Solar System.

5.7 REFERENCES

Aléon-Toppani, A., R. Brunetto, J. Aléon, Z. Dionnet, S. Rubino, D. Levy, D. Troadec, F. Borondics, and F. Brisset. "A preparation sequence for multi-analysis of micrometer-sized extraterrestrial samples." *Meteoritics & Planetary Science* 56 (2020): 1151-1172.

Arcuri, G. A., D. E. Moser, D. A. Reinhard, B. Langelier, and D. J. Larson. "Impact-triggered nanoscale Pb clustering and Pb loss domains in Archean zircon." *Contributions to Mineralogy and Petrology* 175, no. 7 (2020): 1-13.

Barboni, M., P. Boehnke, B. Keller, I. E. Kohl, B. Schoene, E. D. Young, and K. McKeegan. "Early formation of the Moon 4.51 billion years ago." *Science Advances* 3, no. 1 (2017): e1602365.

Blum, T. B., D. A. Reinhard, Y. Chen, T. J. Prosa, D. J. Larson, and J. W. Valley. "Uncertainty and sensitivity analysis for spatial and spectral processing of Pb isotopes in zircon by atom probe tomography." *Microstructural Geochronology: Planetary Records Down to Atom Scale* (2018): 327-350.

Borg, L. E., A. M. Gaffney, and C. K. Shearer. "A review of lunar chronology revealing a preponderance of 4.34–4.37 Ga ages." *Meteoritics & Planetary Science* 50, no. 4 (2015): 715-732.

Bottke, W. F., D. Vokrouhlický, S. Marchi, T. Swindle, E. R. D. Scott, J. R. Weirich, and H. Levison. "Dating the Moon-forming impact event with asteroidal meteorites." *Science* 348, no. 6232 (2015): 321-323.

Cameron, A. G. W., and W. R. Ward. "The origin of the Moon." In *Lunar and Planetary Science Conference*, vol. 7. 1976.

Canup, R. M. "Dynamics of lunar formation." *Annual review of astronomy and astrophysics* 42, no. 1 (2004): 441-475.

Connelly, J. N., and M. Bizzarro. "Lead isotope evidence for a young formation age of the Earth–Moon system." *Earth and Planetary Science Letters* 452 (2016): 36-43.

Elkins-Tanton, L. T., S. Burgess, and Q.-Z. Yin. "The lunar magma ocean: Reconciling the solidification process with lunar petrology and geochronology." *Earth and Planetary Science Letters* 304, no. 3-4 (2011): 326-336.

Ge, R., S. A. Wilde, A. A. Nemchin, M. J. Whitehouse, J. J. Bellucci, and T. M. Erickson. "Mechanisms and consequences of intra-crystalline enrichment of ancient radiogenic Pb in detrital Hadean zircons from the Jack Hills, Western Australia." *Earth and Planetary Science Letters* 517 (2019): 38-49.

James, O. B. "Mineralogy and petrology of the pristine rocks." In *Pristine Highlands Rocks and the Early History of the Moon*, p. 44. 1983.

Kelly, T. F. Miller, M. K. “Atom probe tomography.” In *Review of Scientific Instruments* 78 (2007).

Kusiak, M. A., M. J. Whitehouse, S. A. Wilde, D. J. Dunkley, M. Menneken, A. A. Nemchin, and C. Clark. "Changes in zircon chemistry during Archean UHT metamorphism in the Napier Complex, Antarctica." *American Journal of Science* 313, no. 9 (2013): 933-967.

Kusiak, M. A., M. J. Whitehouse, S. A. Wilde, A. A. Nemchin, and C. Clark. "Mobilization of radiogenic Pb in zircon revealed by ion imaging: Implications for early Earth geochronology." *Geology* 41, no. 3 (2013): 291-294.

Maurice, M., N. Tosi, S. Schwinger, D. Breuer, and T. Kleine. "A long-lived magma ocean on a young Moon." *Science Advances* 6, no. 28 (2020): eaba8949.

McLeod, C. L., A. D. Brandon, V. A. Fernandes, A. H. Peslier, J. Fritz, T. Lapen, J. T. Shafer, A. R. Butcher, and A. J. Irving. "Constraints on formation and evolution of the lunar crust from feldspathic granulitic breccias NWA 3163 and 4881." *Geochimica et Cosmochimica Acta* 187 (2016): 350-374.

Nemchin, A., N. Timms, R. Pidgeon, T. Geisler, S. Reddy, and C. Meyer. "Timing of crystallization of the lunar magma ocean constrained by the oldest zircon." *Nature geoscience* 2, no. 2 (2009): 133-136.

Taylor, D. J., K. D. McKeegan, and T. M. Harrison. "Lu–Hf zircon evidence for rapid lunar differentiation." *Earth and Planetary Science Letters* 279, no. 3-4 (2009): 157-164.

Thiemens, M. M., P. Sprung, R. O. C. Fonseca, F. P. Leitzke, and C. Münker. "Early Moon formation inferred from hafnium–tungsten systematics." *Nature Geoscience* 12, no. 9 (2019): 696-700.

Valley, J. W., Cavosie, A. J., Ushikubo, T., Reinhard, D. A., Lawrence, D. F., Larson, D. J., Clifton, P. H., Kelly, T. F., Wilde, S. A., Moser, D. E. and M. J. Spicuzza. "Hadean age for a post-magma-ocean zircon confirmed by atom-probe tomography." *Nature Geoscience* 7, no. 3 (2014): 219-223.

Valley, J. W., D. A. Reinhard, A. J. Cavosie, T. Ushikubo, D. F. Lawrence, D. J. Larson, T. F. Kelly, D. R. Snoeyenbos, and A. Strickland. "Nano-and micro-geochronology in Hadean and Archean zircons by atom-probe tomography and SIMS: New tools for old minerals." *American Mineralogist* 100, no. 7 (2015): 1355-1377.

Warren, P. H., and J. T. Wasson. "The origin of KREEP." *Reviews of Geophysics* 17, no. 1 (1979): 73-88.

Warren, P. H. "The magma ocean concept and lunar evolution." *Annual Review of Earth and Planetary Sciences* 13 (1985): 201-240.

Wood, J. A., J. S. Dickey Jr, U. B. Marvin, and B. N. Powell. "Lunar anorthosites and a geophysical model of the moon." *Geochimica et Cosmochimica Acta Supplement* 1 (1970): 965.

Zhang, B., Y. Lin, D. E. Moser, J. Hao, Y.-L., J. Zhang, I. R. Barker, Q. Li, S. R. Shieh, and A. Bouvier. "Radiogenic Pb mobilization induced by shock metamorphism of zircons in the Apollo 72255 Civet Cat norite clast." *Geochimica et Cosmochimica Acta* 302 (2021): 175-192.